FEDERAL UNIVERSITY OF ESPÍRITO SANTO
TECHNOLOGICAL CENTER
POSTGRADUATE PROGRAM IN ELECTRICAL ENGINEERING

WESLEY DA SILVA COSTA

DOCTORAL THESIS

TOWARDS ARTIFICIAL INTELLIGENCE IN VISIBLE LIGHT COMMUNICATION SYSTEMS

VITÓRIA
APRIL 2023

FEDERAL UNIVERSITY OF ESPÍRITO SANTO
TECHNOLOGICAL CENTER
POSTGRADUATE PROGRAM IN ELECTRICAL ENGINEERING

Author:
WESLEY DA SILVA COSTA

Advisors:
PROF. DR. JAIR A. LIMA SILVA
PROF. DR. HELDER R. O. ROCHA
DR. ANAGNOSTIS PARASKEVOPOULOS

TOWARDS ARTIFICIAL INTELLIGENCE IN VISIBLE LIGHT COMMUNICATION SYSTEMS

Doctoral Thesis submitted to the Graduate Program in Electrical Engineering from the Technological Center of the Federal University of Espírito Santo, as a requirement for the degree of Doctor in Electrical Engineering.

VITÓRIA
APRIL 2023

Ficha catalográfica disponibilizada pelo Sistema Integrado de Bibliotecas - SIBI/UFES e elaborada pelo autor

---

Costa, Wesley da Silva, 1992-
C837t Towards Artificial Intelligence in Visible Light Communication Systems / Wesley da Silva Costa. - 2023.
162 f. : il.

Orientador: Jair Adriano Lima Silva.
Coorientadores: Helder Roberto de Oliveira Rocha, Anagnostis Paraskevopoulos.
Tese (Doutorado em Engenharia Elétrica) - Universidade Federal do Espírito Santo, Centro Tecnológico.

1. Visible Light Communication. 2. Artificial Intelligence. 3. Soft Computing. 4. Optimization. 5. Spectral Efficiency. 6. Power Efficiency. I. Silva, Jair Adriano Lima. II. Rocha, Helder Roberto de Oliveira. III. Paraskevopoulos, Anagnostis. IV. Universidade Federal do Espírito Santo. Centro Tecnológico. V. Título.

CDU: 621.3

Approval Sheet

April 20, 2023.

This doctoral thesis entitled "*Towards Artificial Intelligence in Visible Light Communication Systems*", prepared and submitted by Wesley da Silva Costa in partial fulfillment of the requirements for the degree of Doctor in Electrical Engineering at the Federal University of Espírito Santo (UFES), has been examined and is recommended for acceptance and approval for Oral Defense.

Documento assinado digitalmente
gov.br JAIR ADRIANO LIMA SILVA
Data: 15/06/2023 17:48:50-0300
Verifique em https://validar.iti.gov.br

Prof. Dr. Jair Adriano Lima Silva (Advisor)
Federal University of Espírito Santo - UFES

Documento assinado digitalmente
gov.br HELDER ROBERTO DE OLIVEIRA ROCHA
Data: 12/06/2023 16:28:49-0300
Verifique em https://validar.iti.gov.br

Prof. Dr. Helder Roberto de Oliveira Rocha (Co-advisor)
Federal University of Espírito Santo - UFES

Dr. -Ing. Anagnostis Paraskevopoulos (Co-advisor)
Fraunhofer-Institut für Nachrichtentechnik, Heinrich-Hertz-Institut - HHI

Approved by the following Committee on Oral Examination.

Documento assinado digitalmente
gov.br ALEXANDRE DE ALMEIDA PRADO POHL
Data: 19/06/2023 17:05:34-0300
Verifique em https://validar.iti.gov.br

Prof. Dr. Alexandre de Almeida Prado Pohl (External Researcher)
Federal University of Technology – Paraná - UTFPR

Documento assinado digitalmente
gov.br REGINALDO BARBOSA NUNES
Data: 27/06/2023 14:47:08-0300
Verifique em https://validar.iti.gov.br

Prof. Dr. Reginaldo Barbosa Nunes (External Researcher)
Federal Institute of Espírito Santo - IFES

Prof. Dr. Maria José Pontes (Internal Researcher)
Federal University of Espírito Santo - UFES

Prof. Dr. Marcelo Eduardo Vieira Segatto (Internal Researcher)
Federal University of Espírito Santo - UFES

Prof. Dr. Patrick Marques Ciarelli (Internal Researcher)
Federal University of Espírito Santo - UFES

UNIVERSIDADE FEDERAL DO ESPÍRITO SANTO

PROTOCOLO DE ASSINATURA

O documento acima foi assinado digitalmente com senha eletrônica através do Protocolo Web, conforme Portaria UFES nº 1.269 de 30/08/2018, por
MARCELO EDUARDO VIEIRA SEGATTO - SIAPE 1172919
Departamento de Engenharia Elétrica - DEE/CT
Em 03/07/2023 às 12:11

Para verificar as assinaturas e visualizar o documento original acesse o link:
https://api.lepisma.ufes.br/arquivos-assinados/740751?tipoArquivo=O

Abstract

In recent years, the increasing applications of Internet of Things (IoT) and smart devices have accelerated the demand for signal bandwidth. However, radiofrequency (RF) wireless systems cannot meet this upcoming need because of spectrum congestion in urban areas and insufficient bandwidth, mainly in indoor environments. These facts pave the way for alternatives to reduce the pressure of the RF spectrum in such conditions and also ensure high data rates, low latency, reliability, and low cost. The advance of Light-Emitting Diode (LED) technology provided high energy efficiency lighting with a high-speed light intensity switching. These facts, along with the possible spectrum crunch, have given rise to research interests in Visible Light Communication (VLC), through which data are transmitted using the existing lighting infrastructure. VLC offers a complementary alternative to radio-based systems, with an unlicensed optical spectrum (approximately 400 THz), security at the physical layer, low power, high speed, and immunity to RF electromagnetic interference.

A high data rate can be achieved by combining the broadband VLC channel and multicarrier modulation schemes. Orthogonal Frequency Division Multiplexing (OFDM) is largely studied because of its spectral efficiency promotion and capacity to deal with multipath fading. However, the nonlinearity introduced by the LED offers a challenge to the OFDM parameters settings, due to its high Peak-to-Average Power Ratio (PAPR). This work tackles the challenge of conveying OFDM signal considering the Intermodulation Distortion (IMD) produced by the LED nonlinearity.

This Thesis addresses the nonlinear LED effects, VLC parameters, and its performance for conventional and constant-envelope OFDM. The VLC system is modeled and optimization algorithms are evaluated to achieve parameters that provide maximum power and spectral efficiencies, constrained by modulation figure of metrics: bit error rate and error vector magnitude. This work also presents the application of artificial neural networks in the physical layer of VLC systems. The Long Short-Term Memory (LSTM) neural network is applied to predict future positions, as well as channel gain, and also forecast optimized parameters. Additionally, an investigation of the OFDM equalization using deep learning architectures for a multipath single-input single-output VLC channel is proposed. Convolutional Neural Network (CNN) architectures are applied in a direct OFDM mapped symbols equalization, without channel estimation, interpolation, nor element-wised division, denominated Convolutional Neural Network Direct-Equalizer (CNN-DE).

Results show that the optimization based on meta-heuristics was capable to determine the

VLC parameters in order to satisfy the communication constraints. Additionally, they emphasize the trade-off between power and spectral efficiency in VLC: higher spectral efficiency is achieved with the increase of offset current (power) to deal with the IMD; in contrast, to achieve higher power efficiency, a lower spectral efficiency is obtained. The optimization results using constant-envelope outperforms the conventional OFDM with the proper choice of the phase modulation index. The LSTM showed as a powerful tool for routing forecasting and assessing the optimized parameters. The CNN-DE equalizer (regression) was capable of detecting the correct symbol for lower SNR (≤ 10 dB). Additionally, the classification version of the CNN-DE was able to predict and classify the mapped symbols similarly to the least-square-based equalization.

***Keywords*:** Artificial intelligence, OFDM Equalization, Meta-heuristics, Power efficiency, Spectral efficiency, and Visible light communication.

Resumo

Nos últimos anos, o uso crescente de dispositivos inteligentes e aplicações em Internet das Coisas (IoT) acelerou a demanda por largura de banda. No entanto, os sistemas sem fio de radiofrequência (RF) não podem atender a essas necessidades futuras devido ao congestionamento do espectro em áreas urbanas e largura de banda insuficiente, principalmente em ambientes internos. Esses fatos abrem caminho para alternativas para reduzir a pressão do espectro de RF, em tais condições, e também garantir altas taxas de dados, baixa latência, confiabilidade e baixo custo. O avanço da tecnologia em diodos emissores de luz (LED, do inglês *Light Emitting Diode*) proporcionou iluminação de alta eficiência energética com comutação de intensidade de luz de alta velocidade. Estes fatos, juntamente com a possível crise de espectro, deram origem a interesses de pesquisa em Comunicação via Luz Visível, em que os dados são transmitidos usando a infraestrutura de iluminação existente. O VLC oferece uma alternativa complementar à RF, com espectro óptico não licenciado (aproximadamente 400 THz), segurança na camada física, baixa potência, alta velocidade e imunidade à interferência eletromagnética.

Alta taxa de dados pode ser alcançada com a combinação do canal VLC de banda larga e esquemas de modulação multiportadoras. A modulação ortogonal por divisão de frequência (OFDM) é amplamente estudada devido à sua promoção de eficiência espectral e capacidade de lidar com multipercursos. No entanto, a não linearidade introduzida pela fonte de luz luminosa representa um desafio para a parametrização do OFDM, devido à sua alta relação de potência pico-média (PAPR). Este trabalho aborda o desafio de transmitir o sinal OFDM considerando a distorção de intermodulação (IMD) produzida pelos efeitos não lineares do LED.

Esta Tese aborda os efeitos não lineares do LED, parâmetros VLC e seu desempenho para OFDM convencional e de envoltória constante (CE-OFDM). O sistema VLC é modelado e algoritmos de otimização são usados para atingir parâmetros que garantem eficiências de potência e espectral, limitadas pelas figuras de merito de comunicação: taxa de erro de bit e magnitude do vetor de erro. Este trabalho também apresenta a aplicação de redes neurais artificiais na camada física de sistemas VLC. A rede neural de memória longa de curto prazo (LSTM) é aplicada para prever posições, bem como ganho de canal, e também prever parâmetros otimizados. Além disso, é proposta uma investigação sobre a equalização OFDM usando arquiteturas de aprendizado profundo para um canal VLC multicaminhos de única entrada e única saída (SISO). As arquiteturas de redes neurais convolucionais (CNN) são aplicadas em equalização direta de símbolos mapeados OFDM, sem estimativa de canal, interpolação, nem divisão elementar, denominada CNN-Direct Equalization (CNN-DE).

Resultados mostram que a otimização baseada em meta-heurísticas foi capaz de determinar os parâmetros do VLC para atender às restrições de comunicação. Além disso, enfatizam o compromisso entre a potência e a eficiência espectral no VLC: maior eficiência espectral é alcançada com o aumento da corrente de polarização, i.e., aumento da potência, para lidar com o IMD, em contraste, para obter maior eficiência de potência, uma menor eficiência espectral é obtida. Os resultados das otimizações usando CE-OFDM superam o OFDM convencional, com a escolha adequada do índice de modulação de fase. O LSTM mostrou-se poderoso para a previsão de roteamento e avaliação dos parâmetros otimizados. O CNN-DE (regressão) foi capaz de detectar os símbolos corretos para valores baixos de SNR ($\leq$ 10 dB). No entanto, a equalização CNN-DE baseada na classificação foi capaz de detectar os símbolos mapeados de forma semelhante à equalização baseada em mínimos quadrados.

***Palavras-Chave*:** Comunicação via luz visível, Eficiência de Potência, Eficiência espectral, Equalização OFDM, Inteligência Artificial e Metaheuristicas.

Acknowledgments

This Thesis becomes a reality with the assistance and kind support of many individuals. I want to extend my most sincere thanks to each and every one of them.

Foremost, I would like to express my special gratitude and thanks to my advisors Dr. Jair Adriano Lima Silva and Dr. Helder Roberto de Oliveira Rocha for imparting their knowledge and expertise in this study, it was an ongoing honor to learn from them. Also acknowledged is Dr. Jorge Aching for the valuable machine learning advice and the unquestionable didactic.

I am deeply grateful to the Fraunhofer Heinrich Hertz Institute (HHI), particularly Malte Hinrichs and Dr. Anagnostis Paraskevopoulos, for their assistance, direction, and ongoing monitoring of my results as well as for supplying crucial details regarding a portion of this research.

My thanks and appreciations also go to the colleague and people of the Telecommunication Laboratory (LabTel) and HHI, who have willingly helped me out with their abilities.

This work would not have been possible without the financial support provided by Capes – Brazilian Federal Agency for Support and Evaluation of Graduate Education within the Ministry of Education of Brazil (Grant CAPES PIPC 12/2018) and FAPES - Foundation for Support to Research and Innovation of Espírito Santo (Grant FAPES 026/2018 and FAPES/CAPES nº 01/2018).

Finally, I want to offer this endeavor to my family and friends, for their support and care. I would like to express my gratitude for the encouragement, for believing and investing the maximum that they could. You brought me here!

Contents

List of Figures

List of Tables

List of Algorithms

List of Abbreviations and Acronyms

5G	Fifth generation of wireless cellular technology
ACO-OFDM	Asymmetrically Clipped Optical OFDM
ADC	Analog-to-Digital Converter
AI	Artificial Intelligence
ANN	Artificial Neural Network
AWGN	Additive White Gaussian Noise
BER	Bit Error Rate
BPSK	Binary Phase Shift Keying
CAP	Carrierless Amplitude Phase Modulation
CD	Crowding Distance Criteria
CE	Channel Estimation
CE-OFDM	Constant-Envelope OFDM
CNN	Convolutional Neural Network
CNN-DE	Convolutional Neural Network Direct-Equalizer
CP	Cyclic Prefix
DC	Direct Current
DCO-OFDM	Direct Current Optical OFDM
DFT	Discrete Fourier Transform
DNN	Deep Neural Network
DVB	Digital Video Broadcasting
EVM	Error Vector Magnitude
FDM	Frequency Division Multiplexing
FFT	Fast Fourier Transform
Flip-OFDM	Flipped OFDM
FOV	Field of View
GA	Genetic Algorithm
GWO	Grey Wolf Optimization
HMO	Hybrid Multi-Objective Optimization
HS	Hermitian Symmetry
IDFT	Inverse Discrete Fourier Transform
IFFT	Inverse Fast Fourier Transform

IM/DD	Intensity Modulation and Direct Detection
IMD	Intermodulation Distortion
IoT	Internet of Things
IR	Infrared
ISI	Intersymbol Interference
LACO-OFDM	Layered ACO-OFDM
LED	Light-Emitting Diode
LOS	Line-of-Sight Propagation
LS	Least-Square
LSTM	Long Short-Term Memory
LTE	Long-Term Evolution
MCM	Multicarrier Modulation
MIMO	Multiple-Input Multiple-Output
MISO	Multiple-Input Single-Output
ML	Machine Learning
MMSE	Minimum Mean Square Error
MOGWO	Multi-objective Grey Wolf Optimization
MOO	Multi-Objective Optimization
MOPSO	Multi-objective Particle Swarm Optimization
NLOS	Non-Line-of-Sight Propagation
NSGA-II	Non-Sorting Genetic Algorithm II
NSGA-III	Non-Sorting Genetic Algorithm III
OFDM	Orthogonal Frequency Division Multiplexing
OMI	Optical Modulation Index
OOK	On-Off Keying
OWC	Optical Wireless Communications
PAM	Phase Amplitude Modulation
PAM-DMT	Pulse Amplitude Modulated Discrete Multitone
PAPR	Peak-to-Average Power Ratio
PD	Photodetector
PHY	Physical Layer
PLC	Power-line Communication
PM	Phase Modulation
PPM	Pulse-Position Modulation
PRBS	Pseudorandom Binary Sequence
QAM	Quadrature Amplitude Modulation
RF	radiofrequency

RNN	Recurrent Neural Networks
SCM	Single-carrier Modulation
SE	Spectral Efficiency
SISO	Single-Input Single-Output
SNR	Signal-to-Noise Ratio
TIA	Transimpedance Amplifier
UV	Ultraviolet
VLC	Visible Light Communication

List of Symbols and Notations

Signal

$2\pi h$	Phase modulation index
Δ_{f}	OFDM subcarrier spacing
$C_(N)$	OFDM normalization factor
D_{in}	Input binary data stream
D_{out}	Output binary data stream
f_k	Carrier frequency of the k-th subcarrier
h	Channel impulse response
l	Number of the OFDM symbol
N	Number of subcarriers
N_{symb}	Number of symbols to evaluate the EVM metric
P_0	Power of the transmitted constellation
R_{b}	Bit rate
T_{G}	Guard interval duration
T_{sym}	OFDM symbol duration
W	Channel noise (frequency domain)
X	Transmitted OFDM signal (frequency domain)
x	Transmitted OFDM signal (time domain)
Y	Received OFDM signal (frequency domain)
y	Received OFDM signal (time domain)

Meta-Heuristics

$\overrightarrow{s}$	Feasible solution vector
f	Outcome of an objective function
k_l	Size of spliting non-dominated front
P_T	Parent set
Q_T	Offspring set
S_T	Combined set of solutions

Machine Learning

$\sigma(\cdot)$	Sigmoid/logistic activation function
$\tanh(\cdot)$	Hyperbolic tangent activation function
b	Bias
h_t	Recurrent information

W	Weights matrix

Operators and Miscellaneous Symbols

$(\cdot)$	Point-wise multiplication vectors
$(\cdot)^*$	Complex conjugate
$\approx$	Approximately equal
$\circledast$	Convolution operation
$\cos(\cdot)$	Cosine
$\leq$	Less than or equal to
$\ln(\cdot)$	Natural logarithm
$\log_b(\cdot)$	Logarithm of base *b*
$\mathbb{E}(\cdot)$	Expected value
$\mathcal{F}\{\cdot\}$	Fast Fourier transform
$\mathcal{U}$	Uniform distribution
$\max$	Maximum
π	3.14159265358979...
$\Re\{\cdot\}$	Real part
$e^(\cdot)$	Exponential
j	$\sqrt{-1}$
$Q[\cdot]$	Gaussian co-error function

Set Theory

$\cup$	Union of sets
$\exists$	Exists
$\forall$	For all
$\in$	Is an element

Visible Light Communications

α	Linear amplification factor
γ	Photodetector responsivity
κ	Boltzman constant
ϕ	Radiation angle
$\Phi_{1/2}$	Semi-angle of half power
Ψ	Incidence angle
Ψ_{c}	Field Of view
$\sigma_{\mathrm{bg-shot}}$	Background shot noise
σ_{dark}	Dark noise

$\sigma_{\mathrm{q-shot}}$	Quantum shot noise
σ_{therm}	Thermal noise
A_{d}	Area of photodetection
A_{eff}	Area of incident collecting radiation
B_{pd}	Photodector bandwidth
B_{W}	Bandwidth
d	VLC link length
D_{out}	Output binary data stream
g	Optical gain in a VLC link
G_{B}	Guard-Band
G_{I}	Guard-interval
H_{los}	Line-of-fight channel gain
$H_{\mathrm{n-los}}$	Non-line-of-sight channel gain
$H_{\mathrm{reflection}}$	Gain of each reflection link in VLC channel NLOS
I_{bias}	LED DC current
I_{LED}	LED current
I_{max}	Maximum LED-feeding current
I_{pc}	Photocurrent
I_{sig}	Amplified signal to be transmitted
m_{L}	Lambert's mode number
N_0	Noise power spectral density
N_{FFT}	FFT size
n_{i}	Concentrator internal refractive index
N_{samp}	Resampling factor
P_{bg}	Background received power
P_{DC}	DC LED optical power
P_{max}	Maximum LED optical power
$P_{\mathrm{r-los}}$	Received LOS optical power
$P_{\mathrm{r-nlos}}$	Received NLOS optical power
P_{sig}	Signal LED optical power
P_{t}	Transmitted LED optical power
q	Electronic charge
R	LED radiation intensity
R_0	Lambertian radiant intensity distribution
R_{L}	Photodector resistence

T_{e}	Photodector temperature
T_{s}	Optical band-pass filter transmission
w	Photodetection noise
W_0	Photodetection power noise
ζ	Electrical-optical adjustment constant

CHAPTER 1.
Introduction

1.1. Introduction and Motivation

Due to the increasing demand for high data rates in wireless communication, the available RF spectrum below 10 GHz has become insufficient [5]. In order to alleviate the RF spectrum crunch, a complementary system is indispensable. With the improvement of LED technology, VLC emerges as a viable technology to provide wireless connectivity, mainly in indoor scenarios [6], as it offers more capacity if compared with radio-based technology because of its higher bandwidth. VLC describes an Optical Wireless Communications (OWC) in which LED with wavelengths around $400 - 700$ nm are implemented [7], [8].

By 2030, 75% of the world's illumination will be generated from LEDs [9]. The availability of LED illumination in indoor and outdoor environments enables the applicability of VLC technology, providing concurrent illumination and communication. This technology is useful in industrial applications where additional spectrum is needed, and it can be integrated with 5G to offload a significant amount of ultra-reliable and low-latency traffic to the optical domain [10]. Communication security at short distances, low energy consumption, and an unlicensed spectrum are also benefits achieved with VLC [11].

In order to attain a high data rate and to provide high Spectral Efficiency (SE), Orthogonal Frequency Division Multiplexing (OFDM) is applied in the physical layer of communication systems [12]. The following are the main benefits of the OFDM modulation: lessen the severe effects of frequency-selective fading and offer a low complexity channel equalization [13]. In VLC, with the increase of the modulating OFDM signal's magnitude, the LED operation is driven to its nonlinear region, which distorts the output optical signal, and also limits the transmitted optical power. Therefore, the sensitivity to distortions introduced by current biasing close to the LED nonlinear region is attributed as a challenge to OFDM-based VLC systems [14, 15]. Resource allocation, via optimization techniques, gained attention in VLC, notably for downlink multi-user transmission [16], [17]. SE was particularly addressed in [16], considering resource allocation in a dynamic time division multiple access VLC system. Performance gains were achieved by optimizing time and power allocation. A survey on the optimization techniques reported in the literature to improve the performance of multi-users VLC systems is provided in [17].

The PAPR of the modulating signals is an important issue to be considered in LED-based

light source VLC. Different techniques were developed to reduce the PAPR and, accordingly, mitigate nonlinearity and increase the average transmitted power [18–20]. However, the PAPR reductions achieved in [18] and [19] are relatively small, and the complexity required by the transceiver suggested in [20] is higher if compared to the conventional OFDM scheme. The transmission of Constant-Envelope OFDM (CE-OFDM) based on electrical phase modulation was shown to improve the tolerance to noise and the nonlinearities in optical communications [21–23]. In VLC, this allows the application of larger signal amplitudes despite the LED nonlinearities and, thus, increasing power efficiency [24, 25]. The OFDM IMD decreases the performance of the system and enforces higher optical guard-bands (G_{B}), consequently reducing the SE, as described in [26]. These trade-offs suggest the application of optimization algorithms that consider the bandwidth (B_{W}) of the signal and carrier frequency, along with the size of the guard-interval (G_{I}), applied to exclude the inter-symbol interference [23, 27]. This is a particular issue in VLC systems based on CE-OFDM because of the spectral broadening that characterizes such low PAPR signals.

Artificial Intelligence (AI) related technologies, such as optimization theory and deep learning, can play significant roles in the Physical Layer (PHY) efficiency of wireless communication systems, in particular for smart manufacturing in Industry 4.0 [28]. A good balance between performance and operational cost, via real-time resource allocation, is a major issue. Optimization theory is indeed widely used to solve signal processing problems in the physical layer of optical communication systems [29], [30], [31]. An exhaustive search optimization procedure was used to increase the capacity of transport optical networks [29, 32]. A Genetic Algorithm (GA) was effectively employed in [30] to optimize the routing, modulation, and spectrum assignments in networks based on optical OFDM. Due to the major interest in GA, in [31] was suggested the application of the elitist Non-Sorting Genetic Algorithm II (NSGA-II) in short-range optical OFDM systems, aiming at SE. Including more constraints, the same procedure was also applied in the PHY parameters optimization conducted in [23], focusing on constant-envelope optical OFDM signals. Recently, in [33] was proposed a heuristic to allocate optical and radio access resources in the Fifth generation of wireless cellular technology (5G) telecommunication infrastructures. The optimization proposed by the authors provided a dynamic and energy-efficient resource allocation in a realistic scenario.

Nonetheless, there are practical problems in optics communication in which AI based on Machine Learning (ML) can play an important role. According to [34], computational complexity and/or channel nonlinearity are drawbacks that can be overcome with deep learning. An AI procedure based on an extreme learning machine was used in [35] to guarantee fast training and good accuracy for the multi-objective optimization design of multi-pump Raman amplifiers in fiber links. More recently, in [36], a CNN was applied to optimize complexity and to compensate for nonlinear signal distortions in a long-haul and high data rate optical link. Several publications provided insights into the potential of ML in VLC systems [37–39]. In [37], it was

investigated the applicability of equalization based on deep learning in a Single-Input Single-Output (SISO) VLC system, without the need for channel estimation as a regressor. Similar to the experimental setup exploited in [38], the equalization scheme was implemented using a CNN. Nevertheless, no optimization algorithms were implemented to optimize the VLC link parameters, once it is proposed by this current work. In [38], the authors combined genetic algorithm-based delayers with neural networks to combat the synchrony and inter-symbol interference issues in multiple-input single-output OWC systems. A CNN was also used in [39], but as a demodulator in a non-orthogonal multiple access VLC system to compensate for linear and nonlinear distortions. Likewise, the potential of ML algorithms can be exploited in VLC to enhance system performance, mitigate nonlinear effects, compensate jitter, identify modulation format, and estimate phase deviation, among others [40].

1.2. Research Questions, Hypotheses, and Objectives

1.2.1. Research Questions

This thesis seeks to answer the following research questions (RQs).

RQ.1 - How can spectral and power efficiency be improved in visible light communication?

RQ.2 - How can AI assist the forecast of the optimal settings based on the receiver's trajectory and positioning in VLC systems?

RQ.3 - How can the equalization stage of VLC systems based on OFDM perform better by utilizing neural networks?

1.2.2. Hypotheses

To respond to the above-itemized questions, the following hypotheses (Hs) were investigated.

H.1 - By setting optimal parameters, determined by multi-objective optimization, it is possible to increase the spectral and power efficiency and exploit the LED nonlinear operation region.

H.2 - Recurrent neural network models can be used to forecast and deploy the optimal parameters provided by the optimization algorithms by using more power-efficient modulation forms.

H.3 - In the equalization step of VLC-based OFDM systems, neural network strategies can be employed to minimize complexity while outperforming traditional algorithms.

1.2.3. Research Objectives

The objective of this thesis is to investigate the nonlinear LED effects to increase power and spectral efficiencies. The PAPR reduction is also a perspective, hence, conventional OFDM and constant-envelope OFDM are also investigated in order to enhance the system performance and to increase the VLC link distances. This work addresses these issues with the introduction of artificial intelligence techniques: meta-heuristics and neural networks. The achievement of the main objective demanded the following specific goals:

- analyze the nonlinear effects and their relation with the VLC and multicarrier modulation parameters;
- develop the SISO VLC models according to real setups;
- employ meta-heuristic optimization algorithms to determine parameters that provide power and spectral efficiencies in SISO VLC schemes;
- perform different modulation techniques in order to compare their performance to deal with LED nonlinearities: conventional OFDM and constant-envelope OFDM;
- employ recurrent neural networks such as long short-term memory neural networks (LSTM) to predict the receiver's positions, as well as channel gain, and also forecast optimized parameters;
- apply convolutional neural networks in the OFDM demodulation, in order to directly equalize the mapped symbols without channel estimation, interpolation, or element-wised division,

1.3. Contributions

The developments in this thesis are to improve the VLC communication systems from artificial intelligence algorithms. The main contributions include a methodology for determining optimum parameters in OFDM-VLC systems with metaheuristic algorithms that increase the reach of the communication link and its spectral efficiency. In addition, a hybrid multi-objective optimization (HMO) procedure is proposed to achieve higher diversity by combining the Non-Sorting Genetic Algorithm III and the multi-objective Grey Wolf optimizer. Recurrent neural networks are used to forecast VLC-based OFDM parameters dependent on the receiver position obtained via the HMO and process. This thesis also includes the application of convolution neural networks to reduce receiver complexity through the equalization stage since it doesn't need channel estimation, interpolation, or other equalization processes.

1.4. Publications

During this Doctoral period, three papers on the research questions were submitted to journals, and three papers were published in conference proceedings. The journal papers are listed below.

J.1 - **Costa, W. S.**, Samatelo, J. L., Rocha, H. R., Segatto, M. E., and Silva, J. A. CNN direct equalization in OFDM-VLC systems: evaluations in a numerical model based on experimental characterizations. *Photonic Network Communications*, v. 45, p. 1-11, 2023.

J.2 - **Costa, W.**, Camporez, H., Hinrichs, M., Rocha, H., Pontes, M., Segatto, M., Rocha H., Silva J., Hinrichs, M., Paraskevopoulos, A., Jungnickel, V., and Freund, R. Toward AI-enhanced VLC Systems for Industrial Applications. *Journal of Lightwave Technology. (Invited Paper).*, v. 41, p. 1064 - 1076, 2022.

J.3 - **Costa, W.**, Camporez, H., Pontes, M., Segatto, M., Rocha, Silva J., Hinrichs, M., Paraskevopoulos, A., Jungnickel, V., and Freund, R. "Increasing the Power and Spectral Efficiencies of OFDM-based VLC System through Multi-objective Optimization," *Journal of the Optical Society of America. A, Optics, Image Science, And Vision*, v. 40, p. 1268-1275, 2023.

The published conference papers are the following.

C.1 - **W. Costa**, J. Samatelo, and J. Silva. Avaliação Experimental do Impacto da Aquisição de Sinais em Sistemas OFDM Multibandas. In *VIII Conferência Nacional em Comunicações, Redes e Segurança da Informação*, 2018, Salvador.

C.2 - **Costa, W. S.**, Samatelo, J. L., Rocha, H. R., Segatto, M. E., Silva, J. A. (2019, November). Direct equalization with convolutional neural networks in OFDM-based VLC systems. In *2019 IEEE Latin-American Conference on Communications* (LATINCOM) (pp. 1-6). IEEE.

C.3 - **W. Costa**, H. Camporez, M. Pontes, M. Segatto, H. Rocha, J. Silva, M. Hinrichs, A. Paraskevopoulos, V. Jungnickel, and R. Freund. "Increasing the LED Bias Point of an OFDM-based VLC System through Multi-objective Optimization." In *2021 SBMO/IEEE MTT-S International Microwave and Optoelectronics Conference (IMOC)*, pp. 1-3. IEEE, 2021.

C.4 - **W. Costa**, H. Camporez, M. Segatto, H. Rocha, and J. Silva. "Towards AI-enhanced VLC Systems." In *Optical Fiber Communication Conference*, pp. W3I-7. Optica Publishing Group, 2022.

Other publications listed below were published concurrently during the doctoral program and are correlated with the area of research however they were not included as part of this thesis.

1 - Silva, J., Pizzaia, J., **Costa, W.**, Camporez, H., Pontes, M., Rocha, H., and Segatto, M.

"Performance evaluation of a simplified power-domain NOMA for visible light communications". *JOSA A*, 40(4), v. 40, p. C46-C52, 2023.

2 - Peterle, A., **Costa, W.**, Camporez, H., Segatto, M., Rocha, H., and Silva, J. A. "Comparing the Performance of OFDM and OCDM-based Visible Light Communications: Numerical and Experimental Analysis". *Journal of Microwaves, Optoelectronics, and Electromagnetic Applications*, v. 22, p. 196-207, 2023.

3 - Camporez, H., **Costa, W.**, Pontes, M., Segatto, M., Rocha, H., Silva, J., Hinrichs, M., Paraskevopoulos, A., Jungnickel, V., and Freund, R. "Increasing the reach of visible light communication links through constant-envelope OFDM signals". *Optics Communications*, v. 530, p. 129179, 2023.

4 - **W. Costa**, W. Santos, H. Rocha, M. Segatto, and J. Silva. "Power line communication-based smart-plug prototype for power consumption monitoring in smart homes." *IEEE Latin America Transactions 19*, , v. 19, p. 1849-1857, 2021.

5 - V. Zwaag, K. Minne, M. Marinho, **W. Costa**, F. Santos, T. Bastos-Filho, H. Rocha, M. Segatto, and J. Silva. "A Manchester-OOK Visible Light Communication System for Patient Monitoring in Intensive Care Units." *IEEE Access 9* (2021), v. 9, p. 104217-104226, 2021.

6 - F. Monteiro, **W. Costa**, J. Neves, D. Silva, H. Rocha, E. Salles, and J. Silva. "Experimental Evaluation of Pulse Shaping based 5G Multicarrier Modulation Formats in Visible Light Communication Systems." *Optics Communications 457*, v. 457, p. 124693-124700, 2019.

7 - F. Monteiro, I. Silva, **W. Costa**, H. Rocha, E. Sales, J. Silva. "Análise de Desempenho de Esquemas e-OFDM". In: *VIII Conferência Nacional em Comunicações, Redes e Segurança da Informação, 2018, Salvador*. 2018.

8 - W. Santos, **W. Costa**, M. Faber, J. Silva, H. Rocha, and M. Segatto. "Sensor Allocation in a Hybrid Star-Mesh IoT Network using Genetic Algorithm and K-Medoids." In *2019 IEEE Latin-American Conference on Communications* (LATINCOM), pp. 1-6. IEEE, 2019.

9 - H. Camporez, **W. Costa**, J. Silva, H. Rocha, and M. Segatto. "Performance Evaluation of a Soft Handover Framework Applied to VLC Systems." In *2021 SBMO/IEEE MTT-S International Microwave and Optoelectronics Conference* (IMOC), pp. 1-3. IEEE, 2021.

1.5. Thesis Outline

This thesis is divided into six chapters. Chapter 1 provides the motivation with essential aspects, the objectives of the research, and the monograph outline. Chapter 2 presents a brief theoretical background on subjects covered in this work: Visible Light Communications, OFDM modulation schemes, and artificial intelligence algorithms. Chapter 3 covers the application of optimization techniques with the aim of maximizing the power and spectral efficiencies in conventional and constant-enveloped OFDM modulation. Chapter 4 presents the hybrid multiobjective optimizations in VLC with a moving receiver and the forecasting of routes and optimum parameters using LSTM. Chapter 5 is dedicated to investigating convolutional neural networks for channel equalization in OFDM-based VLC systems. Finally, in Chapter 6, the conclusions are outlined, and the future directions are presented and discussed. A flowchart outlining the connections between the research questions and the chapters of this thesis is provided in Fig. 1.1.

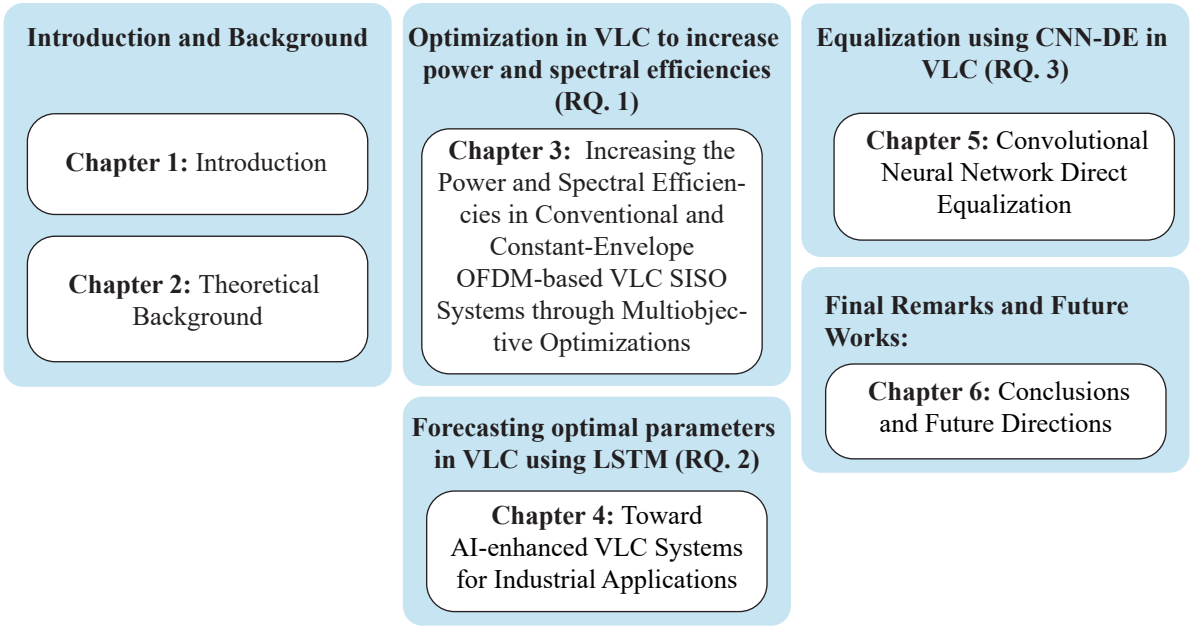

Figure 1.1. Diagram that depicts the relationship between the thesis's organization and its research questions.

CHAPTER 2.

Theoretical Background

This chapter presents the prior knowledge used as the basis for this work, such as the VLC system modeling, OFDM modulation in VLC, meta-heuristics optimization, and machine learning techniques with a focus on CNN and LSTM.

2.1. Visible Light Communications System

In OWC, the Ultraviolet (UV), visible, and Infrared (IR) bands provide high bandwidth for data communication. Fig. 2.1 depicts the electromagnetic spectrum with the classification according to the wave frequency or wavelength. The visible light spectrum provides a huge unlicensed bandwidth (approximately 400 THz) that represents 10,000 times the available RF bandwidth.

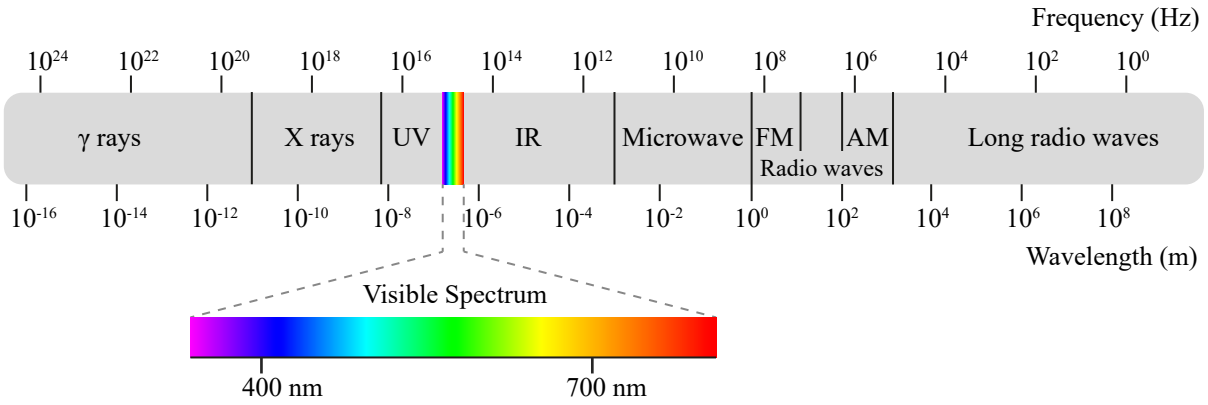

Figure 2.1. Wavelength and frequency of different portions of the electromagnetic spectrum. The wavelength range where the optical radiation is visible is comprised between 380 nm and 780 nm.

VLC usually adopts the Intensity Modulation and Direct Detection (IM/DD) scheme, where the analog signals are directly modulated onto the emitted visible light intensity [41]. In a VLC IM/DD system, the analog modulator converts a data bit stream into an analog waveform. The modulating signal is superimposed onto a driver circuit responsible to feed the light source. The light source (LED or laser diode) is able to convert the electrical signal into photons. At the receiver, the photodetector converts back the photons into an electrical signal that is amplified and filtered by a Transimpedance Amplifier (TIA) [42]. The data stream is detected after a demodulation stage. Fig. 2.2 illustrates the described VLC IM/DD system.

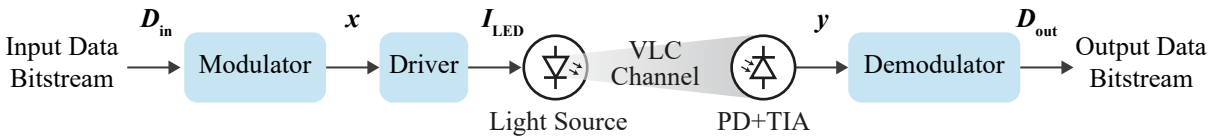

Figure 2.2. VLC intensity modulation and direct detection.

In order to design and operate an efficient VLC system is imperative that each stage is well understood. This section provides a brief historical background of VLC, addresses the LED nonlinear characteristics, discusses the VLC Line-of-Sight Propagation (LOS) channel modeling, and photodetection modeling and noise.

2.1.1. Brief Historical Background

The interest in the study of visible light in communications is due to its intrinsic ability to overcome electromagnetic interference. One of the first works on the subject dates from the 1880s, proposed by Alexander Graham Bell [43], in which a photophone is used for voice modulation using natural light over a distance of about 200 meters. After almost 100 years, experiments conducted with infrared radiation at 950 nm wavelength showed the potential of the OWC in indoor environments with a low-to-medium transmission rate at a range up to 50 meters [44]. Over the subsequent years, the advancement of optoelectronic devices, in special fast-switching LED technology, has paved the way for communications at higher data rates. A proof-of-concept was first proposed in [45], where a traffic light is used to convey information data at 950 nm and 1 Mbps while used for illumination.

Further studies sought to analyze the effects of multiple light source interference, light reflection [46], and shadowing [47] on the performance of the link. In [48], a wiring system for visible optical communication using the existing Power-line Communication (PLC) has been proposed. The white LED was used as the light source and the OFDM was used as the modulation. Extensions of the study were carried out in order to evaluate the brightness control methods [49] and high-accuracy positioning [50] to the communications system.

With the growing demand for high data rates, VLC emerges as a complementary technology for radio systems. Interests in VLC research focused on increasing spectral efficiency and, consequently, data transmission rate. In [51], the authors obtained through experiments a data rate of 50 Mbps with an On-Off Keying (OOK) Pulse-Position Modulation (PPM) as the format for wireless diffuse infrared communication. In [52], detecting only the blue component of the LED and using a simple first-order analog equalizer, a data rate of 100 Mb/s was achieved using OOK non-return-to-zero modulation. A VLC MIMO structure is able to add diversity at the transmission and reception and hence increases the data rate. In [53], a VLC Multiple-Input Multiple-Output (MIMO)-OFDM with a 2×1 array of LEDs and an imaging receiver composed of a 3×3 photodetector array reached 230 Mbps. In [54], a for 4×9 VLC MIMO is proposed

with 4 LED and 3×3 PD array could deliver a total transmission rate of 1.1 Gbps.

2.1.2. LED Light Source Characteristic Function

The magnitude of the modulating signal in a VLC system impacts the LED output optical power intensity, which varies according to the source's electrical-optical characteristics. In LED, the relationship between current and voltage is nonlinear because of the p-n junction and saturation effect [55]. The nonlinear LED characteristic can be expressed as in [56]

$$P_{\mathrm{LED}}(t) = \frac{I_{LED}(t)}{\left[\zeta + \left(\frac{I_{\mathrm{LED}}(t)}{P_{\max}}\right)^{2k}\right]^{1/(2k)}}, \tag{2.1}$$

where ζ is an adjustment constant, $P_{\max}$ is the maximum optical power emitted by the LED, and k is the knee factor that adjusts the level of intensity saturation illustrated. Fig. 2.3 illustrates a generic example of the LED nonlinearity for a Power-Current (P-I) curve. The LED current I_{LED} may be applied within the linear region (or dynamic region) to avoid the prone impairments in the performance due to saturation or clipping. For Direct Current (DC) optical systems, the LED current is mathematically expressed as $I_{\mathrm{LED}} = I_{\mathrm{bias}} + I_{\mathrm{sig}}$, where I_{bias} is the offset current, and I_{sig} represents the amplified signal to be conveyed. The LED output optical power is proportional to the current and expressed by $P_{\mathrm{LED}} = P_{\mathrm{DC}} + P_{\mathrm{sig}}$, where P_{DC} and P_{sig} are the optical power related to the bias and the signal current, respectively.

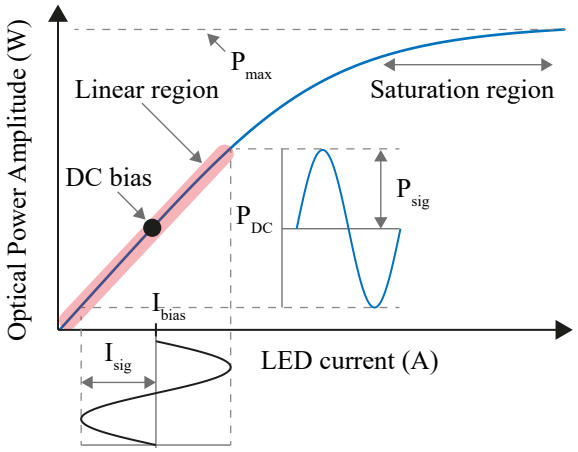

Figure 2.3. Generic LED P-I curve. The shown nonlinear transfer function characteristic emphasizes the linear region and the saturation region. The signal is naturally clipped for negative current values, which signalizes another nonlinear LED aspect.

2.1.3. VLC Channel Propagation Modeling

An LED light source is generally modeled as a Lambertian radiant intensity distribution R_0 calculated as in [6]

$$R_0(\phi) = \begin{cases} \frac{(m_\mathrm{L}+1)}{2\pi}\cos^{m_l}(\phi) & \text{for } \phi \in [-\pi/2, \pi/2] \\ 0 & \text{for } \phi \geq \pi/2, \end{cases} \tag{2.2}$$

where $m_\mathrm{L} = \frac{-\ln 2}{\ln(\cos \Phi_{1/2})}$ is Lambert's mode number, $\Phi_{1/2}$ is the semi-angle of half power, and ϕ is the angle of the reception (PD) with respect to the transmitter (LED). The maximum irradiated power occurs at $\phi = 0$.

The photodetection of a Photodetector (PD) with area A_d is modeled according to its effective area of incident collecting radiation at angles Ψ smaller than the Field of View (FOV), expressed as

$$A_\mathrm{eff}(\Psi) = \begin{cases} A_\mathrm{d}\cos\Psi & \text{for } 0 \leq \Psi \leq \pi/2 \\ 0 & \text{for } \Psi > \pi/2. \end{cases} \tag{2.3}$$

A large area for photodetection could collect more power but it also increases impairments such as manufacturing cost, increase the capacitance junction, reduce the bandwidth, and increase the PD noise power [6]. In order to increase the collecting area, a non-imaging concentrator can be used. The optical gain g is given by (2.4), where n_i is the concentrator internal refractive index and $\Psi_\mathrm{c} \leq \pi/2$ is the FOV. Figure 2.4 illustrates a geometry for a LOS VLC.

$$g(\Psi) = \begin{cases} \frac{n_i^2}{\sin^2 \Psi_\mathrm{c}} & \text{for } 0 \leq \Psi \leq \Psi_\mathrm{c} \\ 0 & \text{for } \Psi > \Psi_\mathrm{c}. \end{cases} \tag{2.4}$$

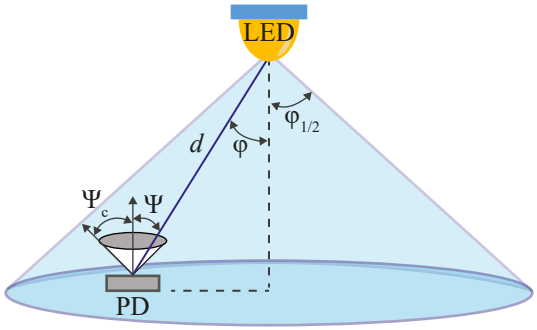

Figure 2.4. Geometry of a LOS VLC link. The DC gain for the presented communication link is determined by (2.5).

Finally, for a VLC link with a Lambertian source, the receiver with a possible optical bandpass filter of transmission T_s, lenses with a non-imaging concentration gain $g(\Psi)$, and a link length d, the DC LOS channel gain, for $0 \leq \Psi \leq \Psi_\mathrm{c}$, is given by

$$H_\mathrm{los} = \frac{A_d\,(m_\mathrm{L}+1)}{2\pi d^2}\cos^{m_l}(\phi) T_\mathrm{s}(\Psi) g(\Psi)\cos\Psi. \tag{2.5}$$

In case of $\Psi > \Psi_\mathrm{c} = \pi/2$, the H_los gain is zero. The LOS received power is determined as

$P_{\mathrm{r-los}} = H_{\mathrm{los}} \times P_{\mathrm{LED}}$.

For a Non-Line-of-Sight Propagation (NLOS) visible light propagation, the reflections gains (altogether $H_{\mathrm{n-los}}$ or for individual reflection $H_{\mathrm{reflection}}$) due to multipath may be considered in the modeling. The received power for the non-LOS scenario is

$$P_{\mathrm{r-nlos}} = (H_{\mathrm{los}} + H_{\mathrm{n-los}})\, P_{\mathrm{LED}} \tag{2.6}$$

$$= \left(H_{\mathrm{los}} + \sum_{\mathrm{reflection}} H_{\mathrm{reflection}} \right) P_{\mathrm{LED}}. \tag{2.7}$$

2.1.4. Photodetection Modeling and Noise

For a LOS link, the received current signal at the output of the PD I_{pd}(t) is given by

$$I_{\mathrm{pd}}(t) = \gamma H_{\mathrm{los}} P_{\mathrm{LED}}(t) + w(t), \tag{2.8}$$

where γ is the photodetector responsivity and $w(t)$ is the overall photodetection noise [47, 57]. The ratio between the desired signal's level (P_{signal}) and the noise's level (P_{noise}) of the received signal can be quantified as the Signal-to-Noise Ratio (SNR), frequently stated in dB. Considering the noise as a random variable N_0, the SNR is defined depending on whether the signal is a constant (s) or a random variable (S) and expressed as

$$\mathrm{SNR} = \frac{P_{\mathrm{signal}}}{P_{\mathrm{noise}}} = \frac{s^2}{\mathbb{E}(N_0)} = \frac{\mathbb{E}(S^2)}{\mathbb{E}(N_0^2)}, \tag{2.9}$$

where $\mathbb{E}(\cdot)$ refers to the expected value. As is typically the case, if the noise has an expected value of zero, the denominator represents the noise's variance or the square of its standard deviation σ^2.

The three main noise types associated with VLC systems are shot noise, thermal noise, and dark current noise [41]. Shot noise is produced by the fluctuation of the arriving photons that reach the PD overtime periods. The quantum shot noise, generated by the light source, is modeled as a Poisson distribution with variance defined as

$$\sigma^2_{\mathrm{q-shot}} = 2qI_{\mathrm{pc}}B_{\mathrm{pd}}, \tag{2.10}$$

where q denotes the electronic charge, $I_{\mathrm{pc}} = \gamma P_r$ is the photo-current, and B_{pd} is the PD effective bandwidth.

The background shot noise is caused by the light of the environment (natural and artificial light) that hits the PD. The background noise is independent of the wavelength and is modeled as an Additive White Gaussian Noise (AWGN) with variance given by [41]

$$\sigma^2_{\mathrm{bg-shot}} = 2qB_{\mathrm{pd}}\gamma P_{\mathrm{bg}}, \tag{2.11}$$

where P_{bg} is the background received power.

In VLC, the thermal noise, also known as Johnson-Nyquist noise, is caused by the free-charge fluctuation defined by the Brownian motion. The thermal noise is proportional to the temperature (T_{e}) and resistance (R_{L}) of the PD material. Moreover, in IM/DD, the thermal noise can be modeled as an AWGN with zero-mean and the variation expressed as [6]

$$\sigma^2_{\mathrm{therm}} = \frac{4\kappa T_{\mathrm{e}} B_{\mathrm{pd}}}{R_{\mathrm{L}}}, \tag{2.12}$$

where $\kappa = 1.380649 \times 10^{-23}\mathrm{m}^2\mathrm{kgs}^{-2}\mathrm{K}^{-1}$ is the Boltzman constant. The variance of thermal noise is generally lower than the shot noises.

The dark noise is associated with the reverse current (dark current I_{d}) of the photodiode in the absence of light, in which free electrons are generated randomly [41]. Closely related to the band-gap of the PD material, silicon (Si) and indium gallium arsenide (InGaAs), with large band-gap, presents a lower dark noise if compared with germanium (Ge)-based PD. The dark noise can be mathematically expressed as

$$\sigma^2_{\mathrm{dark}} = 2qB_{\mathrm{pd}}I_{\mathrm{d}}. \tag{2.13}$$

The SNR of the received signal is proportional to the received optical power P_{r} given by

$$\mathrm{SNR} = \frac{\gamma^2 H^2_{\mathrm{los}} P^2_{\mathrm{r}}}{R_{\mathrm{b}} N_0}, \tag{2.14}$$

where N_0 is the noise power spectral density modeled as an AWGN and R_{b} is the bit rate.

2.2. Orthogonal Frequency Division Multiplexing in VLC Systems

The phenomenon known as multipath, which is the forerunner of Intersymbol Interference (ISI), is characterized by the receiving of several copies of a signal with differing amplitudes and delays. The multipath spreading of the channel exceeds the period of the transmitted symbol when communication rates are higher than those associated to the various channel delays, requiring the adoption of methods to lessen the signal distortion caused by the ISI [58].

The performance of communications systems is strongly related to the modulation techniques. Commonly used in VLC systems, Single-carrier Modulation (SCM) and carrierless modulations, such as Phase Amplitude Modulation (PAM) [59, 60], PPM [51], and Carrierless Amplitude Phase Modulation (CAP) [61] modulations, exploits only one signal frequency to transmit data symbols and can achieve high data rates, with a simply implemented transmitter

but a complex equalization at the receiver to combat ISI and impairments of signal, as well as a lower spectral efficiency if compared with Multicarrier Modulation (MCM) [62].

Higher throughput can be obtained by using numerous spaced carriers in a Frequency Division Multiplexing (FDM) scheme. However, if the orthogonality between the subcarriers is obtained, then for conveying the same information, a less effective bandwidth is required, and consequently, the spectral efficiency increases [63].

Transmission with multiple carriers becomes a more appealing option when the available spectrum is divided into a number of orthogonal sub-channels since it significantly decreases the complexity of single-carrier equalization due to the resulting nearly flat frequency response of each sub-channel. First proposed in [64], OFDM is an MCM that divides the frequency spectrum into sub-channels, and the sub-carriers are orthogonal with each other [65]. OFDM modulation can achieve high-speed data rates and, due to it, is applied in broadband wireless and wireline communication systems, such as Digital Video Broadcasting (DVB), Long-Term Evolution (LTE), 5G new-radio, and PLC [66, 67].

This section is devoted to the explanation of the principles of the OFDM, the DCO-OFDM used in this work, and the OFDM figure of metrics.

2.2.1. Orthogonal Frequency Division Multiplexing Principles

2.2.1.1. Orthogonality and OFDM Transmitter and Receiver

Two time-limited ($0 < t < T_{\text{sym}}$) complex exponential signals $\left\{e^{j2\pi f_k t}\right\}_{k=0}^{N-1}$ representing different OFDM carriers at the central frequency $f_k = k/T_{\text{sym}}$ are considered orthogonal if the integral of the products for their common fundamental period is zero, as given by [1])

$$\begin{aligned}\frac{1}{T_{\text{sym}}}\int_0^{T_{\text{sym}}} e^{j2\pi f_k t}e^{-j2\pi f_i t}dt &= \frac{1}{T_{\text{sym}}}\int_0^{T_{\text{sym}}} e^{j2\pi \frac{k}{T_{\text{sym}}}t}e^{-j2\pi \frac{i}{T_{\text{sym}}}t}dt \\ &= \frac{1}{T_{\text{sym}}}\int_0^{T_{\text{sym}}} e^{j2\pi \frac{(k-i)}{T_{\text{sym}}}}dt \\ &= \begin{cases}1, & \forall \text{ integer } k=i \\ 0, & \text{otherwise}\end{cases}\end{aligned} \tag{2.15}$$

In order to avoid intersymbol interference, orthogonality is mandatory among the sub-carriers. Therefore, for OFDM symbols the discrete samples must be $t = nT_{\text{s}} = nT_{\text{sym}}/N$, where N is the number of sub-carriers. Then (2.15) becomes

$$\begin{aligned}\frac{1}{N}\sum_{n=0}^{N-1} e^{j2\pi\frac{k}{T_{\text{sym}}}\cdot nT_s} e^{-j2\pi\frac{i}{T}\cdot nT_s} &= \frac{1}{N}\sum_{n=0}^{N-1} e^{j2\pi_{T_{\text{sym}}}\cdot\frac{nT}{N}} e^{-j2\pi_{T_{\text{ssm}}}\cdot\frac{nT_{\text{sym}}}{N}} \\ &= \frac{1}{N}\sum_{n=0}^{N-1} e^{j2\pi\frac{(k-i)}{N}n} \\ &= \begin{cases} 1, & \forall \text{ integer } k=i \\ 0, & \text{otherwise} \end{cases}\end{aligned} \tag{2.16}$$

For a conventional OFDM, binary data streams or bitstreams D_{in} are converted from serial-to-parallel (S/P) streams each composed of $\log_2(M)$ bits, where M is the cardinality of the mapping. Then, N symbols are generated and are carried out by different sub-carrier. Considering a single carrier as a comparison (T_{s}-long and bandwidth B), the S/P conversion in OFDM provokes an extension of the signal period from T_{s} for N symbols is increased to NTs, forming a single OFDM signal of $T_{\text{sym}} = NT_{\text{s}}$, and consequently, each carrier bandwidth has a decreased bandwidth of $B_{\text{W}} = B/N$. Let $X_l[k]$ be the mapped symbol, where l is the transmitted symbol and k is the subcarrier, the baseband OFDM signal in the continuous time is given by

$$x_l(t) = \sum_{l=0}^{\infty}\sum_{k=0}^{N-1} X_l[k] e^{j2\pi f_k(t-lT_{\text{sym}})} \tag{2.17}$$

By sampling the continuous-time baseband OFDM signal at $t = lT_{\text{sym}} + nT_{\text{s}}$, where $T_{\text{s}} = T_{\text{sym}}/N$ (consequently $f_k = k/T_{\text{sym}}$ the discret OFDM baseband signal is given by

$$x_l[n] = \sum_{k=0}^{N-1} X_l[k] e^{j2\pi kn/N} \quad \text{for} \quad n = 0, 1, \ldots, N-1 \tag{2.18}$$

It is important to notice that (2.18) reveals to be the Inverse Discrete Fourier Transform (IDFT) of the data symbols and can be efficiently computed by an Inverse Fast Fourier Transform (IFFT) [68]. Not taking into account the effects of the channel, the discrete transmitted symbol $X_l[k]$ can be recovered from (2.18) by performing at the receiver side the Discrete Fourier Transform (DFT), or as a more computationally efficient approach, the Fast Fourier Transform (FFT), as

$$\begin{aligned} Y_l[k] &= \sum_{n=0}^{N-1} y_l[n] e^{-j2\pi kn/N} \\ &= \sum_{n=0}^{N-1} \left\{ \frac{1}{N}\sum_{i=0}^{N-1} X_l[i] e^{j2\pi in/N} \right\} e^{-j2\pi kn/N} \\ &= \frac{1}{N}\sum_{n=0}^{N-1}\sum_{i=0}^{N-1} X_l[i] e^{j2\pi(i-k)n/N} = X_l[k] \end{aligned} \tag{2.19}$$

Fig. 2.5 illustrates a typical realization of orthogonality among the OFDM subcarriers. The time-domain baseband OFDM signal is composed of N orthogonal overlapped subcarriers, equally spaced by $\Delta_{\mathrm{f}} = 1/T_{\mathrm{sym}}$. Each subcarrier is centered at a frequency $f_k = k/T_{\mathrm{sym}} = k/(NT)$, where $k = 0$ represents the DC subcarrier and $k = N/2$ denotes the Nyquist tone.

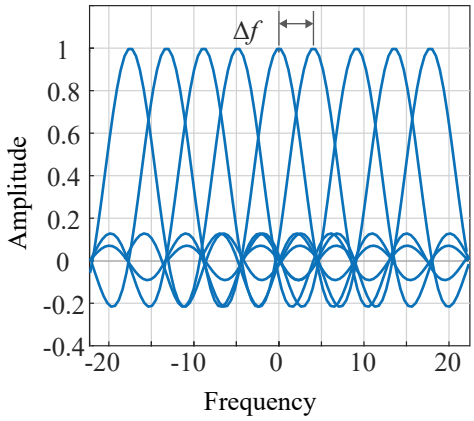

Figure 2.5. Illustration of the Orthogonality among the OFDM subcarriers. The illustration shows the frequency gap Δ_f between the subcarriers.

Fig. 2.6 shows the (a) transmitter and receiver baseband OFDM. Each block will be described in the following subsections.

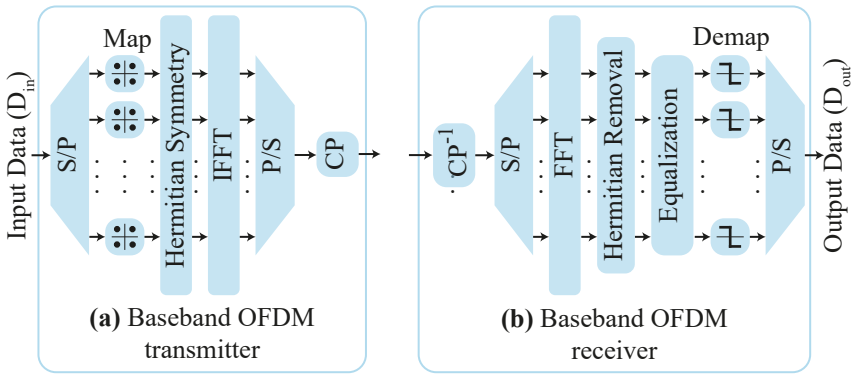

Figure 2.6. Block diagram of the baseband OFDM. (a) OFDM transmitter. (b) OFDM receiver.

2.2.1.2. Multipath Fading and Cyclic Prefix

Signals traveling over two or more routes to the receiver (antenna, PD, etc.) owing to propagation barriers are referred to as dispersive channels. The impulse response $h(t)$ of the channels appears to have a decaying characteristic, as shown in Fig. 2.7a1. Such channels are well known to be frequency-selective and also cause impairments in communication due to ISI, as shown in Fig. 2.7a2, where the response of the previous symbol interferes with the subsequent and may disrupt the OFDM signals' orthogonality.

The application of the interval symbol T_{G} can be used to easily solve this problem by separating the symbols in time (Fig. 2.7a3), consequently, the symbol time increase to $T = T_{\mathrm{sym}} + T_{\mathrm{G}}$. OFDM is resistant to ISI due to the employment of the Cyclic Prefix (CP), which copies a period interval T_{G} of the last OFDM samples into the beginning of the frame. The linear convolution between the channel response and the OFDM symbol is transformed into a circular convolution by applying the CP. The CP period must be larger than the channel dispersive impulsive response [69]. Fig. 2.7b illustrates an OFDM signal and frequency with the CP application.

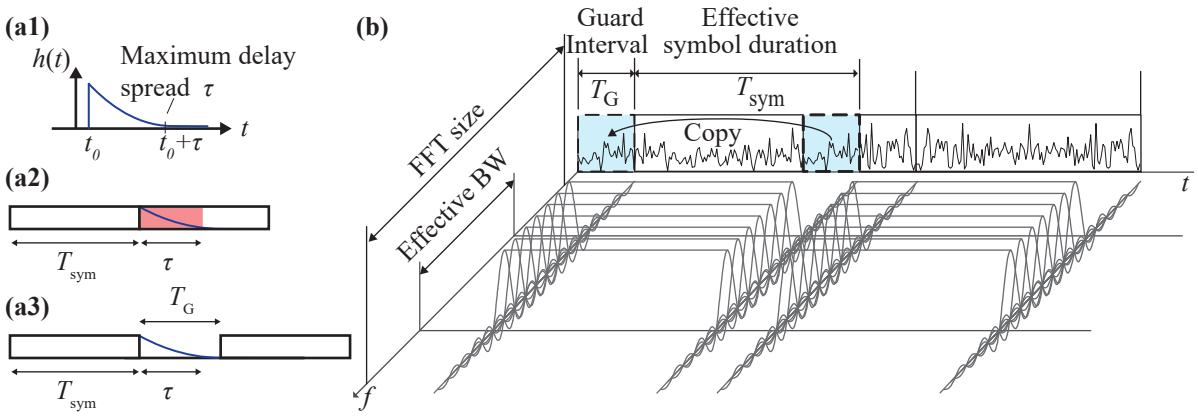

Figure 2.7. Guard interval in the OFDM. (a.1) Channel impulse response of a dispersive channel. (a.2) Example of OFDM symbols interfering with each other due to the dispersive channel response. (a.3) Application of the guard interval in order to avoid ISI. (b) A time-frequency representation of an OFDM signal with a cyclic prefix (adapted from [1]).

2.2.1.3. Hermitian Symmetry

Hermitian symmetry (HS) is a property of OFDM signals where the subcarriers exhibit a particular symmetrical structure. To be more precise, it indicates that the subcarriers have values that are conjugately symmetric with respect to the center frequency. Simply explained, the value of another subcarrier will correspond to the complex conjugate of one subcarrier if it is placed on the side of the center frequency opposite from the center frequency. The design and operation of OFDM systems heavily rely on this HS feature. It permits efficient use of the spectrum that is available, streamlines the installation procedure, and improves the system's ability to fend against interference and channel distortions. The main reason for utilizing the HS in OFDM system for optical application is that the output of the IFFT processing is real, even though its input is complex.

To achieve a real baseband OFDM signal, imposed by the IM/DD, generally, the Hermitian Symmetry (HS), or Complex Conjugate-Symmetry, is applied as input of the IFFT. The HS has to follow the property:

$$X[N-n] = X^*[n], \tag{2.20}$$

where N is the size of the inverse Fourier transform block and * denotes the complex conjugate operation. Hence, HS in OFDM can be proven by inserting (2.20) into the FFT transform equation as (2.21)-(2.24).

$$X[n] = \sum_{k=0}^{N-1} x[k] e^{-j\frac{2\pi}{N}kn} \tag{2.21}$$

$$X[N-n] = \sum_{k=0}^{N-1} x[k] e^{-j\frac{2\pi}{N}k[N-n]} \tag{2.22}$$

$$= \sum_{k=0}^{N-1} x[k] e^{-j2\pi k} e^{j\frac{2\pi}{N}kn} \tag{2.23}$$

$$X[N-n] = \sum_{k=0}^{N-1} \left(x[k] e^{-j\frac{2\pi}{N}kn} \right)^* = X^*[n] \tag{2.24}$$

It is straightforward to observe that the same is valid for the IFFT operation. Then in order to satisfy the OFDM real value constraint, the HS rules (2.25) and (2.26) have to be assured.

$$X[0] = X[N/2] = 0, \text{ and} \tag{2.25}$$

$$X[k] = X[N-k]^*, \text{ for } 0 < k < N/2 \tag{2.26}$$

Due to HS in $X[k]$, (2.18) can be simplified by

$$x[n] = \frac{2}{N} \sum_{k=1}^{N/2-1} \Re \left(X[k] e^{j\frac{2\pi}{N}kn} \right), \tag{2.27}$$

where $\Re$ represents the real value extraction.

2.2.1.4. Channel estimation and Equalization

At the receiver side, the CP is removed, and the next stages are processed in parallel. The electric converted signal at this can be determined as

$$y[n] = x[n] \circledast h[n] + w[n], \tag{2.28}$$

where $\circledast$ denotes the linear convolution operation. Thereafter, the FFT digitally demultiplexes each subcarrier mapping symbol, converting them from time to frequency domain. Hence, each symbol can be expressed as

$$Y[k] = \mathcal{F}\{y[n]\} = H[k] \cdot X[k] + W[k], \tag{2.29}$$

where $\mathcal{F}\{\cdot\}$ denotes the FFT operation and $H[k]$, $X[k]$, and $W[k]$ represent in the frequency domain the channel frequency response, the transmitted mapped symbols, and the noise, respectively.

Equalization is a technique used to mitigate the effects of channel impairments such as multipath fading and frequency selective fading. By using the proper compensation to mitigate the channel distortion, it seeks to restore the originally transmitted signal. The correct detection of the received signal is highly dependent on the correct channel estimation. For frequency selective channels, $X[k]$ is correctly predicted ($\hat{X}[k]$) with channel estimation techniques, such as Least-Square (LS), and subsequently, a one-tap equalizer.

In a communication system, a pilot signal refers to a recognized reference signal that is transmitted concurrently with the data signal. For channel estimation and equalization, the pilot signal is utilized. Pilots are essential to the equalization process as they offer a reliable reference that is used to calculate the channel response and modify the equalizer coefficients. The receiver can evaluate the received signal and determine the channel parameters, such as amplitude, phase, and frequency response, by sending pilot symbols at regular intervals. In synthesis, by accounting for channel distortions and enhancing the received signal, the addition of pilot signals to the equalization process provides more stable and dependable communication.

The goal of the least-square approach for channel estimation is to minimize the square distance of the received signal ($Y_p[k]$) and the original (transmitted) signal ($X_p[k]$) for the pilot subcarriers (p) [70, 71]. The LS formulation is determined by the maximum likelihood expressed as

$$\hat{H}_p^{\mathrm{LS}}[k] = \arg\min_{H_p} \|Y_p[k] - H_p[k]X_p[k]\|_2^2 . \tag{2.30}$$

Therefore, the LS estimation over the pilot subcarriers can be obtained by

$$\hat{H}_p^{\mathrm{LS}}[k] = \mathrm{diag}\left[\hat{H}_p^{\mathrm{LS}}[k]\right] = \frac{Y_p[k]}{X_p[k]}. \tag{2.31}$$

According to the structure of the channel estimation, the received symbols are then equalized using the estimated flat channel for each subcarrier by doing

$$Y_{\mathrm{EQ}}[k] = \hat{X}[k] = \frac{Y[k]}{\hat{H}^{\mathrm{LS}}[k]}. \tag{2.32}$$

Following the equalization, the demodulation is performed and the data stream is detected. The communication figure of metrics can assess the quality of the transmission and detection.

2.2.2. Direct Current Offset OFDM

In VLC systems, the OFDM-modulated signals are constrained to have real-valued and non-negative amplitudes. Various OFDM schemes have been proposed for VLC IM/DD systems in order to satisfy these inevitable constraints, such as Direct Current Optical OFDM (DCO-OFDM) [72, 73], Asymmetrically Clipped Optical OFDM (ACO-OFDM) [74], Flipped OFDM (Flip-OFDM) [75], Pulse Amplitude Modulated Discrete Multitone (PAM-DMT) [76], Layered ACO-OFDM (LACO-OFDM) [77], among others. This work's focus is on the DCO-OFDM scheme.

Fig. 2.8 illustrates the block diagram of a conventional DCO-OFDM physical layer. The passband OFDM signal $x(t)$ is amplified by a factor α and biased by a current I_{bias} to avoid clipping. The LED current is given by

$$I_{\text{LED}}(t) = I_{\text{bias}} + [\alpha \times x(t)]\,. \tag{2.33}$$

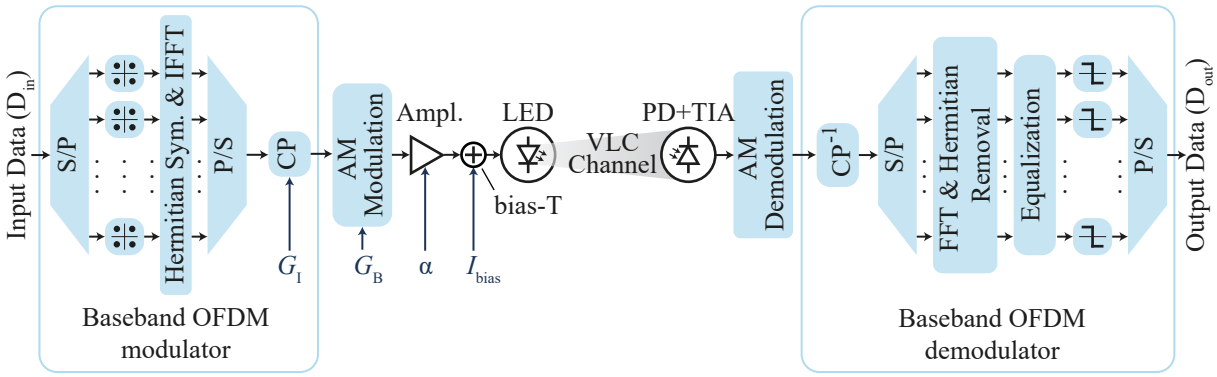

Figure 2.8. DCO-OFDM block diagram for the VLC physical layer.

An Optical Modulation Index (OMI) that relates the maximum LED current (I_{max}) and the I_{bias} can, therefore, be defined as

$$\text{OMI} = \frac{I_{\text{max}} - I_{\text{bias}}}{I_{\text{bias}}} = \frac{\alpha \cdot \max[x(t)]}{I_{\text{bias}}}. \tag{2.34}$$

The signal is converted to the optical domain by the LED, which is transmitted through the channel. The optical signal is then attenuated according to the photodetection and channel characteristics $h(t)$, as mentioned in Section 2.1. At the photodetection, the noise (w), generally modeled as an AWGN, are likely to corrupt the signal.

2.2.3. OFDM Performance Metrics

The metrics used in this work to assess or characterize the OFDM modulation are explained below.

2.2.3.1. Bit Error Rate

The Bit Error Rate (BER) is a measure of the quality of a digital communication channel or data transmission system. It is defined as the number of bits transmitted that are received in error divided by the total number of bits transmitted [78]. In other words, the BER is the ratio of the number of bits received in error to the total number of bits transmitted over a specific period. A lower BER value indicates better transmission quality and a higher BER value indicates poor quality.

2.2.3.2. Error Vector Magnitude

The Error Vector Magnitude (EVM) is a figure of merit for assessing the quality of digitally modulated communication signals. It expresses the average difference between the expected (transmitted) and the received complex symbols [79, 80] or in other words, the EVM collects the mean of the sum of the squared errors. This metric is determined, in RMS value, as

$$\mathrm{EVM} = \sqrt{\frac{1}{N_{\mathrm{symb}}} \sum_{t=1}^{N_{\mathrm{f}}} \frac{\sum_{k=0}^{N-1} \left| X[k] - \hat{X}[k] \right|^2}{\sum_{k=0}^{N-1} |X[k]|^2}}, \tag{2.35}$$

where N_{symb} is the number of transmitted symbols. This metric is commonly presented in decibels by converting $\mathrm{EVM}_{\mathrm{dB}} = 10 \times \log_{10}(\mathrm{EVM})$. When the power of the channel noise and the distortion of the received signals both rises, the EVM value also is prone to increase.

The EVM can be related to the BER and the SNR for a given multi-modulation system (Binary Phase Shift Keying (BPSK) and Quadrature Amplitude Modulation (QAM), for example) [79]. From the definition of the EVM in (2.35), it is unambiguous that the EVM consists of the difference in magnitude between the measured and ideal OFDM symbols, both normalized. For a channel modeled as an AWGN, the error magnitude can be simplified in terms of the noise in-phase $n_{\mathrm{I},t}$ and quadrature $n_{\mathrm{Q},t}$ as

$$\mathrm{EVM}_{\mathrm{RMS}} = \left[\frac{\frac{1}{T} \sum_{t=1}^{T} \left[|n_{I,t}|^2 + |n_{Q,t}|^2 \right]}{P_0} \right]^{\frac{1}{2}} \tag{2.36}$$

where P_0 is the power of the transmitted constellation. Nevertheless, if a large symbol stream is taken into account, i.e., in which the number of symbols T is much greater than the number of unique symbols in the constellation, their unnormalized amounts can be used to substitute the

ratio of the normalized noise power to the normalized power of the ideal constellation by the SNR as

$$\mathrm{EVM_{RMS}} \approx \left[\frac{1}{\mathrm{SNR}}\right]^{\frac{1}{2}} = \left[\frac{\mathbb{E}(N^2)}{\mathbb{E}(S^2)}\right]^{\frac{1}{2}} \tag{2.37}$$

Therefore, the SNR can be approximated as the $\mathrm{EVM_{RMS}}$ value as $\mathrm{SNR} \approx \frac{1}{\mathrm{EVM_{RMS}}^2}$ and in decibels simply as $\mathrm{SNR} \approx -\mathrm{EVM}$. The EVM values can vary for a certain fixed BER value, which means that the EVM metric is more sensitive to variation in the in-phase/quadrature constellation, even if the symbol is correctly detected. It is also possible to approximate the BER with the EVM for such modulations as [79]

$$\mathrm{BER} \approx \frac{2\left(1-\frac{1}{L}\right)}{\log_2 L} Q\left[\sqrt{\left[\frac{3\log_2 L}{L^2-1}\right]\frac{2}{EVM_{\mathrm{RMS}}^2 L}}\right], \tag{2.38}$$

where $L = \log_2(M)$ is the numbers of levels of the M-ary modulation and $Q[\cdot]$ refers to the Gaussian co-error function given by $Q(x) = \int_x^\infty \frac{1}{\sqrt{2\pi}} e^{\frac{-y^2}{2}} dy$.

2.2.3.3. Peak-to-Average Power Ratio

Signals produced by OFDM multicarrier modulation have a larger excursion range compared with its average. This is caused by the time domain summation of the different narrowband subsymbols that together make up these signals, which can occasionally be high enough to noticeably expand the gap between the maximum and average values of the OFDM symbols. This metric is well known as PAPR. The performance of such a system depends on the PAPR primarily in the presence of nonlinear distortions introduced by devices like Analog-to-Digital Converter (ADC) and primarily power amplifiers, which are typically designed to operate close to the area from saturation to high yield. The signal's wide extension is prone to exceed the LED dynamic region, i.e., saturates the signal, and consequently generates nonlinear effects that impair the communication performance. The PAPR is defined as

$$\mathrm{PAPR} = \frac{\|\max\{x[n]\}\|^2}{\mathbb{E}\left(x[n]^2\right)}. \tag{2.39}$$

In order to reduce the OFDM PAPR, many studies were conducted to lower the OFDM PAPR. In the literature, the approaches are classified into distortion and distortionless techniques [81,82]. The distortion techniques clip the signal's high peaks before transmitting, while the distortionless methods modify the characteristics of the signal in the time or frequency domain to lower the PAPR.

In the clipping technique for PAPR reduction, the signal amplitude is ensured to not surpass a maximum threshold amplitude, while the resulting signal's phase is preserved. The ease with

which this approach can be used contrasts sharply with the distortions that spectral broadening introduces. The higher the clipping rate, the bigger the PAPR reduction. However, higher degrees of clipping have a tendency to degrade system performance by introducing distortions to the signal (reducing SNR), highlighting an inefficiency in this approach [83].

This thesis also conducts a comparative analysis between conventional OFDM and Constant-Envelope OFDM, classified as a distortionless PAPR reduction approach.

2.2.4. Constant-Envelope OFDM

First proposed in [84], the constant-envelope OFDM (CE-OFDM) is an approach that involves reducing the PAPR of OFDM symbols in order to remove distortions generated by devices with nonlinear characteristics like power amplifiers in radiofrequency systems. The CE-OFDM is related to the passband signal generation, achieving low PAPR by modulating the phase of an electrical carrier with typical baseband OFDM signals.

In a conventional OFDM system, the baseband signal is modulated with an amplitude-modulation over a carrier frequency f_c given as

$$y(t) = \Re\{x(t)e^{j2\pi f_\mathrm{c} t}\} = A_x(t)\cos[2\pi f_\mathrm{c} t + \phi_x(t)] \tag{2.40}$$

where $A_x(t) = |x(t)|$ and $\phi_x(t) = \arg(x(t))$. Whereas the CE-OFDM signal generation is performed considering a carrier frequency of f_c and can be expressed as

$$\begin{aligned} y(t) &= \Re\left\{As(t)e^{j2\pi f_c t}\right\} \\ y(t) &= A\cos\left[2\pi f_c t + \alpha x(t)\right] \end{aligned} \tag{2.41}$$

where α is the phase shift and A is the amplitude of the modulated signal and its constant average power is equivalent to $A^2/2$. Since this is equivalent to a phase-modulated sine wave, the signal is free of high amplitude fluctuations and the PAPR is only 3 dB.

Fig. 2.9 depicts the waveforms of (a) baseband OFDM, (b) bandpass OFDM and (c) bandpass CE-OFDM. According to the generated signals, the OFDM signal has a strong PAPR whereas the CE-OFDM signal has the desired constant envelope feature.

From (2.41), the phase shift can be set as $\alpha = 2\pi h C_N$, where $2\pi h$ is the phase modulation index and C_N normalizes the variance of the OFDM signal $x(t)$. Therefore, by defining $\phi = 2\pi h C_N x(t)$ the variance of ϕ is given by $\sigma^2 = (2\pi h)^2$, which is dependent only on the set h. (2.41) turns out to be

$$s_\mathrm{Tx}(t) = A\cos\big(2\pi f_\mathrm{c} t + 2\pi h \cdot x(t)\big), \tag{2.42}$$

where the bit and symbol energy are $E_\mathrm{b} = A^2T/(2N\log_2(M))$ and $E_\mathrm{s} = A^2T/2$, respectively.

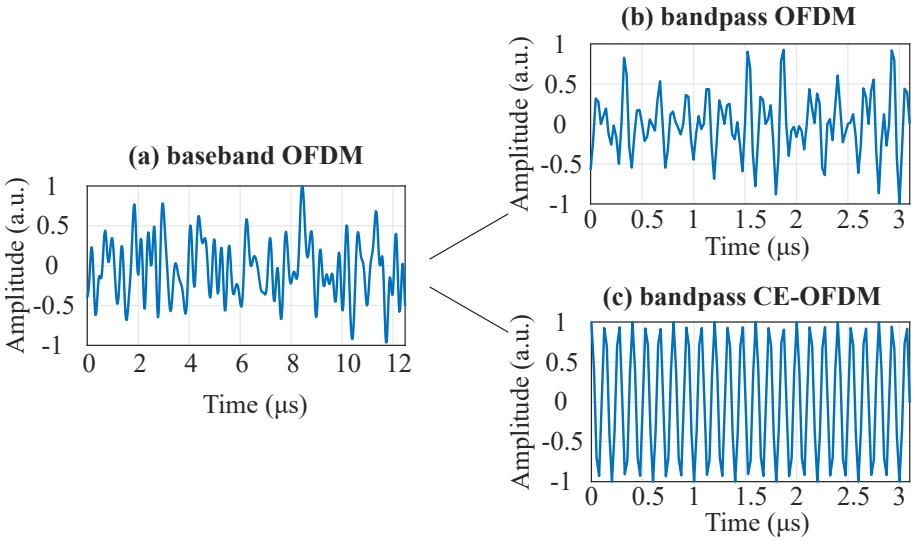

Figure 2.9. Waveforms of (a) baseband OFDM, (b) passband OFDM modulated in amplitude, and (c) passband OFDM modulated in phase (CE-OFDM).

The root-mean-square of the bandwidth of the phase-modulated OFDM is defined as at least the bandwidth of the baseband signal (B_{W}) and is given by [85]

$$B_{\mathrm{RMS}} = \max(2\pi h, 1) \cdot B_{\mathrm{W}}. \tag{2.43}$$

Fig. 2.10 depicts the block diagram for the CE-OFDM physical layer. The baseband real-time signal generation is the same as (2.27). To obtain constant envelope OFDM signals $c(t)$, the phase of the carrier is modulated and can be expressed as Fig. 2.10 shows in the CE-OFDM block diagram.

The phase index $2\pi h$ plays an important role in the trade-off between SE and system performance as can be seen in (2.42). Low phase modulation index values increase noise sensitivity, while high values improve system performance at the cost of increased bandwidth and, as a result, lower SE [86]. Excepting the passband to baseband conversion, the CE-OFDM signal detection is the same as the conventional OFDM detection. The Phase Modulation (PM) demodulation (Fig. 2.10) is evaluated by a discrete phase demodulator, implemented by an arctangent (ARC) processor, as suggested in [84]. A phase unwrapping is also utilized to minimize possible effects of phase ambiguities caused by phase offsets introduced by the communication channel [21].

2.3. Metaheuristic Optimization

Optimization is a process to search for the minimum or maximum of a given function [87]. In this process, there are goals to achieve and constraints to be satisfied. The goal of the optimization is to determine the parameters that will provide an optimum objective. Classical

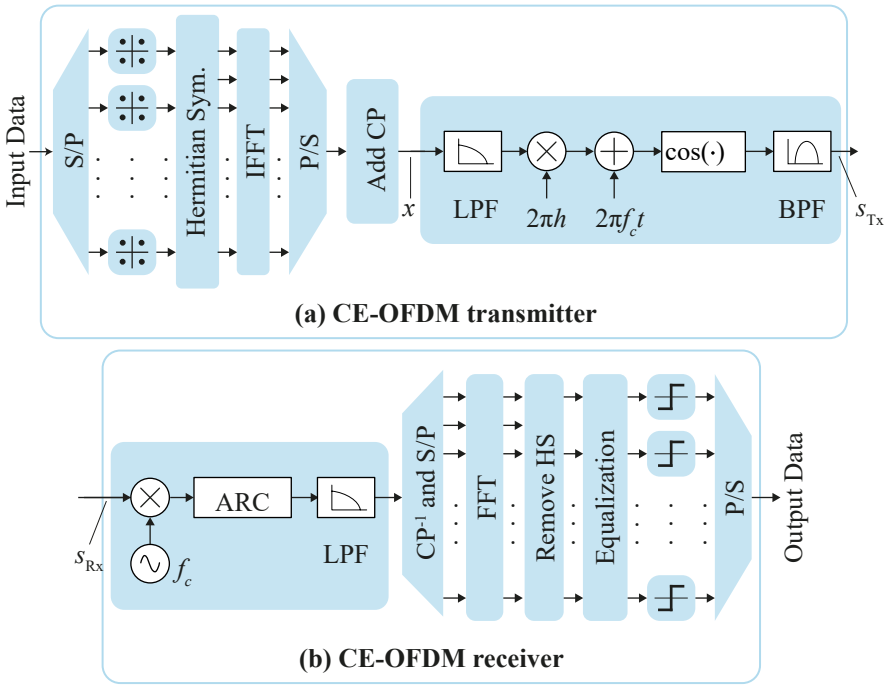

Figure 2.10. Constant envelope OFDM block diagram. (a) The CE-OFDM transmitter side and (b) the CE-OFDM receiver side.

search methods require the objective function to be differentiable. Problems that have some local optima, discontinuities, and restrictions in the search space present high complexity to such methods [88]. In the AI field there is a large number of nature-inspired techniques to solve a wide range of problems. In the field of soft computing, the main objective is to develop algorithms that are capable of solving inexact NP-complete problems that cannot run in a polynomial time. Some NP-hard problems could take a huge amount of time to search the entire search space (universe of possible solutions), which seems to be impractical. On the opposite way, the random search (brute force search) could provide a better solution but with an impairment in reliability. This problem paves the way for the application of metaheuristics which are systematic and stochastic techniques to solve the problem with an exact or feasible solution in a reasonable time [89]. Metaheuristic, also known as a nature-inspired algorithm, mimics nature to solve real-life problems. The optimization based on metaheuristics is capable to explore and exploit the search space using the search experience in a randomized fashion.

For single-objective metaheuristics, the main goal is to maximize or minimize the desired objective function (or fitness). The process of optimization searches for solutions that fulfill the constraints and rank the ones that provide better fitness value, and the best solution is chosen. Some problems with multiple objectives can be formulated as a single objective by applying weights and combining. On the contrary, the problems that cannot be combined may have the metaheuristic adapt to contemplate multiple solutions where each objective is considered as equally good [90]. This technique provides a Pareto front or Pareto frontier composed of a set of feasible solutions. The Pareto dominance is applied to define the solutions ranks or fronts

F_N, where N is the order in non-dominance [91,92]. This method states that, in a minimization problem, for a j-th objective function, a feasible solution $\overrightarrow{s}_1$ dominates the solution $\overrightarrow{s}_2$ if two conditions are satisfied: $\overrightarrow{s}_1$ is no worse than $\overrightarrow{s}_2$ in all objective function values and $\overrightarrow{s}_1$ is strictly better than $\overrightarrow{s}_2$ in at least one objective function value. These conditions can be mathematically expressed as

$$\forall j \in \{1, \ldots, k\}, f_j\left(\overrightarrow{s}_1\right) \leq f_j\left(\overrightarrow{s}_2\right), \tag{2.44}$$

and

$$\exists j \in \{1, \ldots, k\}, f_j\left(\overrightarrow{s}_1\right) < f_j\left(\overrightarrow{s}_2\right), \tag{2.45}$$

where k is the number of objective functions, and $f_j(\overrightarrow{s})$ is the j-th outcome of an objective function for a solution vector. For problems in which the goal is the maximization of the objectives, the inequality signs of (2.44) and (2.45) must be accordingly inverted.

Many multi-objective metaheuristic algorithms based on the evolution theory, based on trajectory, and inspired by nature have been extensively studied. The following subsections introduce fundamental concepts of the non-sorting genetic algorithms and the grey-wolf optimizer.

2.3.1. Non-dominated Sorting Genetic Algorithms

The GA is an optimization method based on the selection principle of Darwin's theory of evolution [93]. Each feasible solution of this algorithm is an individual. With the selection, mutation, and crossover operations, the NSGA-II solutions' convergence and diversity are achieved. The selection allows the best individuals to survive, and the evolved ones of each iteration transfer their genes to the next generations through the crossover operation [94]. The crossover rate, which represents the likelihood that two chosen parent individuals will experience crossover to create offspring individuals, is a parameter that influences the probability of applying the crossover operator during the reproduction process. In the search process, this operator strikes a balance between exploration and exploitation. The crossover rate is typically specified as a value between 0 and 1, where 0 indicates no crossover is conducted, and 1 indicates crossover is always applied, depending on the type of problem.

The individuals can also suffer mutations along iterations defining an offspring set (new solutions) Q_T in each iteration based on the parent (current) population P_T [95]. On the freshly produced offspring individuals, the mutation operator is frequently used following the crossover operation. It measures the risk that a chosen offspring would experience mutation, bringing about arbitrary alterations to its genetic makeup. The mutation rate is commonly expressed as a number between 0 and 1, with 0 denoting no mutations and 1 denoting constant mutation.

The NSGA-II is a multi-objective version of the GA optimizer. This approach uses non-dominance in order to rank the best solutions. In a situation where the number of members of

the fronts in the subsequent generation is greater than the maximum number of members of the population (overall solutions), the last accepted front must be split. Unlike its precursor [96], NSGA-II considers the Crowding Distance Criteria (CD) to estimate the density of solutions close to each i-th solution, in order to keep a good spread of NSGA-II and avoid local maxima or minima instead of finding the global one (see Fig. 2.11 (a)). Thus, the solution with a large CD means its position is in an area with less crowded solutions. To calculate the CD, the solutions are sorted per objective and the ones located at the extreme of the Pareto front are marked with infinite CD. The other solutions' CD values are defined as [2]

$$\mathrm{CD}(i) = \sum_{i=1}^{k_l} \frac{f_j^{i+1} - f_j^{i-1}}{f_j^{\max} - f_j^{\min}}, \tag{2.46}$$

where f_j^i is the j-th outcome of an objective function for the i-th solution/individual and, $f_j^{\max}$ and $f_j^{\min}$ are, respectively, the maximum and minimum values for the objective function among all the individuals. The solutions of the splitting rank according to the CD value (F3 in Fig. 2.11 (b))) and the ones with higher values are assigned to survive to the next generation (P_{T+1}) until the maximum members of the population are attained.

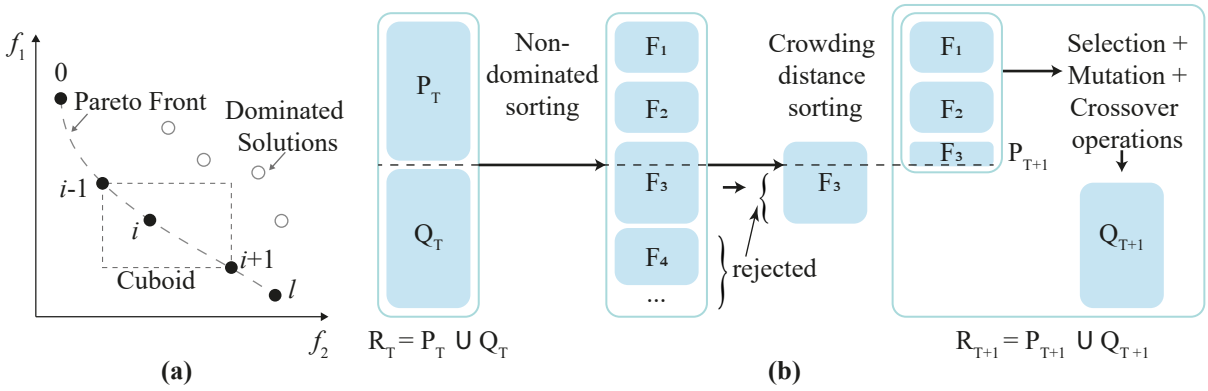

Figure 2.11. Non-sorting genetic algorithm II (adapted from [2]). (a) Crowding distance calculation. (b) NSGA-II procedure.

The selection operator is used to determine the more adapted members from the combined set of solutions, offspring, and parent, $R_T = P_T \cup Q_T$ to the next generation (P_{T+1}). Fig. 2.11 (b) illustrates the block diagram of the NSGA-II. Several selection methods were proposed such as rank, tournament, and roulette wheel [97]. The tournament selection is the most used that considers tournament involving two or three solutions and the solution with the best CD goes to the next generation. The better ranks are selected and, among the members with the same ranks, the ones with larger CDs are also selected for the next generation [98]. The pseudocode for the NSGA-II is given in Algorithm 2.1.

The Non-Sorting Genetic Algorithm III (NSGA-III) multi-objective optimization is an evolutionary algorithm that is capable to deal with many-objective problems. As its former version, the NSGA-II, NSGA-III uses the non-dominated sorting mechanism, but, in order to ensure di-

Algorithm 2.1. NSGA-II procedure (adapted from [2]).

Input: N_{pop}
Output: P_{t+1}
1: Initialize Population P_t
2: Generate random population: $P_t \leftarrow \texttt{RandomPopulation}(N_{\text{pop}})$
3: Evaluate objective values
4: Assign rank (level) based on Pareto (sort);
5: Generate child population;
6: Tournament selection;
7: Recombination and Mutation operations;
8: **for** $i = 1$ to g **do**
9: **for** Each Pareto Front and Child Population **do**
10: Assign rank (level) based on Pareto (sort);
11: Generate sets of nondominated solutions;
12: Determine crowding distance;
13: Loop (inside) by adding solutions to the next generation starting from the first front until N individuals;
14: **end for**
15: Select points on the lower front with high crowding distance values;
16: Create next generation;
17: Tournament selection;
18: Recombination and Mutation operations;
19: **end for**

versity in the solutions, instead of the crowding distance, it adopts a splitting front stage as a reference point approach. A predefined set of reference points are set over the objectives and the closer solutions are likely to be preserved [4, 99]. Algorithm 2.2 shows the pseudocode for NSGA-III.

2.3.2. Grey Wolf Optimization

The Grey Wolf Optimization (GWO) algorithm was inspired by the social hierarchy and hunting mechanism of the Grey Wolves and was originally proposed by Mirjalili et al. [100]. The first step of the GWO design is to define the social hierarchy among the wolves (solutions): the fitness of each solution is calculated individually, the solutions are ranked and the best three are marked as the alpha, beta, and delta; these wolves guide the optimization and are called leaders. The omega wolves are the solutions considered worse according to their fitness values and follow the leaders.

In the GWO, the prey is considered to be the optimal solution (or the best-found solution) in a single-objective optimization. The prey encircling, which is dependent on the grey wolf position $\overrightarrow{X}$, is modeled as

$$\overrightarrow{D} = |\overrightarrow{C} \cdot \overrightarrow{X_{\text{p}}}(l) - \overrightarrow{X}_t| \tag{2.47}$$

Algorithm 2.2. NSGA-III procedure (adapted from [4]).

Require: H processed reference points Z^s, parent population P_t
Ensure: P_{t+1}
1: $S_t \leftarrow \varnothing,\ i \leftarrow 1$;
2: $Q_t \leftarrow \texttt{Recombination}(P_t) \cup \texttt{Mutation}(P_t)$
3: $R_t \leftarrow P_t \cup Q_t$
4: $(F1, F2, ...) \leftarrow \texttt{NonDominatingSorting}(R_t)$;
5: **while** $|S_t| \geq N$ **do**
6: $\quad S_t \leftarrow S_t \cup F_i;\ i \leftarrow i + 1$;
7: **end while**
8: $F_l \leftarrow F_i$; ▷ Last front to be included
9: **if** $|S_t| = N$ **then**
10: $\quad P_t \leftarrow S_t$
11: **else**
12: $\quad P_t \leftarrow \bigcup_{j=1}^{l-1} F_j$;
13: $\quad K \leftarrow N - |P_{t+1}|$ ▷ Number of points to be chosen from F_l
14: $\quad \texttt{Normalize}(F^M, S_t, Z^r, Z^s)$ ▷ Normalize objectives and create a reference set Z^r
15: $\quad [\pi(s), d(s)] \leftarrow \texttt{Associate}(S_t, Z^r)$; ▷ Associate $s \in S_t$ with a reference point
16: $\quad \rho_j \leftarrow \sum_{s \in S_t / F_l} ((\pi(s) = j)\ ?\ 1\ :\ 0$ ▷ Compute niche count of reference point $j \in Zr$
17: $\quad \texttt{Nitching}(K, \rho_j, \pi(s), d(s), Z^r, F_l, P_{t+1})$ ▷ Choose K members one at a time from F_l to construct P_{t+1}
18: **end if**

$$\overrightarrow{X}_{t+1} = \overrightarrow{X_{\mathrm{p}} - l}_{\mathrm{p},t} - \overrightarrow{A} \cdot \overrightarrow{D}, \tag{2.48}$$

where $\overrightarrow{D}$ is the distance from the wolf to the prey, $\overrightarrow{X}_{\mathrm{p},t}$ is the position of the prey at iteration t, and $\overrightarrow{A}$ and $\overrightarrow{C}$ are coefficient vectors. These coefficient vectors are responsible for the exploration (search for prey) and exploitation (attacking the prey) of the algorithm that can be calculated as

$$\overrightarrow{A} = 2\overrightarrow{a} \cdot \overrightarrow{r_1} - \overrightarrow{a} \tag{2.49}$$

$$\overrightarrow{C} = 2 \cdot \overrightarrow{r_2} \tag{2.50}$$

where $\overrightarrow{a}$ linearly decreases from 2 to 0 along the course of iterations and $\overrightarrow{r_1}$ and $\overrightarrow{r_2} \sim \mathcal{U}(0, 1)$, where $\mathcal{U}$ denotes a uniform distribution that ranges from 0 to 1.

The optimal solution in the GWO is obtained by the encircling mechanism. For each iteration, the three best solutions are archived (X_α, X_β, and X_δ), which models the social hierarchy of the grey wolves and are used to update the wolves' positions, since they represent the closest positions to the prey at the moment. The hunting mechanism GWO is mathematically modeled by

$$\begin{aligned} \overrightarrow{D_\alpha} &= |\overrightarrow{C}_1 \cdot \overrightarrow{X_\alpha} - \overrightarrow{X}| \\ \overrightarrow{D_\beta} &= |\overrightarrow{C}_2 \cdot \overrightarrow{X_\beta} - \overrightarrow{X}| \\ \overrightarrow{D_\delta} &= |\overrightarrow{C}_3 \cdot \overrightarrow{X_\delta} - \overrightarrow{X}| \end{aligned} \tag{2.51}$$

$$\overrightarrow{X_1} = \overrightarrow{X_\alpha} - \overrightarrow{A_1} \cdot \overrightarrow{D_\alpha} \tag{2.52}$$

$$\overrightarrow{X_2} = \overrightarrow{X_\beta} - \overrightarrow{A_2} \cdot \overrightarrow{D_\beta} \tag{2.53}$$

$$\overrightarrow{X_3} = \overrightarrow{X_\delta} - \overrightarrow{A_3} \cdot \overrightarrow{D_\delta} \tag{2.54}$$

$$\overrightarrow{X}_{t+1} = \frac{\overrightarrow{X_1} + \overrightarrow{X_2} + \overrightarrow{X_3}}{3} \tag{2.55}$$

where $\overrightarrow{X_\alpha}$, $\overrightarrow{X_\beta}$, $\overrightarrow{X_\delta}$ denotes the position vector of the alpha, beta, and delta in the current population, respectively, $\overrightarrow{X}$ represents the grey wolf, and $\overrightarrow{D_\alpha}$, $\overrightarrow{D_\beta}$, $\overrightarrow{D_\delta}$ are the distance between the current candidate grey wolf and the best wolves, respectively. The exploration components $\overrightarrow{A}$ and $\overrightarrow{C}$ are fundamental in the GWO to search solutions along the possible search space. Fig. 2.12 (a) illustrates the grey wolf optimizer hunting mechanism. The random vector $\overrightarrow{A}$ ranges $[-2a, 2a]$ which makes probable the search agents to approximate and deviate from the prey. If the values of $|A| < 1$, the next position of the wolf $X(l+1)$ is between the current position and the prey (explore the local optimum solution). For values of $|A| > 1$ the wolf explores areas in the other direction of the prey (explore the global solution); this condition is defined to force the algorithm to explore the search area and avoid a stationary local solution (see Fig. 2.12 (b)). The random vector $\overrightarrow{C}$ ranges $[0, 2]$, and its main function is to provide a weight that deemphasizes ($C < 1$) or emphasizes ($C > 1$) the effect of the prey in defining the distance.

The Multi-objective Grey Wolf Optimization (MOGWO) was first proposed in [100], with the hybridization of the Multi-objective Particle Swarm Optimization (MOPSO) algorithm [101] and the above described GWO. The MOGWO adds to the GWO two components: the non-dominated Pareto sorting stage and a leader selection strategy that assists to choose the GWO hierarchy from the archive. An archive is a storing unit that stores and restores the non-dominated Pareto solution according to the new solutions along the iterations. The archive has a limited number of solutions and the following considerations have to be taken into account [102]:

- If the solution to be stored is dominated by one or more solutions in the archive, it must be eliminated;
- If the new solution dominates one or more members in the archive, the dominated solutions have to be removed and the new non-dominated solution stored;

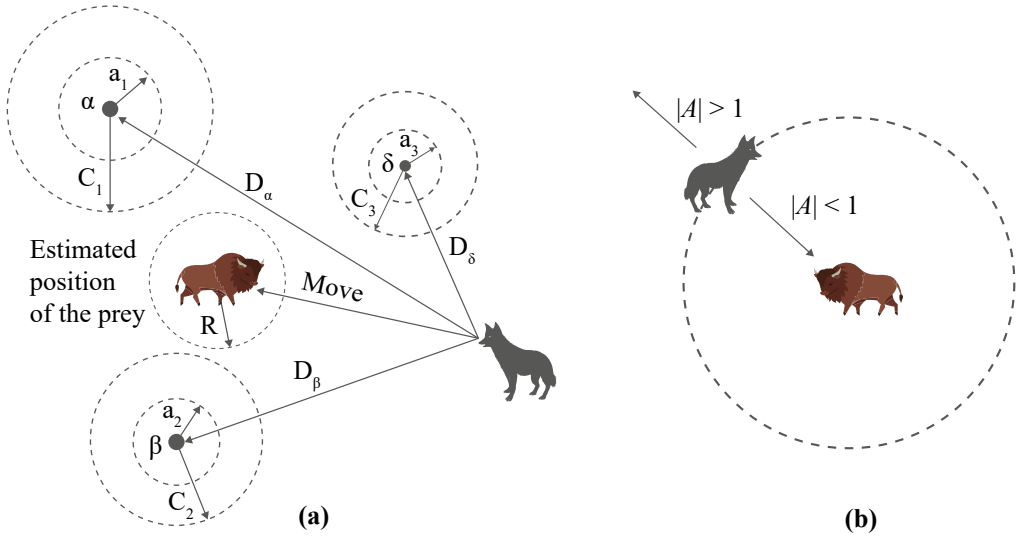

Figure 2.12. Schematic of Grey wolf optimizer. (a) Hunting mechanism of grey wolf optimizer. (b) Exploration of the GWO: for $|A| < 1$ occurs the approaching to the prey (local solution) and for $|A| > 1$ the wolf separates from the current prey in order to find a more suitable prey (global solution).

- If both the new solution and the stored solutions are not dominated by each other, the new solution must be stored; and
- If the archive is full, the grid method reorganizes the section and the most crowded section has the removal of its solutions. For the sake of diversity, the new solution is added to the less crowded segment.

The leader selection is the second new feature of the MOGWO if compared with the GWO. The wolf leaders guide the other wolves along the iterations, and for the single-objective approach, the leaders are defined by the best fitnesses. The multi-objective is comprised of the Pareto optimal principles, which do not consider one solution better than the other if they are not dominated inwardly. In order to select the leaders, the leader mechanism selects the least crowded segments and picks one of the non-dominated solutions. The pseudocode of the MOGWO is given by Algorithm 2.3.

2.4. Machine Learning

The field of machine learning is concerned with the studies and development of algorithms that automatically improve by practice (learning). The following subsections introduce two machine learning techniques: Convolutional Neural Networks (CNN) and Long-short-Term Memory (LSTM).

Algorithm 2.3. Pseudocode of the Multi-Objective Grey Wolf Optimizer (MOGWO)

Input: Population size N_{pop}, `CostFunction`$(\cdot)$, number of iterations $l_{\max}$
Output: Archive

Initialize the grey wolf population X_i $(i = 1, 2, 3, \ldots, N_{\text{pop}})$;
Initialize $\overrightarrow{a}$, $\overrightarrow{A}$, and $\overrightarrow{C}$;
Calculate the objective value for each search agent: `CostFunction`(X_i)
Find the non-dominated solution with (2.44) and (2.45) and initialized the archive with them
$X_\alpha, X_\beta, X_\delta \leftarrow$ `SelectLeader`(Archive)
while $l \leq l_{\max}$ **do**
    For each search agent Update the position of the current search agent by (2.51)-(2.55)
    Update a, A and C
    Calculate the objective value for all search agents
    Find the non-dominated solution
    Update the archive with respect to obtained non-dominated solutions
    if the Archive is full **then**
        Run the grid mechanism to omit one of the current archive members
        Add the new solution to the archive
    end if
    if any of the newly added solutions to the archive is located outside the hypercubes **then**
        Update the grid: to cover the new solution(s)
    end if
    $X_\alpha, X_\beta, X_\delta \leftarrow$ `SelectLeader`(Archive)
    $l \leftarrow l + 1$
end while

2.4.1. Convolutional Neural Networks

The CNN are biologically inspired by the visual cortex of animals and are extensively applied in computer vision, pattern recognition, and natural language processing, among others [103]. Analogous to the Artificial Neural Network (ANN), the CNN is comprised of neurons that self-optimize via supervised learning. The CNN is capable of capturing the spatial and temporal correlations with the reduction of parameters and reusability of weights. Following are detailed the three main layers that constitute a CNN: convolution layer, pooling layer, and fully connected layer.

2.4.1.1. Convolutional layer

The convolutional layers perform the scalar product of the configurable kernel (or filter) matrix and the region connected to the input matrix, and thereafter the output is fed through an activation function to introduce nonlinearity. In this operation, the learnable parameters are the filters that extract the characteristics of the input. Fig. 2.13 illustrates two examples of the convolutional layer: Fig. 2.13a shows a 2D input convolution operation composed of the filter overlaying to the input matrix, element-wise multiplication performed, and the result adding to

the specific position of the output. Fig. 2.13b illustrates a convolutional operation with 3D input data: filter 1 and filter 2 with dimensions $3 \times 3 \times 3$ are parallel convoluted with the input data and their dimensions sum-wise generating two matrices of dimension $4 \times 4 \times 1$, which in the end represent the matrices per depth, therefore the dimension of $4 \times 4 \times 2$. The number of filters in the operation defines the depth of the output.

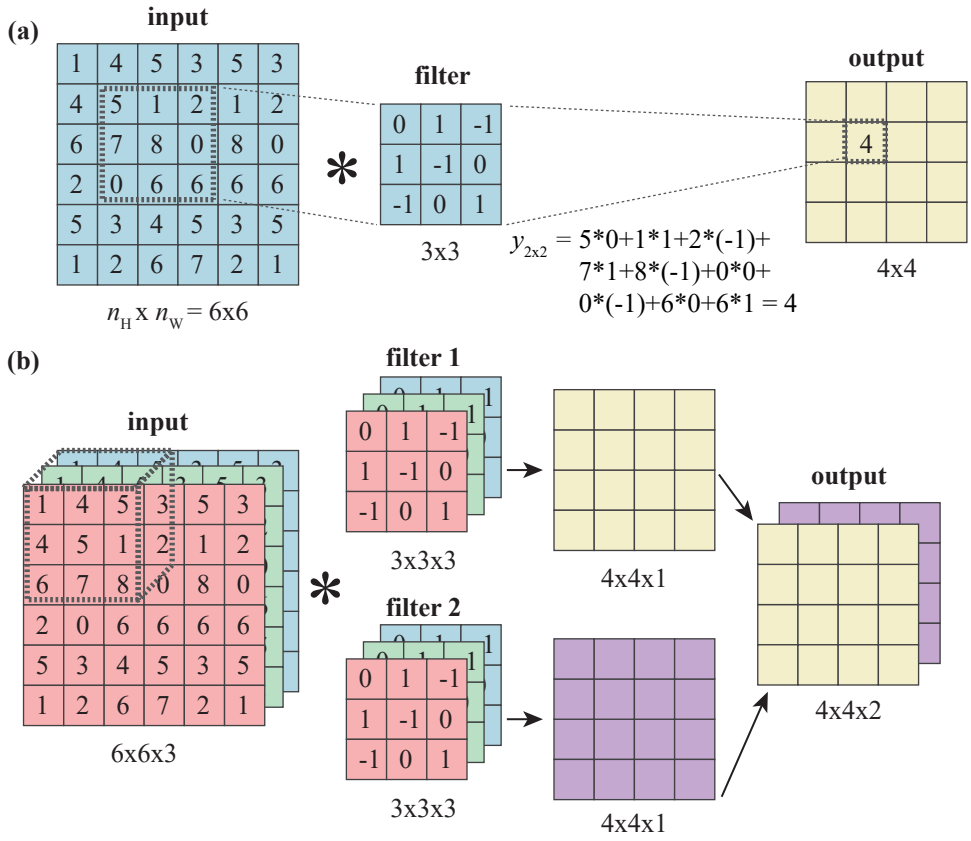

Figure 2.13. Convolutional layer. (a) An example of a 2D convolution operation composed of the filter overlaying to the input matrix, element-wise multiplication performed, and the result adding to the specific position of the output. (b) Example of a convolutional operation for a 3D input and two filters and therefore one output per channel.

The one-dimensional convolutional layer (conv1D) is a special case of the convolutional layers. For this case, a convolution operation is performed between the given input vector and the filter that produces another vector with the number of channels equivalent to the number of filters [104]. CNNs composed by conv1Ds are relatively easy to train and have the least computational complexity if compared with the ones based on higher dimension convolutional layers [105].

At the end of the convolutional layer, it is common to apply an activation function in order to introduce nonlinearity to the network. Three very widely used activation functions are the sigmoid, rectified linear unit (ReLU), and the hyperbolic tangent (*tanh*).

The sigmoid activation function, often known as the logistic activation function, has long been a favorite activation function for neural networks used as the standard activation used on

neural networks up until the early 1990s. The function converts the input into a number between 0 and 1. Values significantly lower than 0 are snapped to 0, and inputs substantially bigger than 1 are changed to the value 1 [106]. The function has an S-shape from zero up through 0.5 to 1.0 for all potential inputs (see Fig. 2.14a). The sigmoid is mathematically expressed as

$$sigmoid(x) = \frac{e^x}{e^x + 1} = \frac{e^x}{e^x + 1}. \tag{2.56}$$

The *tanh* function is another name for the hyperbolic tangent activation function that returns values between -1 and 1 and is expressed as

$$tanh(x) = \frac{e^x - e^{-x}}{e^x + e^{-x}}. \tag{2.57}$$

The output value will be closer to 1.0 the larger the input (more positive), and the output will be closer to -1.0 the smaller the input (more negative) as can be seen in 2.14b.

The rectified linear activation function, mostly known as the short ReLU, is a piecewise linear function that, if the input is positive, produces the input directly; if not, it outputs zero, as illustrated in 2.14c. The vanishing gradient problem restricts the sigmoid and hyperbolic tangent activation functions from being employed in networks with many layers. The rectified linear activation function, however, can deal with this issue and performs quicker and better [107]. The expression that represents the ReLU is

$$ReLU(x) = x^+ = \max(0, x) = \begin{cases} x & \text{if } x > 0 \\ 0 & \text{otherwise} \end{cases} \tag{2.58}$$

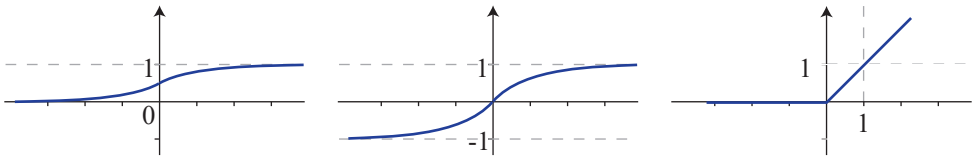

(a) *sigmoid* **(b)** *tanh* **(c)** *ReLU*

Figure 2.14. Convolutional layer activation functions. (a) rectified linear unit and (b) hyperbolic tangent.

2.4.1.2. Pooling layer

The pooling layers have the effect of reducing the dimensions of the hidden layer by merging the outputs of neuron clusters at the preceding layer into a single neuron at the subsequent layer. In other words, the pooling layer is characterized as downsampling along the spatial dimensionality of the input that reduces its size, and consequently, minimizes the number of

parameters and computations in the network [108]. Applying the pooling layer results in smaller feature maps and network parameters.

One of the most used Pooling operators is the Max-Pooling, which, within a set of R activations, transmits the maximum value as output. In this way, it reduces the variability of the convolutional output bands by downsampling [108]. Fig. 2.15 illustrates an example of Max-Pooling in which the Pooling filter has 2×2 dimension and a stride[1] of 2×2 (with non-overlapping sub-regions of the initial representation).

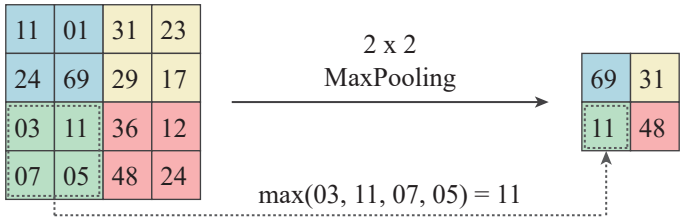

Figure 2.15. Example of a Max-Pooling operation used to reduce the variability of the convolutional output bands.

2.4.1.3. Fully connected layer

The fully connected layer, also referred to as a dense layer, is the layer whose inside neurons link to every neuron of the preceding layer. Generally, the fully connected layer is followed by a nonlinear activation function that attempts to produce the output classes or the regression predictions [107, 109]. Fig. 2.16 shows an example of a fully connected layer comprised of an input layer, two hidden layers, and an output layer.

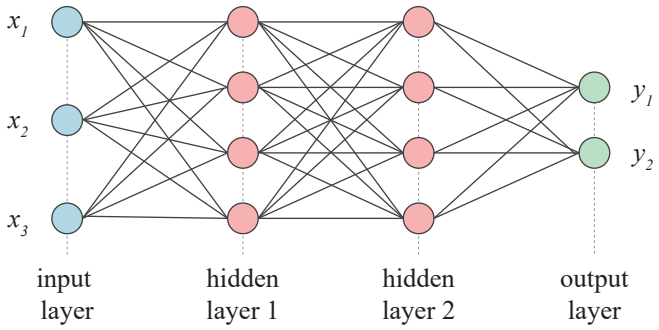

Figure 2.16. Illustration of a fully connected layer.

As stated, the fully connected layers transform linearly the input vector using a weight matrix W. The result is then subjected to a nonlinear transformation using a nonlinear activation function f. This layer simply entails a linear operation on the input vector of the layer, followed by a nonlinear function, which is represented by

[1] Stride is the number of pixels/positions shifted across the input matrix.

$$y_{jk}(x) = f\left(\sum_{i=1}^{n_H} w_{jk}x_i + w_{j0}\right) \tag{2.59}$$

where f is the activation function operation, n_{H} is the number of outputs of the previous layer, y_{jk} is the output of the jth neuron from the kth layer, w is the learned weight, and w_0 is the bias weight. In this operation, the learnable parameters are the weights used to define the output of each layer.

2.4.2. Softmax Function

The softmax function, sometimes referred to as the softargmax function or multi-class logistic regression, converts a vector of K real values into a vector of K real values that add to 1, allowing them to be understood as probabilities. The softmax converts a tiny probability into a small input if it is small or negative, and a high probability into a large input if it is large, but it always stays in the range of 0 and 1. The softmax is a generalization of logistic regression that is only appropriate for use in classifiers when the classes are mutually exclusive and can be used for multi-class classification. The softmax function can be mathematically expressed as [110]

$$\sigma_i(\overrightarrow{z}) = \frac{e^{z_i}}{\sum_{j=1}^{K} e^{z_j}} \tag{2.60}$$

where $\overrightarrow{z}$ is the softmax input vector, z_i is the i-th element of the input vector, and K refers to the number of classes in the classifier.

2.4.3. Cross-entropy

Cross-entropy is a frequently used mathematical function in machine learning, particularly in classification problems. It gauges how far apart two probability distributions are from one another. It is often employed in binary classification to compare the projected probability produced by a machine learning model to the actual true binary labels of the data. The cross-entropy is expressed as:

$$L = -\sum(y \cdot \log(p) + (1-y) \times \log(1-p)), \tag{2.61}$$

where p is the predicted probability of the positive class (between 0 and 1) and y is the true label (0 or 1). The output predicted probabilities are expected to be relatively close to the true labels by the cross-entropy loss function. Important to notice that the cross-entropy loss gets closer to zero when the true class's expected probability is close to 1.

2.4.4. Long Short-Term Memory

Recurrent Neural Networks (RNN) are used for learning whose data characteristics are list or sequential and extensively used for speech recognition, language modeling, and translation. Traditional approaches of RNNs, such as sigma cells or tanh cells, are unable to learn relevant information from the input data when an input gap is large. To overcome this problem, LSTM, a special case of RNN, was proposed in [111] whose objective is to add layers to store long pieces of information in the short-term memory [112]. Indeed, LSTM is capable of learning from long-term dependencies.

The traditional LSTM cell is comprised of three elements: line carriers vector, pointwise operation, and learned weights. Additionally, the LSTM module, proposed in [113], is divided into three parts: (a.1) the forget gate, (a.2) the input gate, and (a.3) the output gate (see Fig. 2.17 (a)).

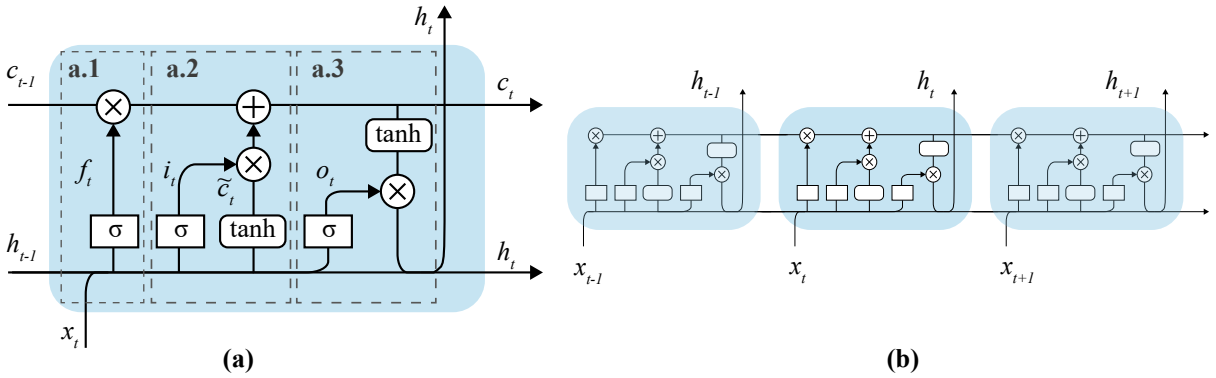

Figure 2.17. LSTM architecture with a forget gate. (a) LSTM cell with emphasis on the gates: (a.1) the forget gate, (a.2) the input gate, and (a.3) the output gate. (b) LSTM network comprised of repeating chain LSTM cells.

The major line carrier vector is called cell state (c), in which the data goes from one cell to another. The cell state is modified by the forget and input gate with some minor linear interactions. Since LSTM cannot remove or add information to the cell state, the flow of information is controlled by the gates. The forget gate is composed of a sigmoid neural network and a multiplication block. The output of the sigmoid layer range from 0 to 1, meaning how much of the information goes through the chain: 0 for discarding and 1 for keeping the data. The input gate decides whether keep the information from the input x_t and recurrent information h_{t-1} vectors. For that, a *tanh* activation function is performed and $\tilde{c}_t$ is a newly generated candidate. Thereafter, the cell state output is updated with the combination of the previous gates. The output gate decides the information to be fed to the neighbor LSTM cells. Also performed by a *tanh* and sigmoid layer, the output of the LSTM cell is the recurrent information h_t and the cell state c_t.

The LSTM architecture with the forget gate can be mathematically modeled by

$$
\begin{aligned}
f_t &= \sigma\left(W_{fh}h_{t-1} + W_{fx}x_t + b_f\right), && (2.62)\\
i_t &= \sigma\left(W_{ih}h_{t-1} + W_{ix}x_t + b_i\right), && (2.63)\\
\tilde{c}_t &= \tanh\left(W_{ch}h_{t-1} + W_{\tilde{c}x}x_t + b_{\bar{c}}\right), && (2.64)\\
c_t &= f_t \cdot c_{t-1} + i_t \cdot \tilde{c}_t, && (2.65)\\
o_t &= \sigma\left(W_{oh}h_{t-1} + W_{ox}x_t + b_o\right), && (2.66)\\
h_t &= o_t \cdot \tanh\left(c_t\right). && (2.67)
\end{aligned}
$$

where σ and *tanh* denote the sigmoid and hyperbolic tangent activation functions, respectively, $W_{fh}, W_{fx}, W_{ih}, W_{ix}, W_{ch}$, and $W_{\tilde{c}x}$ are the weights, b_f, b_i, $b_{\tilde{c}}$, b_o the output, and the operator "$\cdot$" denotes the point-wise multiplication of two vectors.

A recurrent neural network is composed of multiple copies of the same neural cell, with the transmitting message to each other (see Fig. 2.17 (b)).

CHAPTER 3.

Increasing the Power and Spectral Efficiencies in Conventional and Constant-Envelope OFDM-based VLC SISO Systems through Multi-Objective Optimizations

3.1. Introduction

The PAPR of modulating signals is an important issue to be considered in LED-based VLC systems. Different techniques were developed to reduce the PAPR and, accordingly, mitigate nonlinearity and increase the average transmitted power [18–20]. However, the PAPR reduction achieved in [18] and [19] are relatively small, and the complexity required by the transceiver suggested in [20] is higher if compared to conventional OFDM-based VLC systems. The transmission of CE-OFDM based on electrical phase modulation was shown to improve the tolerance to noise and the nonlinearities in optical communications [21–23]. In VLC systems, these benefits allow the application of larger signal amplitudes despite the LED nonlinearities and, thus, increasing the reach in such links [24, 25].

The OFDM IMD decreases the performance of the system and enforces higher optical guard-bands (G_{B}), consequently reducing the SE, as described in [26]. These trade-offs suggest the application of optimization algorithms that consider the bandwidth (B_{W}) of the signal and carrier frequency, along with the size of the guard-interval (G_{I}), applied to exclude the inter-symbol interference [23, 27]. This is a particular issue in VLC systems based on CE-OFDM because of the spectral broadening that characterizes such low PAPR signals.

This chapter investigates the trade-off between the maximization of the optical power and the LED's nonlinearity. With the aim of increasing the VLC link distances, the system parameters optimization was evaluated, taking into account the bias current (I_{bias}), the OMI, the G_{B}, G_{I}, and the oversampling factor N_{samp}.

Therefore, the novel technical contribution in this chapter lies in the application of the above-mentioned multi-objective optimization in VLC systems based on CE-OFDM modulating signals. In particular, it is demonstrated that the systems with such low PAPR signals outperform

the VLC systems based on conventional OFDM. Results show that the optimization procedure benefited the SE of both evaluated systems, according to the reduction in the G_{B} to only $6\ \%$ of the signal bandwidth. With this guard band, a Bit Error Rate (BER) equals to 1×10^{-3} was achieved with CE using SNR values of ≈ 10.8 and ≈ 24 dB, for 4-QAM and 16-QAM subcarrier mappings, respectively. For the conventional OFDM-based VLC systems, this performance was reached with SNR values of approximately 13 and 25 dB, for 4-QAM and 16-QAM, respectively.

This chapter is structured as follows. The multi-objective problem formulation and the employed NSGA-II algorithm are presented in Section 3.2. The evaluation of the proposed optimization and the obtained simulation results are shown and discussed in Section 3.3. Section 3.4 outlines the findings.

3.2. Guard-band Reduction and Power Efficiency Enhancement of VLC Systems Through Multiobjective Optimization

This section is devoted to the description of the problem formulation as a Multi-Objective Optimization (MOO) approach and the environmental parameters used in this work.

3.2.1. MOO Problem Formulation

The OFDM signal can be transmitted or up-converted and centered around a carrier frequency f_{c} with amplitude analog modulations. According to the f_{c} and B_{W}, the guard-band G_{B} can be determined as the band between the DC and the lower OFDM frequencies. Fig. 3.1 depicts the normalized power spectral density (PSD) of a pass-band OFDM signal with the relation between the guard-band G_{B} and the signal bandwidth $\frac{G_{\mathrm{B}}}{B_{\mathrm{W}}}$ being unitary. The spectral efficiency is defined as $\mathrm{SE} = R_{\mathrm{b}}/(G_{\mathrm{B}} + B_{\mathrm{W}})$, for R_{b} the system data rate in bits/s. The total bandwidth required by the IMDD optical system comprises the effective bandwidth B_{W} and the guard-band G_{B} [31]. As observed in [31] and [114], in order to avoid intermodulation distortions introduced by the photodetection in IMDD systems, the guard band should be at least equal to the signal bandwidth. Thus, for a certain R_{b} and $G_{\mathrm{B}} = B_{\mathrm{W}}$, the spectral efficiency becomes $\mathrm{SE} = R_{\mathrm{b}}/(2 \times B_{\mathrm{W}})$. Therefore, reductions in G_{B}, i.e., by tolerating some signal deterioration through IMD, the guard band can be reduced and SE increased accordingly, one of the main objectives of the optimization procedures proposed in this work.

Identifying the rules of the evaluated optimization is the primary goal of the problem formulation. In summary, the objectives are to minimize the required SNR for a bit error rate BER = 1×10^{-3} and to maximize the overall SE by minimizing the optical guard band, which indicates that this is a multi-objective problem.

Hereafter, it is utilized the definition of required SNR as $\mathrm{SNR}_{\mathrm{req}} = \mathrm{SNR\ at\ BER} = 10^{-3}$.

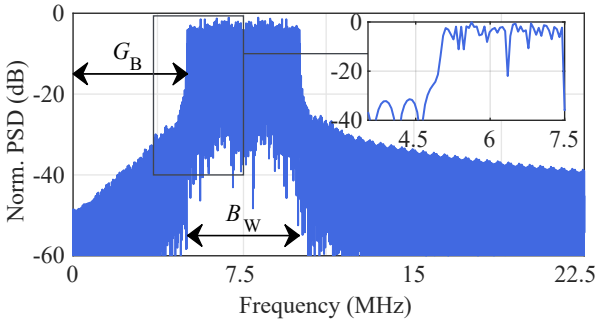

Figure 3.1. Normalized power spectral density (PSD) of an OFDM signal generated with a $G_B/B_W = 1$ (G_B - guard-band, B_W - bandwidth). Inset is the spectrum of an OFDM symbol with emphasis on the first subcarriers.

To increase the transmitted optical power, the bias current and OMI limits were chosen to stimulate the LED operation in the nonlinear region (see Fig. 2.3). The guard-interval G_I size is the number of redundant signal samples added to avoid interference of multipath from previous transmissions, and N_{samp} is the oversampling factor. In summary, the problem formulation is restricted by the specified boundaries, subject to the described variables to be optimized, and subject to the BER constraint of inequality, as shown in Table 3.1. The bias current boundaries were empirically determined in order to establish the link (BER $<<$ 10^{-3} for 100 cm of link distance), without a high noise effect (lower bound) and without damaging the component (upper bound).

The guard-interval G_I size is the number of redundant signal samples appended at the beginning of the OFDM symbol and N_{samp} is the oversampling factor in the up-conversion process. In summary, the problem formulation is subject to the described variables to be optimized, bounded by the stipulated limits, and the BER constraint of inequality (Table 3.1).

Table 3.1. The problem formulation.

Min. SNR at BER $= 1 \times 10^{-3}$
Min. $\frac{G_B}{B_W}$
subject to
$0.1 \leq \text{OMI} \leq 1$
$400 \leq I_{bias} \leq 2000$ mA
$0.01 \times B_W \leq G_B \leq B_W$
$\left(2^{X_{max}}\right)^{-1} \leq G_I = \left(2^{X}\right)^{-1} \leq \left(2^{X_{min}}\right)^{-1}$
$4 \leq N_{samp} \leq 10$
$X_{max} = 10$ and $X_{min} = 2$

According to the formulation problem constraints, the solution vector $\overrightarrow{s} \in \mathbb{R}$ is defined as

$$\overrightarrow{s} = [\text{OMI } I_{bias} \; G_B \; G_I \; N_{samp}]. \tag{3.1}$$

In the CE-OFDM evaluation, the optimization was carried out using the determined problem formulation taking a wide range of $2\pi h$ into consideration.

3.2.2. Environmental Configuration

The electrical-optical (EO) characteristic curve of the white LEDs, hereafter applied, is shown in Fig. 3.2. This nonlinear EO curve was obtained by the lux meter Instrutherm THDL-400 with the variation of the bias current (Fig. 3.2a). For the characterized LumiLED white-light LED LXML-PWC2 source [115], the parameters of the nonlinear EO curve determined by Eq. (2.1) are $L_{\max}$ = 755 lux, $\zeta = 20$, and k = 1.9. By calculating the linear range via the 1-dB compression method, according to [116], the linear range's upper bound is around 1000 mA.

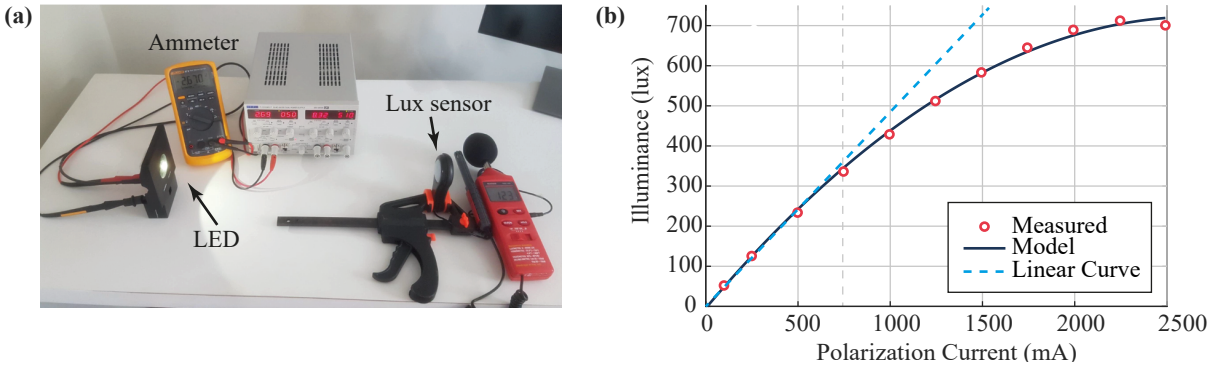

Figure 3.2. Determination of the LED electrical-optical conversion characteristic curve [3]. (a) Setup with a white LED, an ammeter, and a lux meter Instrutherm THDL-400. (b) Measured and fitted characteristic current-lux curve of the LumiLED white-light LED LXML-PWC2.

In order to analyze the performance of the proposed optimization procedure, Monte Carlo simulations were conducted by using a VLC-SISO model, as a cost function, based on a real system's characteristics (see Fig. 3.2). The parameters of the VLC system model can be seen in Table 3.2.

The performance of pass-band multicarrier modulations that take into account the Hermitian symmetry is assessed in the current study, in contrast to the method used in [3]. Nonetheless, the results from the refereed paper were also examined.

In the conducted algorithms, the OFDM bandwidth was fixed to 10 MHz and the FFT block had a size of 512, from which 256 carried data and the other half was filled by Hermitian symmetry samples. In order to diminish the effect of the filtering, 40 subcarriers were zeroed. The utilized modulation orders M were 4 and 16-QAM. The thermal noise is assumed to be dominant and it was modeled as an additive white Gaussian noise (AWGN). The OFDM bit rate is determined by

$$R_{\mathrm{b}} = \frac{N_{\mathrm{s}} \times \log_2(M) \times B_{\mathrm{W}}}{N_{\mathrm{FFT}} + N_{\mathrm{CP}}} \tag{3.2}$$

Table 3.2. Parameters of the SISO-VLC model.

	Parameter	Value
Room	Room size	3 m × 3 m × 3 m
	Link length	2 m
Emitter	Emitter height	1 m
	Orientation vector	[1, 0, 0]
	Semi-angle at half power	30°
	Tx Frontend bandwidth	25 MHz
Receiver	Receiver height	1 m
	Orientation vector	[-1, 0, 0]
	Photosensitive area	7 mm^2
	Field of view	45°
	Responsitivity	0.63 A/W
	Rx Frontend bandwidth	25 MHz
	Gain of optical filter	1

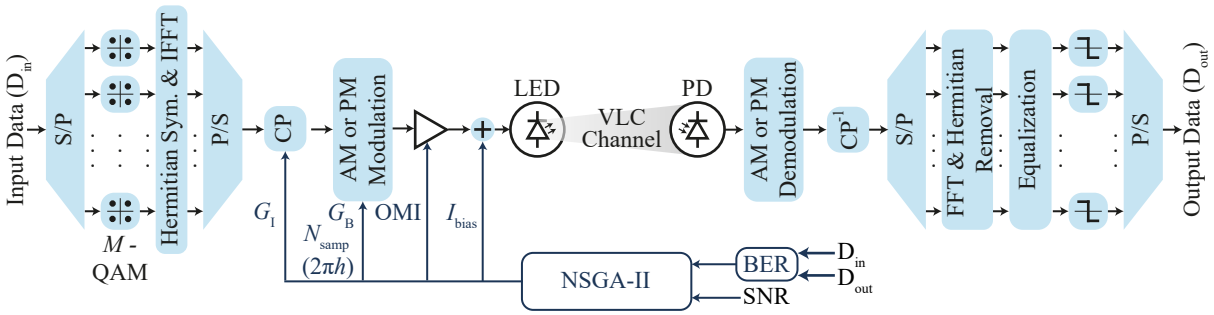

Figure 3.3. Block diagram of CE-OFDM and OFDM-based VLC system parameters optimization by NSGA-II.

where N_s is the number of data subcarriers calculated as $N_s = N_{FFT} - N_z$, where N_z is number of zeroed subcarriers and N_{CP} is the number of the cyclic prefix samples.

The OFDM parameters are summarized in Table 3.3.

As detailed in the problem formulation (Subsection 3.2.1), the BER is used as an inequality constraint for the optimization process. This metric is determined by counting the bit errors over the 342,400 transmitted and received bits. The solutions are also evaluated and compared in terms of error-vector magnitude (EVM), calculated as described in [117] and [79]. The real-coded NSGA-II algorithm is developed as stated in [2]. The individuals of the first population are determined randomly by a uniform distribution limited according to the variables' range (see Table 3.1).

The parameters of the NSGA-II are strictly related to the problem. The population size was determined by considering how long it will take to evaluate each iteration. If this size was too

Table 3.3. OFDM parameters and values.

Parameter	Variable	OFDM
Effective bandwidth	B_{W}	10 MHz
(I)FFT size	N_{FFT}	512
Subcarrier spacing	Δ_{f}	19.531 kHz
Zeroed subcarriers	N_{z}	40
Subcarrier mapping	M	4-QAM and 16-QAM
Maximum bit rates	$R_{\mathrm{b-max}}$	4.180 and 8.360 Mbps

large, processing time increased significantly. Otherwise, if the maximum population size was too low, the population's diversity suffered and the time of convergence was also affected. For each individual, the probability of mutation is determined by the mutation rate. Setting the mutation rate too low can restrict the diversity and impede the search process while setting it too high can result in excessive exploration and the loss of good solutions. Setting the crossover rate too high may result in early convergence, while setting it too low may slow down the exploration of the search space. A summary of the empirically set NSGA-II parameters is detailed in Table 3.4. The overall optimization procedure is illustrated in Fig. 3.3.

Table 3.4. NSGA-II optimization parameters.

NSGA-II Parameter	Value
Population size	20
Mutation rate	0.02
Crossover rate	0.5
Selection method	Tournament
Number of iterations	50

For the CE-OFDM signals, the optimizations were evaluated separately for different values of $2\pi h$, and the first Pareto front was taken as a solution. Then, a new set of solutions were generated considering the non-dominated solutions among all the phase modulation indexes solutions.

3.3. Results and Discussion

Following are the results of the optimization procedure based on the OFDM-based VLC Systems without Hermitian symmetry, reported in [3] (Subsection 3.3.1), and with Hermitian symmetry (Subsection 3.3.2).

3.3.1. Performance Evaluations of the OFDM-based VLC Systems (without Hermitian Symmetry)

The Pareto fronts for 4-QAM and 16-QAM of the traditional OFDM are given in Fig. 3.4 for the problem formulation described in Subsection 3.2.1 after the algorithms have been evaluated. The transmitted power required for the BER $\approx 1 \times 10^{-3}$, i.e., the SNR for a fixed noise power level, decreases with the increase of the guard band. This is due to the IMD in the photodetection [26]. This effect is noticeable for $G_{\mathrm{B}}/B_{\mathrm{W}} \leq 0.05$, for 4-QAM. The variation of the required SNR for 16-QAM at a BER $\approx 1 \times 10^{-3}$ ranges from 15.5 (at $G_{\mathrm{B}}/B_{\mathrm{W}} = 0.01$) to 18 dB (at $G_{\mathrm{B}}/B_{\mathrm{W}} = 0.875$).

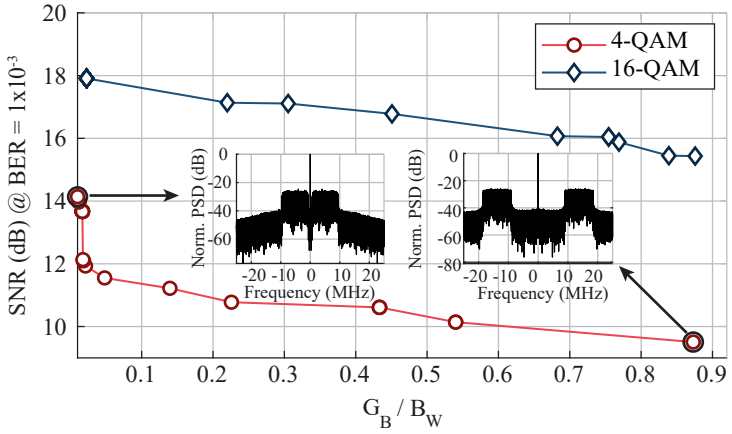

Figure 3.4. Pareto fronts for a SNR at BER $= 1 \times 10^{-3}$ *versus* $G_{\mathrm{B}}/B_{\mathrm{W}}$ for 4-QAM and 16-QAM [3]. Inset is shown the normalized power spectral density (PSD) for the optimized 4-QAM extreme solutions.

Some of the optimized solutions obtained via a simulated model are detailed in Table 3.5. With the optimization, the signals tend to be centered at ≈ 1 A, which configures the nonlinear region of the characteristic curve of the LED.

With the aim of analyzing the sensibility of the optimized solutions according to the bias current, the solutions for the third lines of Table 3.5 for 4 and 16-QAM were taken as reference, keeping the same optimized values and varying the bias current from 400 to 2000 mA. The difference between the $\mathrm{SNR}_{\mathrm{req}}$ obtained by the optimization (see the formulation problem in Table 3.1) and the one evaluated for different biases (performed for a BER $= 10^{-3}$) is hereafter called $\mathrm{SNR}_{\mathrm{req}}$ penalty. The results for the SNR penalty are shown in Fig. 3.5. The nonlinearity of the LED plays an important role in this analysis: the $\mathrm{SNR}_{\mathrm{req}}$ penalty values tend to increase in this region, while for the linear region (up to 1000 mA), the penalties are not substantial.

Table 3.5. Optimized parameters for some points of the Pareto fronts [3].

4-QAM						
OMI	I_{bias} (A)	G_{I}	N_{samp}	$G_{\text{B}}/B_{\text{W}}$	SNR (dB)	EVM (dB)
0.924	0.9994	$1/8$	5	0.0101	13.8	-9.89
0.931	1.0011	$1/4$	6	0.0177	11.8	-9.4
0.945	0.9996	$1/8$	6	0.0481	11.5	-9.33
1	1.0016	$1/8$	7	0.226	10.9	-9.32
16-QAM						
OMI	I_{bias} (A)	G_{I}	N_{samp}	$G_{\text{B}}/B_{\text{W}}$	SNR (dB)	EVM (dB)
0.995	1.0012	$1/8$	6	0.0228	18.2	-15
0.995	1.0013	$1/8$	7	0.305	17.3	-14.9
0.989	1.0009	$1/16$	9	0.683	16.9	-15.2
0.998	1.0022	$1/16$	9	0.769	16.9	-15.1

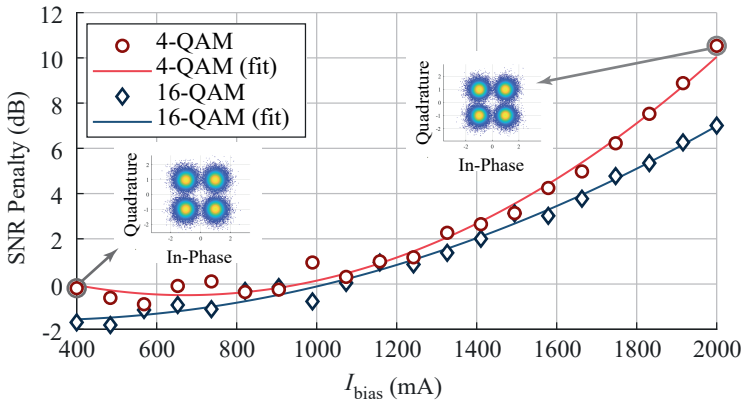

Figure 3.5. SNR penalties *versus* bias current [3]. Inset the scatterplots are shown for $I_{\text{bias}} = 400$ and 1200 mA.

3.3.2. Performance Comparisons between Conventional OFDM and Constant Envelope OFDM-based VLC Systems (with Hermitian Symmetry)

Before the performance comparisons, the suitability of the proposed optimization procedure was evaluated for the CE-OFDM-based systems, considering a wide range of the phase modulation index $2\pi h$. Fig. 3.6 and Fig. 3.7 show the Pareto fronts obtained with 4-QAM and 16-QAM as subcarrier mappings, respectively. Then, among all Pareto front solutions generated for each phase modulation index, the non-dominating individuals (F_1) are chosen to compose the optimum Pareto front for each subcarrier mapping.

It can be observed from Figs. 3.6 and 3.7 that, as expected, the reduction in the G_{B} requires high values of SNR_{req}. With 4-QAM as subcarrier modulation, values of $2\pi h$ around 11.75 provide good solutions, against $2\pi h \approx 6$ when 16-QAM is used as subcarrier mapping.

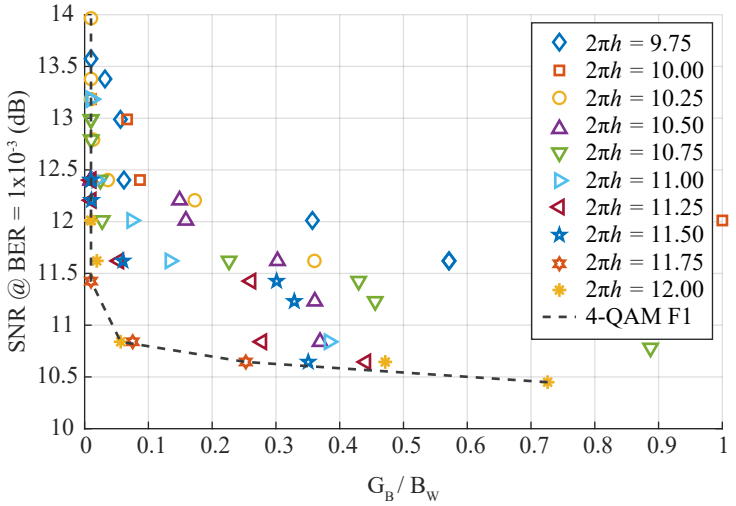

Figure 3.6. Pareto fronts (SNR @ BER $= 1 \times 10^{-3}$ *versus* $G_{\mathrm{B}}/B_{\mathrm{W}}$) of CE-OFDM with 4-QAM mapping.

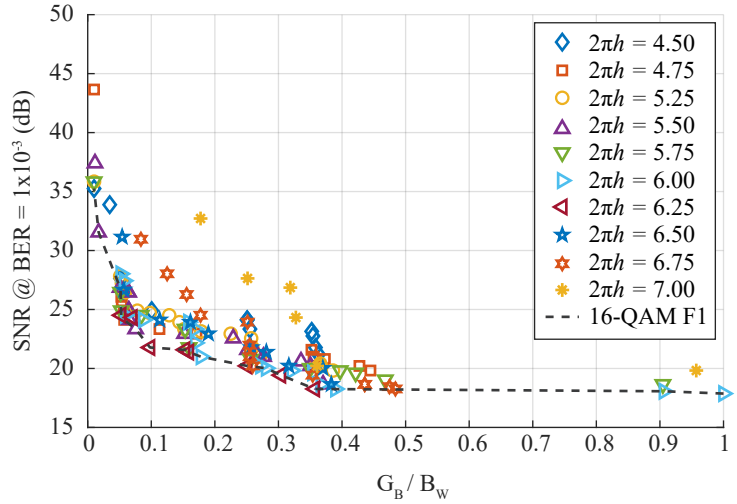

Figure 3.7. Pareto's fronts (SNR @ BER $= 1 \times 10^{-3}$ *versus* $G_{\mathrm{B}}/B_{\mathrm{W}}$) of CE-OFDM with 16-QAM mapping.

Fig. 3.8 shows the Pareto fronts in which the performance of both evaluated VLC systems was compared, considering the two evaluated modulation orders. Fig. 3.8 shows that, when 4-QAM is used as subcarrier mapping, the system with CE signals outperforms the conventional OFDM-based systems, except when a $G_{\mathrm{B}}/B_{\mathrm{W}} = 1$ % in which both systems have the same performance. At $G_{\mathrm{B}}/B_{\mathrm{W}} = 6$ %, the adoption of constant envelope signals provided an SNR gain of around 2.2 dB. When 16-QAM is the subcarrier modulation, the performances of OFDM and CE-OFDM systems are almost the same with the same guard band. Nonetheless, the performance gain of the system with CE signals increases with G_{B}, proving the power efficiency provided by the adoption of such PAPR transformation technique. Tables 3.6 and 3.7 show the optimized parameters, as well as the system performances of both systems in terms of SNR required for the BER $= 1 \times 10^{-3}$.

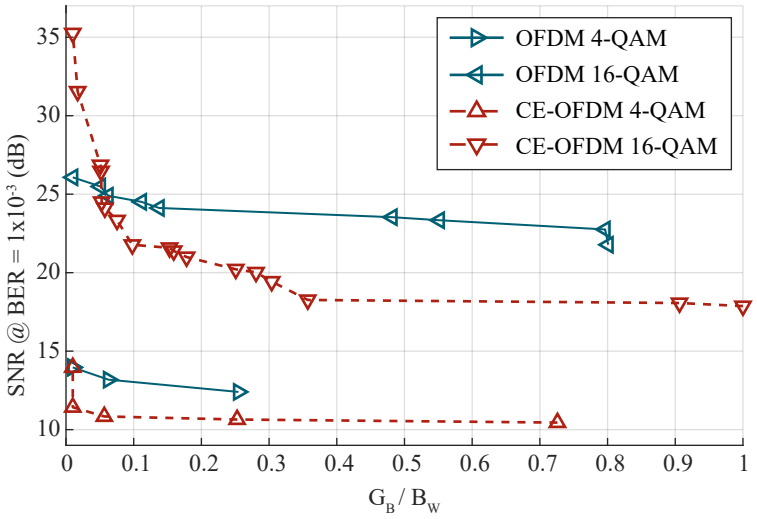

Figure 3.8. Performance comparison of CE-OFDM and the conventional OFDM-based VLC systems, in terms of Pareto fronts (SNR @ BER $= 1 \times 10^{-3}$ *versus* $G_{\mathrm{B}}/B_{\mathrm{W}}$), for both 4-QAM and 16-QAM mappings.

3.4. Final Remarks

Visible light communication (VLC) is a potential complementary technology for radio-frequency wireless systems considering its low-cost energy consumption, availability, and unlicensed spectrum. Nonetheless, the light-emitting diode (LED) adds nonlinearity to the modulating optical signal to be conveyed. In this chapter, a multi-optimization problem to exploit the LED nonlinear operation region was presented, with the objectives of minimizing the required signal-to-noise ratio (SNR) for a bit error rate BER = 1×10^{-3} ($\mathrm{SNR}_{\mathrm{req}}$) and maximizing the overall SE by minimizing the optical guard-band, with and without a constant envelope (CE). In order to achieve the described objectives, the OFDM-based VLC system parameters, such as bias-current, optical modulation index, guard-interval, guard-band, and phase modulation index, were optimized via the non-sorting genetic algorithm (NSGA-II).

Results show that the required SNR decreases with the increasing guard band due to inter-modulation distortions. For CE-OFDM signals, a guard-band of $6\ \%$ of the signal bandwidth was obtained for $\mathrm{SNR}_{\mathrm{req}}$ values of ≈ 10.8 and ≈ 24 dB, for 4-QAM and 16-QAM, respectively, against the $\mathrm{SNR}_{\mathrm{req}}$ values of $\approx\ 13$ and $\approx\ 25$ dB achieved by the conventional OFDM-based systems. The SNR gains obtained with CE-OFDM and 16-QAM increased with the adoption of higher guard bands, suggesting that the CE-OFDM modulation format and parameters optimization via algorithms are promising in power and spectral-efficient VLC systems.

Table 3.6. OFDM optimized parameters for the Pareto front set of solutions.

4-QAM					
OMI	I_{bias} (A)	G_{I}	N_{samp}	$G_{\text{B}}/B_{\text{W}}$	SNR_{req} (dB)
0.960	0.659	10	10	0.01	13.965
1	0.366	10	10	0.01	13.965
0.986	0.702	8	10	0.254	12.402
0.999	0.472	8	10	0.062	13.184
16-QAM					
OMI	I_{bias} (A)	G_{I}	N_{samp}	$G_{\text{B}}/B_{\text{W}}$	SNR_{req} (dB)
0.870	0.124	9	10	0.801	21.777
0.905	0.980	7	10	0.010	26.074
0.971	0.767	6	10	0.482	23.535
0.894	0.984	8	10	0.138	24.121
1	0.447	6	10	0.796	22.754
0.911	0.640	6	10	0.552	23.34
0.877	0.957	5	10	0.051	25.488
0.966	1.093	8	10	0.062	24.902
0.904	1.058	7	10	0.111	24.512

Table 3.7. CE-OFDM optimized parameters for the Pareto front set of solutions.

4-QAM						
OMI	I_{bias} (A)	G_{I}	N_{samp}	$G_{\text{B}}/B_{\text{W}}$	SNR_{req} (dB)	$2\pi h$
0.973	0.171	5	10	0.726	10.449	12
0.924	0.650	7	10	0.253	10.645	11.75
1	0.882	6	10	0.057	10.84	12
1	0.939	9	10	0.010	11.426	11.75
0.703	0.634	6	9	0.010	13.965	10.25
16-QAM						
OMI	I_{bias} (A)	G_{I}	N_{samp}	$G_{\text{B}}/B_{\text{W}}$	SNR_{req} (dB)	$2\pi h$
0.937	0.01	10	10	1	18	6
0.937	0.206	8	10	0.906	18	6
1	1.049	7	10	0.357	18	6.25
0.764	1.093	10	10	0.304	19	6.25
0.845	1.067	7	9	0.281	20	6
0.852	1.081	10	10	0.251	20	6.25
0.678	1.084	5	9	0.178	21	6
0.691	0.972	10	10	0.159	21	6.25
0.905	1.01	8	9	0.153	22	6.25
0.632	1.093	9	10	0.098	22	6.25
0.779	1.014	8	9	0.075	23	5.5
0.977	1.178	9	9	0.057	24	4.75
0.636	1.048	10	10	0.053	25	6.25
0.526	1.105	7	7	0.052	26	5.75
0.528	1.247	7	7	0.051	27	5.5
0.484	1.125	6	6	0.017	32	5.5
0.416	1.159	8	7	0.010	35	4.5

CHAPTER 4.

Toward AI-enhanced VLC Systems for Industrial Applications

4.1. Introduction

This chapter presents the application of meta-heuristic algorithms to enhance power and spectral efficiency for a moving VLC receptor. Additionally, this chapter proposes the use of LSTM to predict the position of VLC terminals for the optimization of link parameters. Based on a novel forecasting methodology, a new problem formulation is proposed and applied in the optimization procedure which is called hybrid multi-objective optimization (HMO). Two Industry 4.0-oriented case studies (1D and 2D traces) are considered, leading to two-stage evaluations. The LSTM architecture is applied to predict the channel gain of trajectory positions and, thereafter, configure the VLC links with the optimal PHY layer parameters obtained by the HMO.

The adoption of long short-term memory (LSTM), an artificial neural network capable to learn features from sequential data, aiming at trajectory prediction is of primary interest. The proposed LSTM extracts a set of parameters for the VLC system, previously obtained through optimization algorithms, which is not considered in the works described in [39] and [40]. LSTM is a promising tool, considering that one of the major issues addressed in this paper is a time series prediction [118]. LSTM has proven to be efficient to predict a series of human trajectories considering its behaviors and interaction with surrounding environments [119]. In [120] a link outage predictor in OWC systems based on LSTM was reported. With their predictor, the authors achieved 91% of event hit rate for the outage and 83% for predicting signal recoveries in the uplink and downlink of line-of-sight (LOS) OWC links. However, they do not consider movement trajectories in their proposed framework.

The remainder of this chapter is structured as follows. Section 4.2 describes the case studies scenarios implemented in this work. Optimization procedures, applied criteria, and meta-heuristics are presented in Section 4.3. Section 4.4 is devoted to the presentation of the LSTM architectures and procedures to generate the datasets. In Section 4.5, the obtained simulation and experimental results are shown and discussed. Ultimately, Section 4.6 summarizes the findings of this chapter.

4.2. Case Study Scenarios

The scenarios for Case Studies I and II are described in this section.

4.2.1. Case Study I - Experimental Validation of channel model by 1D Traces

Experiments were conducted in a SISO model with the LED input current in the linear optic-electrical conversion region (see Fig. 3.2 (b)), in order to establish a simulation model of the setup, which was denominated Digital Twin (DT). Apart from serving as a calibration for the DT, the 1D setup also corresponds to the use case scenario in which robots work in one direction of movement, as shown in Fig. 4.1. In this use case, there is no angle dependency and the performance of the VLC link depends only on the link distance.

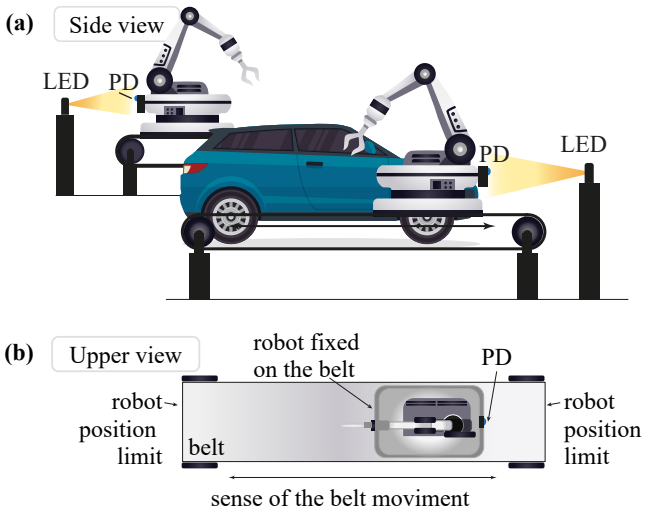

Figure 4.1. Industrial scenario with two robots communicating via Li-Fi moving on a belt in one direction of movement. Side view (a) and upper view (b) of the proposed use case.

Fig. 4.2 depicts the experimental setup used to evaluate the VLC link performance obtained by varying the transmission distance. An arbitrary function generator (AFG) delivered the electrical signals. The generation of the $s(t)$ electrical signals (optical modulating signals) took as reference some recommendations for the 5G New Radio (NR) physical layer, aiming at scenarios in which OWC employs modern wireless analog signal formats [121]. Considering the bandwidth limitation provided by the experimental setup, the 5G NR OFDM signals were generated with bandwidths $B_{\mathrm{W}} = 5$ MHz and subcarrier spacing $\Delta_{\mathrm{f}} = 15$ kHz, resulting in the multiplexing of the reasonable amount of data subcarrier shown in Table 4.1.

Considering the above-mentioned 5G NR specifications, the analog signals were centered at the carrier frequency $f_{\mathrm{c}} = 7.5$ MHz. These signals were electrically amplified to set OMI $= 0.35$ and superimposed onto a bias current $I_{\mathrm{bias}} = 500$ mA via a Bias-Tee to drive a commercial LumiLED white-light LED LXML-PWC2 [115]. After propagation through the LOS channel, supported by PHYWE 09820-02 bi-convex lenses with 100 mm of focal length and

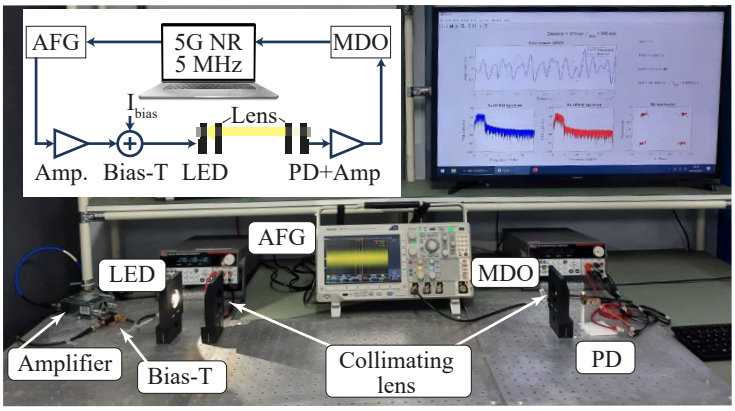

Figure 4.2. Experimental setup used to establish the logical copy of the physical object, as demanded in the Digital Twin denomination. Inset shows the setup block diagram.

Table 4.1. Experimental Parameters.

	Parameter	Symb.	Value
OFDM parameters	QAM mapping order	M	4
	FFT block size	N_{FFT}	128
	Data subcarriers	N_{s}	42
	Cyclic prefix size	N_{CP}	16
	Subcarrier spacing	Δ_{f}	15 kHz
	Bandwidth	B_{W}	5 MHz
	Carrier frequency	f_{c}	7.5 MHz
VLC parameters	Offset (bias) current	I_{bias}	500 mA
	Optical modulation index	OMI	0.35

40 mm of diameter, the VLC signals were detected by a HAMAMATSU S10784 photodiode before analog-to-digital conversion by a mixed domain oscilloscope (MDO) and demodulated offline. The OFDM signals are composed of $N_{\mathrm{s}} = 42$ data subcarriers and the size of the fast Fourier transform is $N_{\mathrm{FFT}} = 128$, due to hardware limitations of the experimental setup. The parameters used in the experimental evaluation are summarized in Table 4.1.

Fig. 4.3 shows the performance comparisons between the experimental and the simulation results for various link lengths, using error vector magnitude (EVM) as the performance metric. During the experiments, the distance link was increased from 80 to 400 cm. The maximum distance obtained was 4 m due to lab space restrictions. To obtain a noise level similar to the physical setup, the simulation model was calibrated. To this aim, the receiver noise level in the simulated system was varied. The root mean square of the error over the measured points (RMSE) was evaluated between the EVMs of both physical setup and simulation to identify a noise power that makes the EVM curves match (minimize the RMSE value), which hereafter is called calibrated electrical receiver noise level. After sweeping the PD noise level in the model, the RMSE was calculated between the EVM performances of the simulated and physical setup.

The minimum RMSE of 2.60 % was between the EVMs across all distances for a noise level of $\nu = -165$ dBm. Being this noise level the one that best matches the performances, then the noise level was set as the Digital Twin parameter value (see Fig. 4.3). Henceforth in this chapter, the experimental EVM values of Fig. 4.3 will be referred to as "reference EVM values (EVM_{ref})". The slight experimental performance degradation registered at 220 cm is due to a minor lens misalignment that occurred during the variation of the transmission distance.

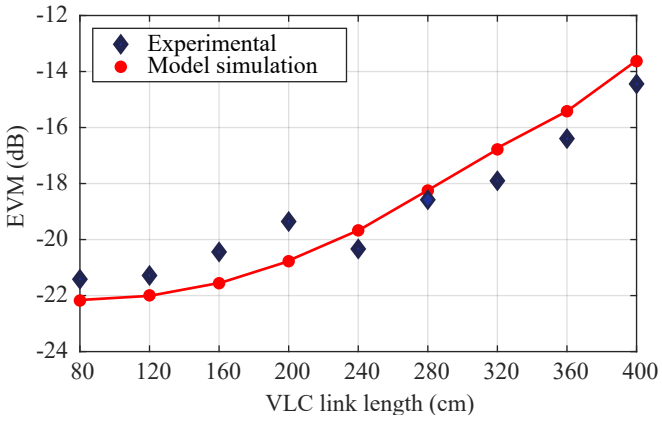

Figure 4.3. EVM *versus* link length for evaluated experiments and the calibrated Digital Twin. The similarity of both EVM series is measured with RMSE of 6 %, which validates the developed model (Digital Twin).

In the modeled VLC model, the intense ambient light reaching the photodiode induces a steady state shot noise, treated as additive white Gaussian noise (AWGN) with zero mean and variance $\sigma^2 = N_0/2$, in which N_0 is the noise power [46, 47, 57]. It is also assumed that the impact of the OFDM Gaussian-distributed amplitudes (modulating signals) on the shot noise is negligible. Fig. 4.4 show a schematic of the VLC simulation model. In order to apply the bias current accordingly, an offset removal is evaluated in the OFDM modulating signals before the re-scaling processing with the α parameter. If a manufacturing hall with high ceilings is taken as an example, the multipath can be ignored and the transmission can be approximated to a free space optical system. Additionally, the reflections along the path can be compensated by the one-tap post equalizer implemented in the OFDM and thus be neglected in the noise.

The analog optical frontends (OFEs) are modeled as band-pass Butterworth filters based on measurements described in [122]. For both transmitter and receiver, the band-pass gain was set to 0 dB, the cut-off frequencies for the high-pass components were 90 kHz (order 4)

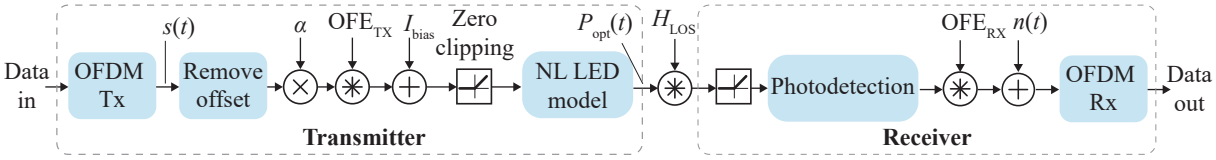

Figure 4.4. Block diagram of the VLC model. The symbol "⊛" denotes the convolution operator. OFE_{Tx}: analog optical front end at the transmitter; OFE_{Rx}: analog optical front end at the receiver; NL: nonlinear.

and 200 kHz (order 1), and the cut-off frequencies for the low-pass components were left at 20 MHz (order 1), 100 MHz (order 4), and 200 MHz (order 8).

4.2.2. Case Study II - Modelling 2D Trajectories

To simulate a more complex movement of a mobile robot, a 3-dimensional (3D) room model was generated and taken as a reference including a mobile robot equipped with an OWC receiver (Rx) moving under a single ceiling-mounted transmitter (Tx) along a looping trajectory. This model is depicted in Fig. 4.5a. In the first stage, a 2D trajectory was considered, represented by a series of 100 positions that the robot will follow. At every position, the channel gain of the line-of-sight channel between the transmitter and receiver is calculated according to (2.5). The geometrical radiation characteristics of the optical source are modeled by a polynomial fit based on the specifications of the commercially available LED. Similarly, the directivity of the receiver is modeled according to a commercial photodetector. The terms depending on the angle of incidence are summarized into a single polynomial fit for this purpose. The geometrical radiation and sensitivity characteristics, i.e., their angular dependencies, are depicted by colored mesh cones (transmitter: yellow, receiver: blue). Gray mesh spheres are inserted to visualize the position of the robot's body. The resulting calculated channel gain values H_{Pt} along the trajectory are shown in Fig. 4.5b. The LOS channel gain was used as the parameter in the simulation since it resumes the link distance and the angles of transmission, as expressed in (2.5). Robot position 1 corresponds to the one shown in Fig. 4.5a and position indices increase along the trajectory in a counter-clockwise direction (hereafter assumed to be the direction of all the evaluations). The noise level used in the model is adopted from Case Study I ($\nu = -165$ dBm), where it was obtained by calibration with the experimental setup. The summary of the simulation parameters is shown in Table 4.2.

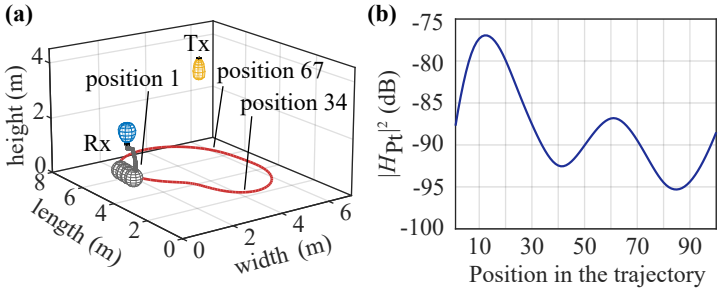

Figure 4.5. Simulation model illustration. (a) 2D Rx trajectory, the radiation and sensitivity characteristics are depicted by colored mesh cones (transmitter: yellow, receiver: blue); the positions 1, 34, and 67 are identified in the 3D trajectory. Gray mesh spheres are inserted to visualize the position of the robot's body. (b) Calculated channel gain values H_{Pt} along the receiver trajectory positions in a counter-clockwise direction.

In order to show the impact of the channel gain on the performance, the EVM was calculated along the trajectory for $I_{\mathrm{rms}} = 200$ mA, $I_{\mathrm{bias}} = 750$ mA, and $G_{\mathrm{B}}/B_{\mathrm{W}} = 1$ (see Fig. 4.6).

Table 4.2. Parameters of the model.

	Parameter	Value
Room	Room size	8 m × 6 m × 4 m
Emitter	Emitter height	4 m
	Orientation vector	[0, 0, -1]
	Semi-angle at half power	30°
	$\mathrm{OFE_{TX}}$ bandwidth	23 MHz
Receiver	Receiver height	1.5 m
	Orientation vector	[0, 0, 1]
	Photosensitive area	7 $\mathrm{mm^2}$
	Field of view	45°
	Responsitivity	0.63 A/W
	$\mathrm{OFE_{RX}}$ bandwidth	23 MHz

For maximum channel attenuation, the signal is more susceptible to disturbance from the noise resulting in a high EVM (for example at position 86, where the channel gain is close to -95 dB). On the other hand, the EVM is significantly lower for positions where the channel attenuation is smaller (for example at position 12: for a channel gain of -77.5 dB, the EVM is close to -16.5 dB).

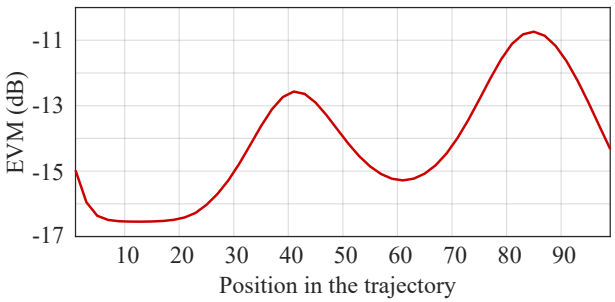

Figure 4.6. Simulated EVM values along the 2D trajectory (see Fig. 4.5b) for $I_{\mathrm{bias}} = 750$ mA, $I_{\mathrm{rms}} = 200$ mA, and $G_{\mathrm{B}}/B_{\mathrm{W}} = 1$.

4.3. Optimization of VLC Link Parameters

As already mentioned in section I, the scope of this chapter is to demonstrate that LSTM-based algorithms can support link parameter optimization. To this aim, optimization of power and spectral efficiency was performed. Both use case scenarios for robotic movements were taken into account with tailored optimization criteria.

The overall aim was to simultaneously minimize the power consumption (P_{T}) and the guard

band (G_{B}) while maintaining the link performance at a specific level. In general, a reduced I_{bias} can be compensated by increasing the OMI or the G_{B}, which reduces intermodulation distortions [23]. By defining ranges for the link parameters and performance, an LSTM optimizer was implemented to assess the optimum points at the corresponding trace positions.

4.3.1. Problem Formulations for Case Studies I and II

The parameters' boundaries of the optimizer for Case Study I are summarized in Table 4.3. Case Study I was the first effort to apply the optimization to increase power and spectral efficiencies by using the direct-current biased OFDM, in which signal clipping of the signal at zero amplitude was intentionally avoided for simplicity, by limiting the maximum value of OMI at 1. The maximum bias current was set to $I_{\mathrm{bias}} = 2$ A because currents above this value can damage the LED used in the experiments conducted to validate the nonlinear model described in Section II-A and, as demonstrated in [115], its luminous efficacy drastically diminishes with such value. In the work presented in [56], it was chosen a relatively high minimum current, because it was used the same LED model and the main objective was to increase bias points aiming at VLC reach extensions. Thus, taking advantage of the experience acquired in such optimization work, in the current work the minimum current was decreased to 50 mA because, unlike [56], one of the main goals is the increase power efficiency.

The experimental data from the digital twin, described in Section 4.2, were taken as reference points ($\mathrm{EVM}_{\mathrm{ref}}(d)$) to evaluate the optimal outcomes from the optimizer. Accordingly, the inequality constraint of the optimization aims to keep the EVM of the optimized solution ($\mathrm{EVM}_{\mathrm{sol}}(d)$) within ± 10 % of $\mathrm{EVM}_{\mathrm{ref}}(d)$, for a given link distance. The solutions that did not fulfill the constraint were penalized and prevented from being added as good solutions.

Table 4.3. Optimization problem formulation for Case Study I.

Min. P_{T} and **Min.** $\frac{G_{\mathrm{B}}}{B_{\mathrm{W}}}$
subject to:
$0.1 \leq \mathrm{OMI} \leq 1$
$50 \leq I_{\mathrm{bias}} \leq 2000$ mA
$0.001 \leq \frac{G_{\mathrm{B}}}{B_{\mathrm{W}}} \leq 1$
$\xi = \left\lvert 1 - \frac{\mathrm{EVM}_{\mathrm{sol}}(d)}{\mathrm{EVM}_{\mathrm{ref}}(d)} \right\rvert \leq 10\%$

In Case Study II, for the two-dimensional movement, the boundaries are similar. However, in this case, the RMS amplitude of the modulation current was used instead of OMI as the amplification parameter, as it more directly represents the average signal power. By this choice, clipping of the signal at zero amplitude is tolerated and takes into account the noise caused by it. The RMS upper bound was set to 1 A. An EVM constraint is also applied here, but in this case, an absolute EVM value is set as a limit, corresponding to a BER below the forward error

correction (FEC) limit. For OFDM transmission with 4-QAM as subcarrier mapping in AWGN channel, the target EVM of -11 dB corresponds to a BER of approximately 1×10^{-4} [123]. Table 4.4 summarizes the formulation problem for Case Study II.

Table 4.4. Problem formulation for Case Study II.

Min. P_{T} and **Min.** $\frac{G_{\mathrm{B}}}{B_{\mathrm{W}}}$
subject to:
$0.01 \leq I_{\mathrm{RMS}} \leq 1$ A
$50 \leq I_{\mathrm{bias}} \leq 2000$ mA
$0.001 \leq \frac{G_{\mathrm{B}}}{B_{\mathrm{W}}} \leq 1$
$\mathrm{EVM}_{\mathrm{sol}} < -11$ dB

For both Case Studies, the electrical transmitted signal power is the calculated RMS power after the superimposed bias current. For the sake of simplification, the considered LED voltage $V_{\mathrm{in}} = 12$ V.

4.3.2. Hybrid Multi-objective Optimization

A hybrid multi-objective optimization (HMO) based on the Non-Sorting Genetic Algorithm III (NSGA-III) and the multi-objective Grey Wolf optimizer (MOGWO) is proposed in this work. This approach aims to achieve higher diversity by combining the two well-established meta-heuristics and choosing one solution over the first combined Pareto front. This approach aims to increase the set of solutions' diversity.

The first stage of the HMO is to obtain the Pareto fronts (F1s) from both evaluated optimizers, working in parallel, for each trajectory position. Thereafter, the Pareto fronts were combined and the dominant set of solutions were removed (see $\mathrm{F1}_{\mathrm{HMO}}$ in Fig. 4.7a).

Since the Pareto front is composed of independent solutions that are not dominated by any other, an objective criterion was necessary to be applied to choose the optimal solution. For this reason, the normalized values of the involved parameters (P_{T} and $\frac{G_{\mathrm{B}}}{B_{\mathrm{W}}}$ in Fig. 4.7b) were taken into account. The minimum Euclidean distance to the origin was considered as the "knee-point", i.e., the best-found parameter set for the given position. The HMO and the selection of the knee-point solution procedures are detailed in Algorithm 4.1.

The NSGA-III and MOGWO parameter settings are summarized in Table 4.5. The parameters were chosen per convenience (empirically), aiming for a faster minimization of the objectives but maintaining the algorithms' abilities to explore and exploit. For more details about the parameters of each multi-objective optimizer, please refer to [4] and [100].

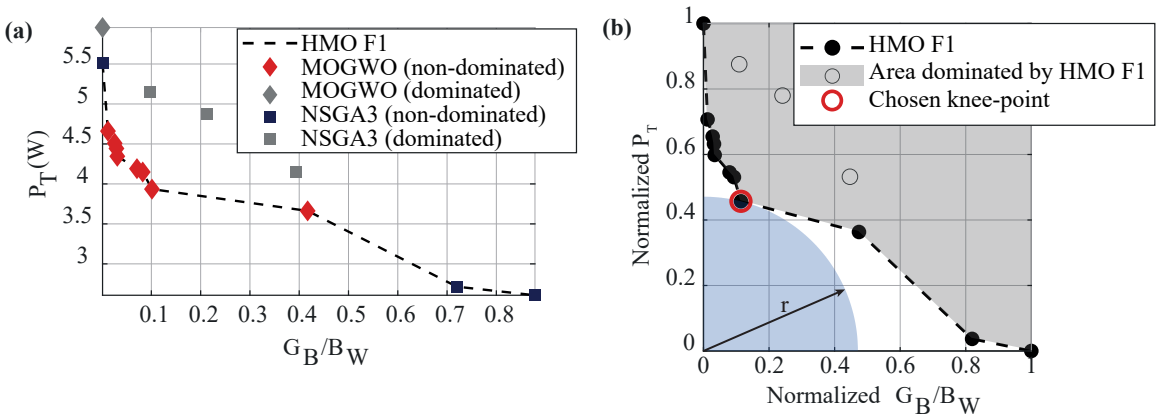

Figure 4.7. HMO procedure illustration for the definition of optimal parameters at a given position. (a) The set of non-dominated solutions is determined by the combination of both NSGA-III and MOGWO Pareto fronts ($\mathrm{F1_{HMO}}$); the dominated solutions of one optimizer are necessarily dominated by solutions of the other optimizer. (b) After normalization of parameters' values ($\widehat{\mathrm{F1}}_{\mathrm{HMO}}$), the knee-point solution for each position is identified as the one with the least Euclidean distance (r) to the origin.

Algorithm 4.1. HMO and knee-point selection procedures.

Input: Pareto fronts from NSGA-III ($\mathrm{F1_{NSGA-III}}$) and MOGWO ($\mathrm{F1_{MOGWO}}$) evaluations
Output: Knee-point solution

1: $\mathrm{HMO} \leftarrow \mathrm{F1_{NSGA-III}} \cup \mathrm{F1_{MOGWO}}$ ▷ Fig. 4.7a
2: $\mathrm{F1_{HMO}} \leftarrow \texttt{NonDominated}(\mathrm{HMO})$ ▷ returns the non-dominated solutions based on (2.44) and (2.45)
3: $\widehat{\mathrm{F1}}_{\mathrm{HMO}} \leftarrow \texttt{NormalizeObjectives}(\mathrm{F1_{HMO}})$ ▷ Fig. 4.7b
4: $r \leftarrow \texttt{EuclideanDistance}(\widehat{\mathrm{F1}}_{\mathrm{HMO}})$
5: $i \leftarrow \min_{\forall i \in \widehat{\mathrm{F1}}_{\mathrm{HMO}}}(r_i)$ ▷ Minimum Euclidean distance
6: $k_{\mathrm{p}} \leftarrow \mathrm{F1_{HMO}}(i)$ ▷ knee-point solution

4.4. Long-Short Term Memory Forecasting

The LSTM architectures and the dataset generation with the robot trajectories for each Case Study are described in the following subsections.

4.4.1. Forecasting Parameters with LSTM in Case Study I

For Case Study I, the interpolation capability of the ANNs allowed parameter estimation for positions (i.e. link distances) between the reference points for which optimized parameter sets exist, and the memorization of past events, that characterizes LSTMs, contributed to the prediction process. To this end, the last (d_{k-1}) and the current (d_k) positions of the robot were defined as the inputs of the LSTM and the link parameters $G_{\mathrm{B}}/B_{\mathrm{W}}$, I_{bias} and OMI as its outputs. A link range between 80 and 400 cm was considered in this case, with a step size of 10 cm. The LSTM input and output features or variables are normalized by the Min-Max scaler, which transforms the data into the range [0, 1]. The main purpose of this scaling is to allow the

Table 4.5. Parameters of the HMO optimizer.

NSGA-III

Parameter	Value
Population Size	30
Number of Iterations	50
Mutation percentage	0.05
Crossover percentage	0.5
Mutation rate	0.05

MOGWO

Parameter	Value
Population Size	30
Number of Iterations	50
Number of Population (wolves)	40
Grid Inflation Parameter (α)	0.1
Grids per each Dimension	20
Leader Selection Parameter (β)	4

variables to contribute equally to the model fitting [124]. The mathematical expression for the Min-Max normalization of a generic variable vector x is

$$x_{\text{scaled}} = \frac{x - \min(x)}{\max(x) - \min(x)}. \tag{4.1}$$

This normalized dataset was generated, allocating to all combinations of d_{k-1}, d_k, and d_{k+1} optimal parameter sets of G_B/B_W, I_{bias}, and OMI for each trace position. The set of the expected optimal parameters was extracted from the knee points of the corresponding Pareto fronts provided by the HMO.

Fig. 4.8 shows the LSTM architecture composed of four hidden layers with 512, 1024, 256, and 64 units, respectively, as well as an output layer with 3 units. Hyperbolic tangent (tanh) and rectified linear unit (ReLu) are the activation functions of the hidden and the output layers, respectively. The LSTM was trained using the Adam optimization algorithm, considering 2048 epochs with a batch size of 8 samples. Each training period includes an evaluation of a loss function to gauge the effectiveness of the neural network. The disparity between the expected output and the predicted output is measured mathematically using the loss function. A neural network's fundamental objective is to minimize the loss function, often known as the prediction or classification error. The loss function was chosen as a multidimensional root mean square error (RMSE), which is defined as

$$\mathrm{RMSE} = \sqrt{\frac{1}{3n}\sum_{i=1}^{n}\left[(\Delta\frac{G_{\mathrm{B}}}{B_{\mathrm{W}}})_i^2 + (\Delta I_{\mathrm{bias}})_i^2 + (\Delta\mathrm{OMI})_i^2\right]}, \tag{4.2}$$

where Δ is an operator that represents the absolute difference between the expected and predicted parameter and n is the number of observed values.

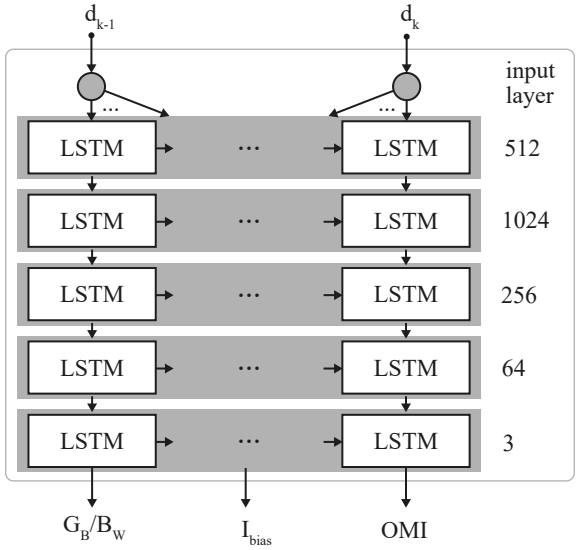

Figure 4.8. LSTM architecture used to predict positions and the VLC parameters of the positions in Case Study I.

4.4.2. Forecasting Channel Gain with LSTM in Case Study II

Event prediction is an important issue to enhance VLC link performance. In Case Study II, the channel gain along the trajectory is predicted and, based on this information, the optimized VLC parameters are chosen. To create different movement patterns, the trajectory was divided into three sections (see Fig. 4.9). The robot can start and end its path at points A, B, or C. This is equally a time series problem because the channel gain values used as output are directly related to the robot's path. Consequently, the LSTM was applied to provide predictions of future channel gain values.

This dataset generation was inspired by a robot working on a task, in which case it must move to different positions to perform this task. If the statistical model of the robot trajectory is well known, the proposed system can be replaced by a lookup table. In this work, the route is randomly generated and the LSTM has the function to forecast the channel gain of a future position. Thus, the dataset was generated based on three points A, B, and C), representing points 1, 34, and 67 of Fig. 4.5b, respectively. The admitted probability for the robot to change its direction of movement at each of these points was set to 50 %. The probability of 50 % was chosen for the determination of the robot direction in the transition points to avoid a biased dataset. If the probability is different for a specific direction, the dataset is biased, and the

prediction error tends to diminish. For example, a robot starting in point A can go to point B (path 1, Fig. 4.9b) or C (path 2, Fig. 4.9b) with 50 % probability. The robot keeps choosing other paths and keeps on moving until it completes the predetermined number of paths.

The performance of the LSTM neural networks is dependent on the number of samples used in the training of the model, with more samples, better performance can be achieved [125]. The number of samples used for training the LSTM model of this case took into consideration all the six possible paths developed by the robot to accordingly forecast the future position of the robot through channel gain. Hence, the number of learning samples used for this training was set as 50 robot paths. This dataset was afterward split into 70 % as a training set, 15 % as a validation set, and 15 % as a test set.

It is worth noting that, the methodology proposed in this work is a concept for potential real-world application. The LSTM training is meant to be evaluated offline, while the forecasting is intended to be assessed online.

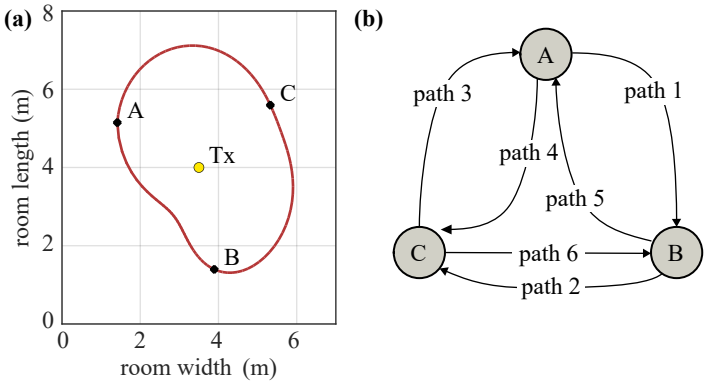

Figure 4.9. (a) 2D trajectory with the segmentation points. (b) Schematic view of the possible robot paths from each segmentation point.

Fig. 4.10 shows the corresponding ANN architecture, which is composed of one layer with 100 LSTM units and an output-dense layer (i.e. a layer that is highly connected with its preceding layer) with one neuron. The hyperbolic tangent was chosen as the activation function. In the training process, the Adam optimization algorithm was selected with 256 epochs with a batch size of 128 samples and the RMSE as the loss function which is defined as

$$\mathrm{RMSE} = \sqrt{\frac{1}{n}\sum_{i=1}^{n}(\Delta H_i)^2}, \tag{4.3}$$

where H is the Min-Max scaled channel gain. The LSTM input size is not a critical architecture parameter if it is greater than three samples, i.e. three past samples. If this condition is met, low training and test RMSE are achieved. In this Case Study, the input sequence of the LSTM considered the last five channel gain values ($H_{k-4}, H_{k-3}, H_{k-2}, H_{k-1}, H_k$) and the output was the predicted one (H_{k+1}). It was assumed five as the number of samples for the LSTM input

to ensure more robustness to the model. Therefore if one sample is corrupted, by noise, for example, the others will retain the network's ability to predict the next channel gain. The LSTM architecture for Case Study II has fewer learnable parameters than the architecture proposed for Case Study I due to the lower number of outputs.

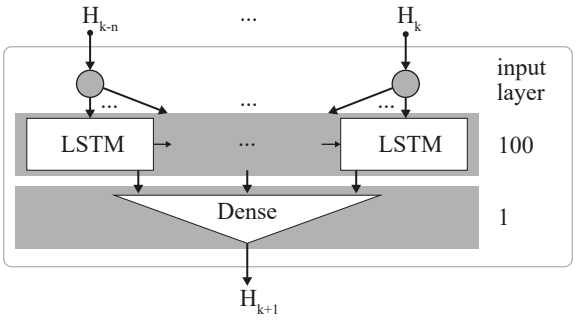

Figure 4.10. LSTM architecture used to forecast the channel gain (H_{k+1}) of a robot receiver in a 2D trajectory.

4.5. Results and Discussion

This section provides and discusses numerical results to demonstrate the performance of the proposed HMO procedure presented in Section 4.3. The results of the LSTM forecasting algorithms, proposed in Section 4.4, are also presented for each Case Study.

4.5.1. Case Study I - Assessing the Optimal Parameters and Forecasting Positions in 1D Traces

Fig. 4.11 shows the VLC system parameters provided by the HMO procedure described in Section 4.3 for various link lengths. The bias current I_{bias} increases with link distance. This is necessary to compensate for the signal attenuation in the optical channel and achieve a sufficient power level at the receiver to overcome receiver noise (Fig. 4.11a). $\frac{G_{\mathrm{B}}}{B_{\mathrm{W}}}$ remains low at values around 0.2 at all distances. Thus, with $G_{\mathrm{B}}/B_{\mathrm{W}}$ = 1 as a reference, the optimization results obtained in Case Study I lead to an SE increase of approximately 66.67 %, on average. The optimized OMI varies between 0.55 and 1, as shown in Fig. 4.11b.

The fixed parameters used in the experiment (Table 4.1) and the corresponding system power consumption $P_{\mathrm{T,ref}} = 5.25$ W were then considered as reference values to assess the attainable power savings through the application of the HMO optimizer. As shown in Fig. 4.12, in almost all link distances, a lower power consumption $P_{\mathrm{T,HMO}}$ is attained with the optimized parameters. For the lower link length values, power consumption decreases by up to $80\ \%$.

To validate the optimal solutions provided by the HMO, the experiments described in Subsection 4.2.1 were repeated with the optimized link parameters. The main goal at this point was to match the performance of the optimized system with the experimental setup, not to achieve

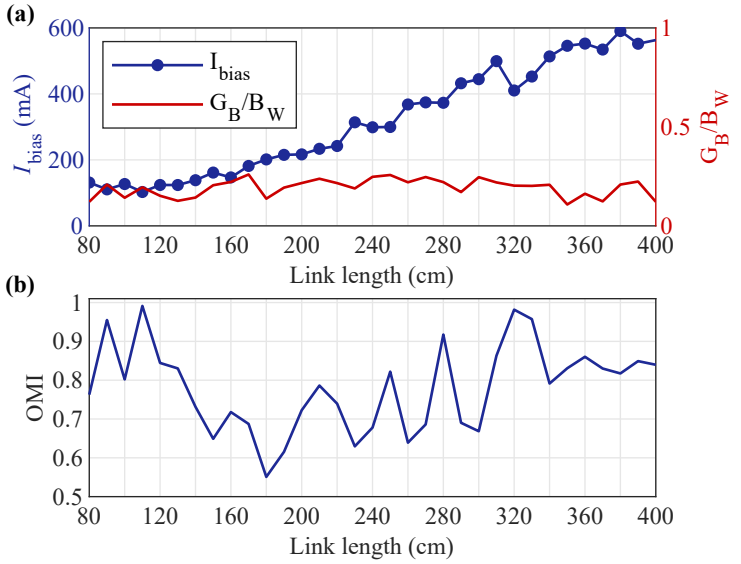

Figure 4.11. HMO solutions for Case Study I. (a) I_{bias} and $\frac{G_{\text{B}}}{B_{\text{W}}}$, and (b) OMI along the link distances in 1D.

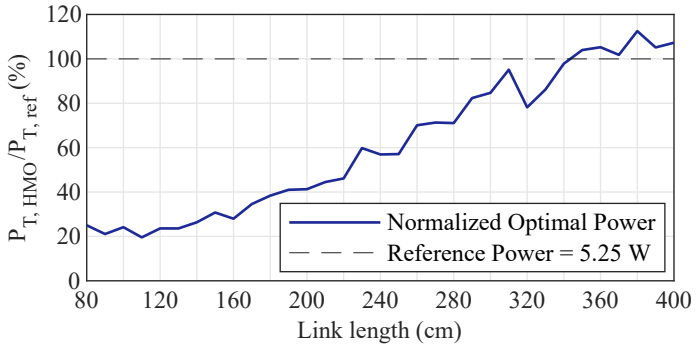

Figure 4.12. Optimized power consumption ($P_{\text{T,HMO}}$) compared with the digital twin calibration power ($P_{\text{T,ref}}$) at a fixed $I_{\text{bias}} = 500$ mA, OMI = 0.35, and $\frac{G_{\text{B}}}{B_{\text{W}}} = 1$ (see Fig. 4.3).

the optimal performance. In Fig. 4.13 the EVM values generated with the optimized parameter sets are compared with the reference EVM values obtained before. The light blue zone in Fig. 4.13 demonstrates that the optimized solutions lie within the aimed ± 10 % EVM tolerance. They also show that at higher link length values, where the power benefit is smaller (see Fig. 4.13), the optimizer leads to slightly better EVM values.

The HMO solutions were then used in the forecasting model described in Subsection 4.4.1. To this aim, the following experiment was carried out: a dataset of 221 routes was generated and divided into 70 % training, 15 % validation, and 15 % testing and served as input for the LSTM algorithm. The LSTM delivered the optimized solutions for each next position as an output.

Overfitting is a phenomenon that arises when a machine learning model gets excessively complicated and fitted to the training data, leading to poor performance on fresh, unknown data. In other words, an overfitted model fails to capture the fundamental relationships between

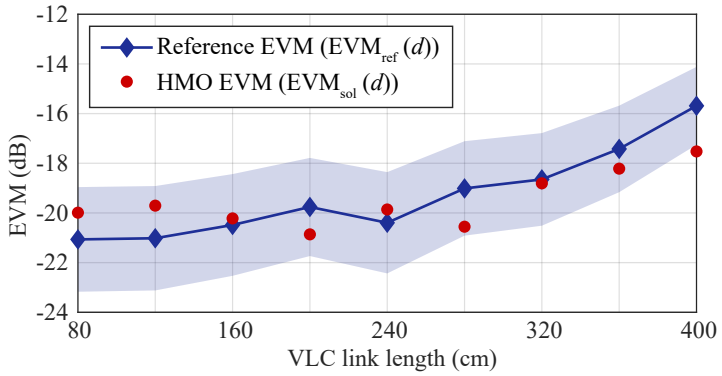

Figure 4.13. Comparison of measured EVM reference values for Case Study I (see Fig. 4.3) with the EVM obtained with HMO solutions. The blue zone indicates the ± 10 % tolerance in the EVM constraint (see Table 4.3).

the input characteristics and the target variable and instead learns the noise and random changes in the training data [126]. Analyzing the training losses, the model checkpoint returned an RMSE of 5.10 % after training and 7.68 % after the test. The convergent loss curves for the train and test dataset shown in Fig. 4.14a demonstrate that overfitting did not occur.

The success of the proposed LSTM in forecasting the optimized VLC communication system parameters was validated by the EVM obtained with the application of its output parameters ($\mathrm{EVM}_{\mathrm{LSTM}}(d)$). As it can be observed in Fig. 4.14b the error between $\mathrm{EVM}_{\mathrm{LSTM}}$ and $\mathrm{EVM}_{\mathrm{ref}}$ remains below 7 % at all link lengths, which shows that that the solutions also meet the error criterion of around 10 % expressed in the Table 4.3.

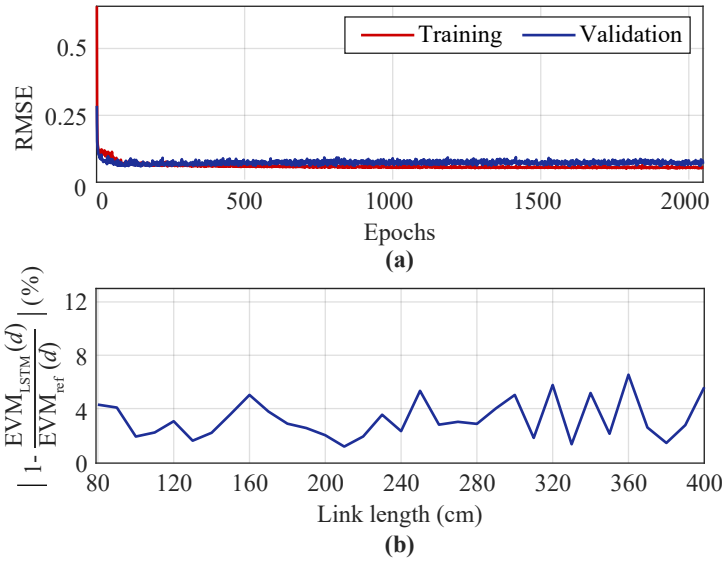

Figure 4.14. Performance of the proposed LSTM for a 1D trajectory: (a) the RMSE loss obtained in the training and testing of the proposed LSTM architecture and (b) system performance deviation with EVM as metric, comparing the performance with optimized parameter sets to the reference values at various link lengths.

4.5.2. Case Study II - Determining Optimal Parameters and Predicting Channel Gain for 2D Trajectories

As described in the problem formulation in Section 4.3, for Case Study II, the absolute EVM was defined as the inequality constraint of the optimization. In a slightly different approach, the optimizer task here was to attain EVM values lower than -11 dB, which would correspond to a BER of 1×10^{-4} for 4-QAM. Fig. 4.15 shows the optimized solutions for bias, RMS currents, and guard-band for all positions of the trajectory shown in Fig. 4.5. The optimized bias current remains under 700 mA and varies according to the channel gain variation (Fig. 4.15a), with higher values for greater channel attenuation. Fig. 4.15b depicts the RMS current results, and it shows that I_{RMS} remains under 300 mA, showing the same behavior as the bias current: with higher channel attenuation, more power is required to maintain the necessary EVM performance. As expected, Fig. 4.15b show that low values of I_{bias} and I_{RMS} are sufficient in the low attenuation regions to maintain the system performance. In these cases, low values of the guard band are required as can be seen in Fig. 4.15c, which also increases the overall spectral efficiency [31]. For example, for the robot positions 10 to 20 (see Fig. 4.15c), the guard-band values are close to the lower bound guard-band stipulated by the formulation problem of $G_{\mathrm{B}}/B_{\mathrm{W}} = 0.001$ (Table 4.4), which corresponds to an increase of 99.80 % of the reference SE.

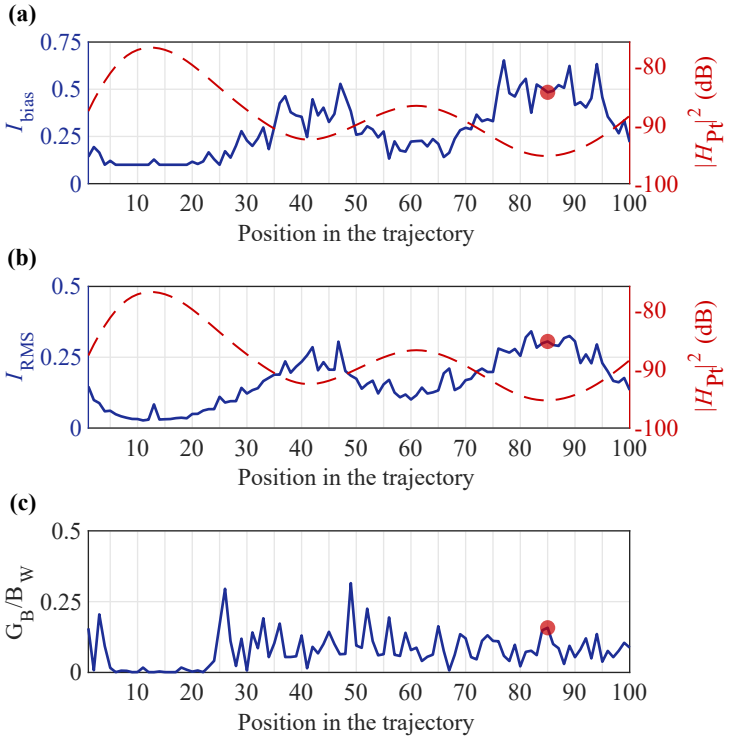

Figure 4.15. Link parameters (a) I_{bias} (left axis), (b) I_{RMS} (left axis), and (c) $G_{\mathrm{B}}/B_{\mathrm{W}}$ obtained with HMO along the robot positions in the 2D trajectory (see Fig. 4.5). The parameters marked with a red circle indicate the "lowest channel gain scenario" to achieve the aimed EVM criterion with fixed parameters. The red dashed curves on the right axes of (a) and (b) correspond to the channel gain of Case Study II.

The benefit of applying the HMO algorithm is highlighted if an alternative link parameter choice is considered without this tool. In this case, to produce a fair comparison, the optimized parameters for the trajectory point with the lowest channel gain, as seen in Fig. 4.5b, is taken as the reference. For the given trajectory, this corresponds to the parameters at position 85 (see red dot markers in Fig. 4.15), where $I_{\text{bias}} = 483.7$ mA, $I_{\text{RMS}} = 305.7$ mA, and $\frac{G_{\text{B}}}{B_{\text{W}}} = 0.157$. The corresponding calculated power consumption is $P = 6.504$ W.

In Fig. 4.16 the calculated power consumption values with the HMO parameters are compared to this reference value. These results demonstrate that through optimization, consumption can be reduced down to ≈ 19.37 % for the positions with low channel attenuation (e.g. among others 11 and 16 positions). Fig. 4.16 also shows some peaks around point 85 that exceed 100 percent. Between points 80 and 90, the channel gain is the lowest compared to the others and therefore the power at the receiver, for the mentioned points, is the most attenuated. As the maximum EVM condition must be satisfied, in this region the transmitted power value is expected to be the highest compared to the ones in other positions of the receiver. The difference between the optimal power results comprised between points 80 and 90 is due to the difficulty of the optimization algorithm in finding global solutions, so the solutions get stuck in local minima in the search space for this noisy scenario.

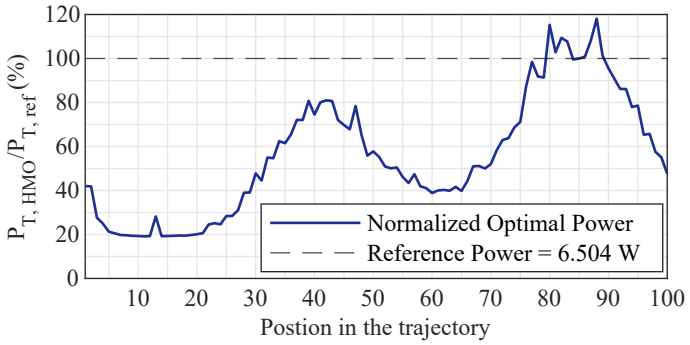

Figure 4.16. Comparison of power consumption with optimized parameters $P_{\text{T,HMO}}$ to the 'lowest channel gain scenario' for the optimized power $P_{\text{T,ref}}$ at various trajectory positions. The power can be minimized to ≈ 19.37 % of the $P_{\text{T,ref}}$ for positions with lower channel attenuation with the optimized parameters for each position in the trajectory.

Subsequently, the LSTM architecture and dataset proposed in Subsection 4.4.2 were evaluated to forecast the trajectory and apply the optimal parameters from the HMO. A computer with a 2.3 GHz Intel Xeon CPU and 12.6 GB of DDR4 RAM was used to run the LSTM simulations.

Fig. 4.17a depicts the losses obtained on the LSTM training process, showing two convergent curves. This confirms that overfitting did not occur. The best LSTM training achieved an RMSE equal to 0.63 % for training, and 0.48 % for validation.

Fig. 4.17b shows the results for the expected and predicted values after the LSTM test. Each prediction took between 2 to 4 milliseconds to process. The fact that the two curves are similar

corroborates the low RMSE values on the training and validation dataset. The robot changes its trajectory with $50\ \%$ chance towards the neighbor position, as described in subsection 4.4.2. Because of that, the LSTM prediction errors are more likely to happen in the trajectory transition points (see Fig. 4.17b vertical dashed lines). To emphasize the lower prediction error, Fig. 4.17c shows the error between the predicted and expected gains. The prediction errors are more prominent at the points of path transitions. The absolute predicted gain error over time remains lower than $0.7\ \%$.

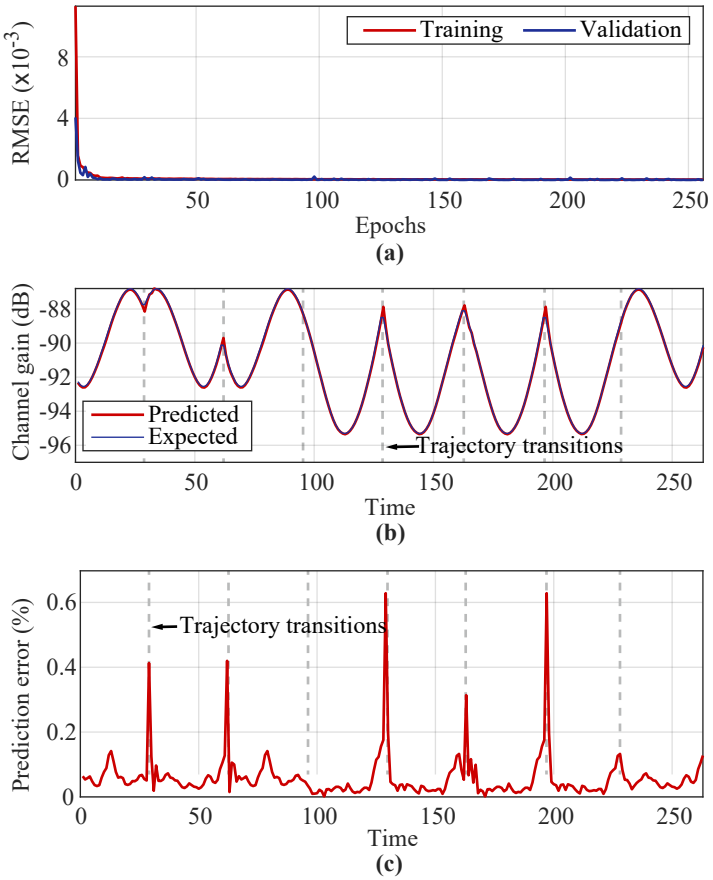

Figure 4.17. Results of forecasting in a 2D trajectory with LSTM. (a) The losses along the epochs in the LSTM training process show an RMSE of around $0.6\ \%$. (b) The predicted (red line) and the expected channel gain (blue line). (c) The error between predicted and expected channel gain values. Dotted lines indicate the positions, at which trajectory transitions take place.

4.6. Final Remarks

In this chapter, optimization and artificial intelligence procedures were proposed aiming at simultaneously increasing power and spectral efficiency (SE) of visible light communication systems for two exemplary industrial scenarios. To this aim, it was presented two Case Studies involving one and two-dimensional robotic movements, respectively. A hybrid multi-objective optimization (HMO) was proposed using a combination of the non-sorting genetic algorithm

III and the Grey Wolf optimizer to minimize the signal's transmitted power and the guard band while constraining the error vector magnitude (EVM) metric. Thereafter, the optimal solutions were applied to a long-short-term memory neural network to forecast the future link parameters (Case Study I) and channel gain (Case Study II).

For Case Study I, the HMO solutions provided a reduction of the RMS power consumption of up to $\approx$ 80 % as compared to the non-optimized reference power and a minimized guard-band of down to $\approx 20\ \%$ of the bandwidth as compared to the fixed parameters case, which is equivalent to an SE increase of $66.67\ \%$ for the evaluated link. The optimal parameters were experimentally tested and the EVM comparison validated both the proposed optimization, as well as the developed digital twin model. The success of the proposed LSTM in forecasting the optimal parameters was expressed by the low RMSE, under $7\ \%$ with no overfitting.

For Case Study II, the optimized solutions were highly correlated with the channel gain. In the evaluated scenario, the power consumption was reduced by approximately $80.64\ \%$ as compared to a constant power setting along the trajectory. For some points, the guard band was minimized to the lower bound ($G_{\mathrm{B}}/B_{\mathrm{W}}$ = 0.001) when lower power was required. The LSTM results show that the neural network architecture can be much simpler if the objective is to predict the channel gain of the robot's future position. Simulation results show that the RMSE of the predictions obtained after testing the proposed LSTM architecture was approximately $0.5\ \%$.

CHAPTER 5.

Convolutional Neural Network Direct Equalization

5.1. Introduction

In broadband systems, the transmitted signals can be distorted by frequency-selective channels or noise. To obtain a correct detection, at the receiver is implemented the Channel Estimation (CE) and the symbols' equalization [127]. For multi-carrier communication schemes, the channel response is predicted by pilots located at known frequency bins. Two different structure strategies are commonly used for channel estimation: the block-type and the comb-type [128]. In the block type, the pilots are periodically arranged in time, and they fill all sub-carriers. In the comb type, the pilots are equally spaced in the frequency domain and allocated in some sub-carriers. Since there are frequency bins without pilots, for the comb-type structure, is mandatory the interpolation for predicting the adjacent frequency responses.

The channel estimation can be implemented using traditional algorithms, for instance, the LS and Minimum Mean Square Error (MMSE). The LS is well known for its low complexity achieved by an element-wise division operation, but it presents a reduced performance with the increase of channel noise power [129]. Better performance can be achieved by the MMSE channel estimator. Nonetheless, it is required the implementation of matrix inversions and the previous knowledge of both the channel autocovariance and the noise variance, which makes this channel estimator unfeasible due to its high complexity [71, 130].

The following literature review shows the application of artificial intelligence techniques to channel estimation algorithms. In [131], the authors present a denoising and deep learning (DL) super-resolution approach, in which the positions of the pilots were considered as the input of the neural network (a low-resolution image) and the output of the neural network was the estimated channel response (a high-resolution image). A deep neural network known as Deep Image Prior is presented in [129]. For this approach, denoising without the training process is applied for channel estimation, reducing the signal received noise. In [132], the authors propose an end-to-end deep learning-based approach that estimates the channel state information implicitly and recovers the transmitted symbols directly with the drawback of a long training time. The optical channels estimation in coherent optical OFDM systems using DL architectures are presented in [133] and [134], and in [135] the studies were continued to wireless multiple-input multiple-output (MIMO) systems. In [136] and [137], deep neural networks

were used for underwater acoustic OFDM direct detection of binary data. Notwithstanding, the presented studies target the channel estimation, and thereafter process the interpolation and equalization, separately.

The authors in [138] propose a channel estimation strategy based on Deep Neural Networks (DNN) that performs as well as LS and MMSE schemes but requires fewer pilots. In [139] improvements are made in the reduction and then the removing the number of orthogonal pilots without losses in terms of BER.

Since the structure of the channel estimation is the comb-type, and it is not approached as sequential data, we should not apply a RNN, that essentially need the sequential input data characteristic [140]. The Deep Neural Network (DNN) should require a huge amount of data for training and also performs a considered number of operations [107].

This chapter introduces the mapped OFDM symbols equalization using CNN in a visible light communication channel. The presented CNN model is denominated CNN-DE due to the direct detection of symbols without channel estimation, interpolation, and element-wise division (zero forcing or least square equalization) performed in conventional systems. We used the CNN for the equalization regarding the dependency of each channel response (relationship with the neighborhood), which is taken into account with the CNN [141]. The regression and classification of CNN-DE approaches are also discussed in this chapter.

The remainder of this chapter is structured as follows. Section 5.2 presents the proposed methodology for CNN-based equalization. Section 5.3 is devoted to the simulation and results descriptions. The characterization of an experimental setup, the nonlinear LED model, the CNN-DE performance, and the computational complexity analysis are shown and discussed in Section 5.4. This chapter's final remarks are presented in Section 5.5.

5.2. The CNN-Direct Equalizer

5.2.1. The dataset generation

The OFDM block diagram was developed as illustrated in Fig. 5.1 (a). The mapped symbols at the transmission are set to be the CNN-DE target (X), composed of the data (carrying information) and the pilots (known data) at a comb-type structure due to a possible fast variation of the channel response. The N_{p} pilots are equally spaced in frequency by $\Delta_{\mathrm{f-p}}$ Hertz, as shown in Fig. 5.1 (b).

The mapped symbols are multiplexed by the IFFT transform, the cyclic prefix is appended and, at a specific carrier frequency f_{c}, the band base signal is upconverted by the analog quadrature-amplitude modulation (QAM). The signal is transmitted over a VLC SISO mode channel as previously described. At the receiver, the CP is removed and the FFT demodulation is processed. The distorted mapped symbols are set to be the CNN-DE input (Y).

The shape of the input and target tensors, for this approach, are $N_{\mathrm{FFT}} \times 2$, where the number 2 refers to the in-phase and quadrature coefficients of the constellation symbols. For the regression approach, the input of the CNN-DE equalizer has the same shape as its output. With the CNN-DE properly trained, the evaluation of the model prediction provides the equalization of the received symbols that afterward are converted into binary data.

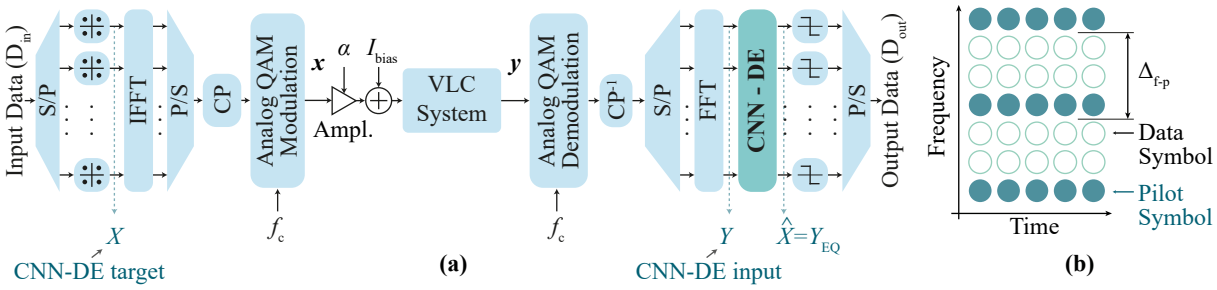

Figure 5.1. DCO-OFDM scheme dataset generation for the CNN-DE training and test. (a) DCO-OFDM block diagram. (b) The comb-type pilot arrangement was utilized in this work.

5.2.2. The CNN-DE Regressor Structure

The CNN-DE input is a complex vector reshaped into a tensor of two channels, for real and imaginary parts, maintaining its spatial disposition. The CNN-DE model as a regressor is depicted in Fig. 5.2 and also summarized in Table 5.1.

A one-dimensional convolution (Conv1D) layer is applied with 64 kernels of size 4, which feeds a rectified linear unit (ReLU) activation function. The CNN-DE performs a batch normalization (BN) motivated by its capacity to act as a regularizer and to enhance the training speed by supporting higher learning rates [142]. Subsequently, a feature map downsampling is performed by the 1D Max-poling layer (MaxPool) [143], and thereafter, another Conv1D layer (4 kernels of size 4 and ReLU as activation function) is applied. The tensor is flattened (converted into a one-dimension tensor) and fed into a dense layer of 256 units with a *tanh* as output activation function. The *tanh* is used instead of the sigmoid activation function because, as stated by [107], typically, the hyperbolic tangent activation function outperforms the logistic sigmoid.

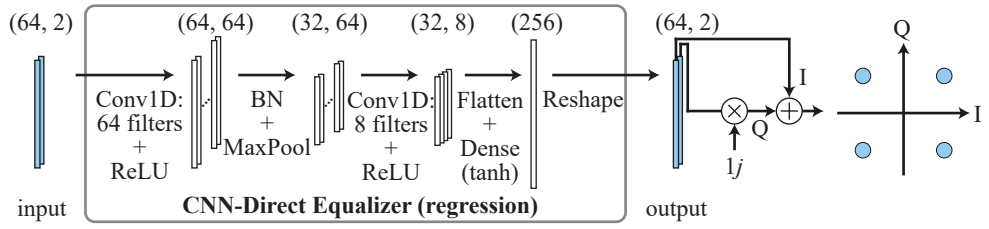

Figure 5.2. Proposed CNN-direct equalizer model as a regressor.

Table 5.1. Summary of the CNN Direct Equalizer Model as a Regressor.

	Input Shape	**Output Shape**	**Activation Function**
Input Data	-	(64,2)	-
Conv1D	(64,2)	(64,64)	ReLU
Batch Normalization (BN)	(64,64)	(64,64)	-
MaxPooling1D	(64,64)	(32,64)	-
Conv1D	(32,64)	(32,4)	ReLU
Flatten	(32,4)	(128)	-
Dense	(128)	(128)	tanh
Reshape	(128)	(64,2)	-
Output Data	(64,2)	-	-

5.3. Results and Discussion

5.3.1. Implementation Features

Table 5.2 shows the parameters for the OFDM signals generation. The QAM analog modulation is applied with a carrier frequency f_{c} tuned for the most linear region of the VLC fading channel. An off-the-shelf 10 MHz LED was modeled as the source and a Thorlabs 10 GHz photodiode was modeled for the photodetection [25].

Table 5.2. Summary of the OFDM parameters.

Parameter	**Symbol**	**Value**
Effective Bandwidth	B_{W}	5 MHz
(I)FFT size	N	64
Subcarrier mapping	M	4-QAM
Cyclic Prefix	CP	25%
Subcarrier spacing	Δ_{f}	78.125 kHz
Oversampling factor	K	4
Central frequency	f_{c}	7.5 MHz

A total dataset of 50,000 samples was generated in order to train, validate and test the proposed CNN-DE. The data was split into 70 % for training, 15 % for validation, and 15 % for testing. The generated datasets during the current study are available in the GitHub repository (link). At the training process, the minimization of the average of the squared differences between the predicted $\hat{X}(k)$ and actual values $X(k)$ was evaluated by the mean square error (MSE) loss function expressed as

$$\text{MSE} = \frac{1}{N}\sum_{k=0}^{N-1}\left[X(k) - \hat{X}(k)\right]^2. \tag{5.1}$$

The Adam optimizer (short for Adaptive Moment Estimation) is applied to the CNN-DE training to update network weights iteratively based on the input data utilizing the ideas of momentum and adaptive learning rates in conjunction to effectively update the model parameters during the optimization process [144]. For this problem, the learning rate of the optimizer was set to 0.001 and a batch size of 64. The training hyperparameters were chosen empirically and are listed in Table 5.3. The presented CNN-DE was implemented using the TensorFlow library version 2.8.2. The machine used for the experiments was configured as follows: (*i*) Linux OS, Ubuntu 18.04.2; (*ii*) 1-core hyperthreaded Xeon Processors at 2.3 GHz; (*iii*) DDR4 RAM memory 12.6 GB; (*iv*) Hard Disk 33 GB; (*v*) Tesla K80 with 2496 CUDA cores, and 12GB GDDR5 VRAM dedicated memory. The model training took approximately 3 hours to evaluate 50 epochs.

Table 5.3. CNN-DE hyperparameters.

Parameter	Value
Mini Batch Size	64
Training samples	35 k
Validation samples	7.5 k
Test samples	7.5 k
Max Epochs	50
Optimizer	Adam
Learning Rate	0.001

5.3.2. Performance Evaluation Methods

After the CNN-DE model testing, the received symbols and data are compared with the transmitted ones, in order to generate a quantitative analysis. The MSE, calculated as (5.1), indicates how different are the equalized data symbols (real and imaginary parts) from the transmitted mapped symbols. Beyond the MSE, the bit error rate (BER) and the error vector magnitude (EVM) communication metrics are also evaluated.

5.3.3. Performance evaluation of the proposed CNN-DE

The equalization via CNN-DE was assessed by testing the model and varying the number of pilots, equally spaced. The transmitted and equalized symbols were compared with the traditional comb-type LS channel estimation, in terms of MSE and EVM. After the LS estimation,

the spline interpolation method [145] was executed for the channel estimation of data subcarrier positions, and succeeded by the computation of the BER metric.

The MSE performances of the CNN-DE and the LS-based equalization are shown in Fig. 5.3. As shown, at high SNR values, CNN-DE performances are the same for 4, 16, and 32 pilots. Moreover, the LS outperforms the convolutional direct equalization for SNR $>$ 10 dB.

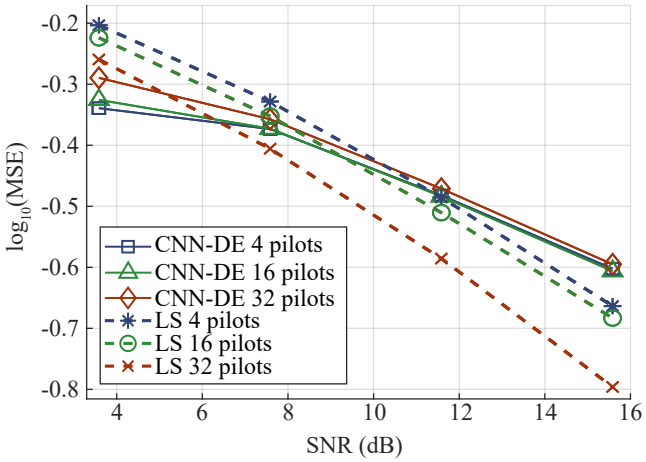

Figure 5.3. MSE *vs* SNR for 4, 16, and 32 equally spaced pilots.

The EVM shows a similar trend as the MSE, as seen in Fig. 5.4: for lower SNR ($<$ 10 dB), the CNN-DE outperforms the LS-based equalization. Thus, it can be concluded that in scenarios with possible adjustment in the luminous intensity (i.e. LED signal power), in dimerized VLC systems, the proposed equalization scheme is a suitable solution.

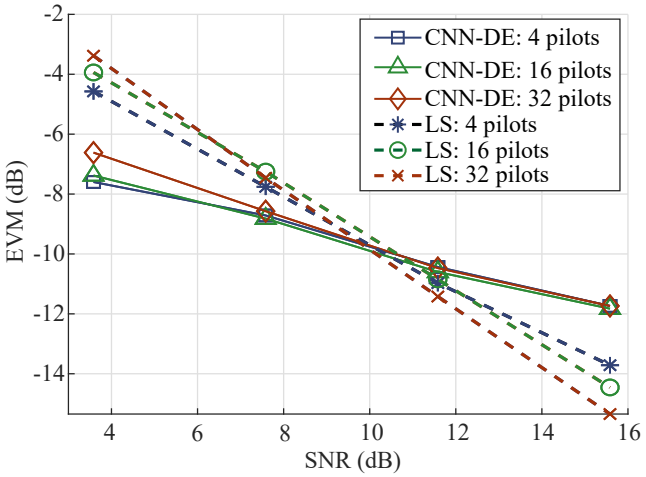

Figure 5.4. Error vector magnitude over the channel SNR variation for the proposed CNN-DE and the traditional LS.

The evaluation of the BER metric over the channel SNR variation is displayed in Fig. 5.5. The same performance is observed for the CNN-DE 16 and 32 pilots for SNR $>$ 10 dB. These results reinforce the adoption of the proposed CNN-DE in SISO VLC systems.

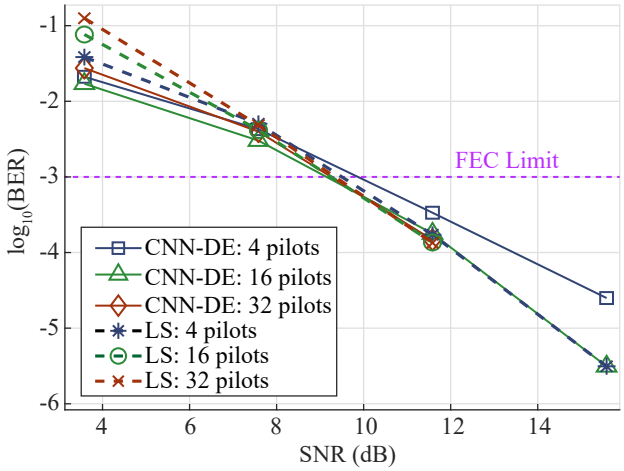

Figure 5.5. BER *vs* SNR for CNN-DE and LS. The behavior of the CNN-DE outperforms the LS for lower SNR values.

5.4. Adding Practical Features to the Numerical Model with Experimental Characterizations Results

5.4.1. The VLC System Frequency Response

In order to determine the frequency response of a VLC system, an optical back-to-back (B2B) characterization is necessary. To confirm the suitability of the channel estimation through the comb-type arrangement, we compared its estimation with experimental results obtained by *(i)* the frequency scan method, *(ii)* the measurements with a network analyzer, and *(iii)* the estimation from OFDM training signals. The frequency scan method consists in conveying sinusoidal signals in different frequencies and performing the Fourier transform at the receiver to achieve the frequency response. The method based on the measurements with the Network Analyzer, employed Anritsu's MS2038C network analyzer after a proper set of parameters and calibration, to measure the frequency response of the VLC system. The profile of the amplitude characteristic of the VLC transfer function was captured respecting the intensity limits that can saturate the photodiode. The experimental results were compared with the estimation obtained from OFDM training signals, in which the received spectrum is analyzed to estimate the channel frequency response.

Fig. 5.6 shows the VLC link low pass characteristic and the inset is shown the experimental setup for the channel estimation. The three above-mentioned methods were applied and the curve's proximity validates the channel estimation with the comb-type arrangement. In the VLC setup, the LED presents the main bandwidth limitation ($\approx$ 10 MHz).

5.4.2. Modeling of the LED nonlinearity based on experiments

The electrical modulating signal, proportional to the data signal $x(t)$ by the amplification factor (α), is superimposed onto the LED bias current I_{bias} because the electrical current inten-

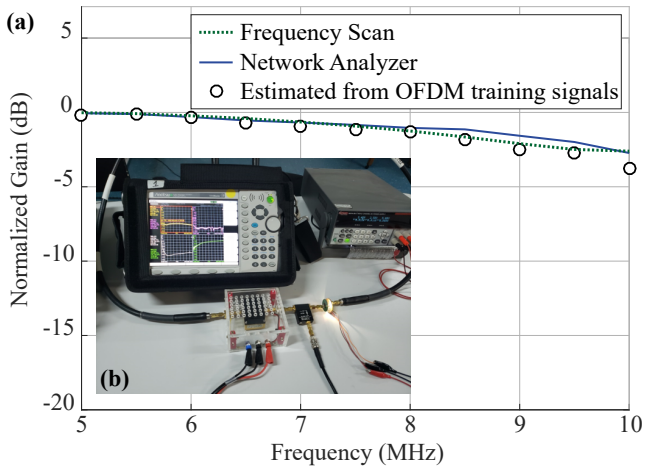

Figure 5.6. Channel frequency response. (a) Normalized channel gain for the VLC setup for optical back-to-back frequency characterizations. (b) Setup for the channel estimation with Anritsu's MS203 network analyzer.

sity should not be negative [146]. This provides an LED current given by (2.33). The LED's output optical illuminance (L_{in}) depends on the modulating signal I_{in} according to (2.1).

To approximate the behavior of the numerical model to the VLC experimental setup, we added an optical intensity versus polarization current model obtained after experimental characterization of a commercial LED, to evaluate its impact on the system performance. The nonlinear behavior of the white LED, depicted in Fig. 3.2, was achieved with the setup shown inset. The optical intensity measurements were obtained with a lux sensor. The numerical model of (2.1) can be approximated by the experiment using $L_{\max} = 755$ lux, $\zeta = 20$, and $k = 1.9$.

5.4.3. CNN-DE for Symbol Classification

As a second approach for the CNN-DE, it is proposed hereafter a classifier, in which the inputs are the real and imaginary parts of the OFDM symbol in the reception, the same as proposed in the first approach (see Fig. 5.2). Differently from the regressor version, the classification version of the equalizer outputs the classes of the OFDM symbols (Fig. 5.7a). The structure of the CNN-DE as a classifier is almost the same as the regressor but the application of the the softmax for multi-class classification as the output activation function. The model characteristics are also summarized in Table 5.4.

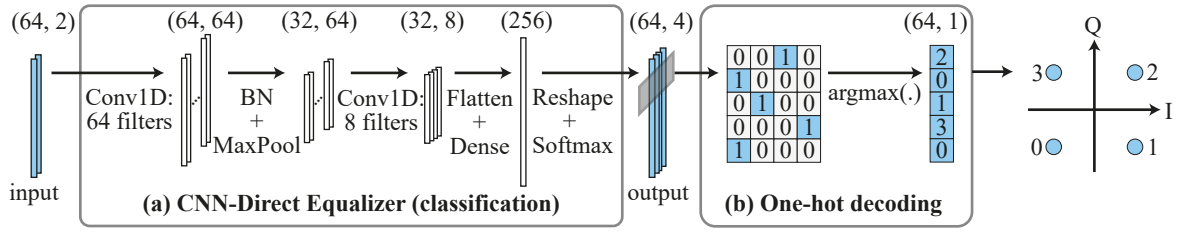

Figure 5.7. Proposed CNN-direct equalizer model as a classifier.

Table 5.4. Summary of the CNN Direct Equalizer Model as a Classifier.

	Input Shape	**Output Shape**	**Activation Function**
Input Data	-	(64,2)	-
Conv1D	(64,2)	(64,64)	ReLU/tanh
Batch Normalization	(64,64)	(64,64)	-
Max Pooling	(64,64)	(32,64)	-
Conv1D	(32,64)	(32,8)	ReLU/tanh
Flatten	(32,8)	(128)	-
Dense	(128)	(256)	ReLU/tanh
Reshape	(256)	(64,4)	-
Output Data	(64,4)	-	softmax

It should be emphasized that the CNN-DE model is dependent on the modulation order M. The shape of the dense layer is $(N_{\mathrm{FFT}} \times M, 1)$ and the output shape is (N_{FFT}, M), because the number of classes for the CNN-DE is the exact number of the OFDM symbols M. For 4-QAM modulation ($M = 4$), the output data predicted by the model are one-hot decoded, and the data are detected as seen in Fig. 5.7b. In this second strategy, it is also intended to examine which activation function – ReLU or tanh – has better performance as the model's internal operation.

Additionally, the cross-entropy is applied as the loss function in the training process of the CNN-DE neural network as a classifier. The hyper-parameters were the same as those used in the first approach.

5.4.4. Performance Analysis

The described practical features were applied to the VLC system model utilized to evaluate the CNN-DE equalization. The application of CNN-DE in OFDM-based VLC system equalization considers the LED nonlinear characteristic, and for the sake of simplicity, the dataset is generated for LOS VLC channels.

In order to investigate the CNN-DE capability to overcome the nonlinear effects caused by the LED, the model activation functions have to be carefully chosen, since these elements are the most responsible for introducing nonlinearity to the predictions. We evaluated the CNN-DE with *ReLU* and *tanh* as the convolutional layers activation functions.

The BER results for CNN-DE (*reLU*), CNN-DE (*tanh*), and LS are shown in Fig. 5.8. The CNN-DE with different activation functions performs similarly. Additionally, the equalizer based on CNN BER performance is close to the LS, with slightly lower values for SNR > 15 dB.

Fig. 5.9 shows the EVM results for the evaluated equalizers. For SNR > 15 dB, the EVM metric of the CNN-DE (*tanh* and *ReLU*) achieves better results if compared with LS. This is

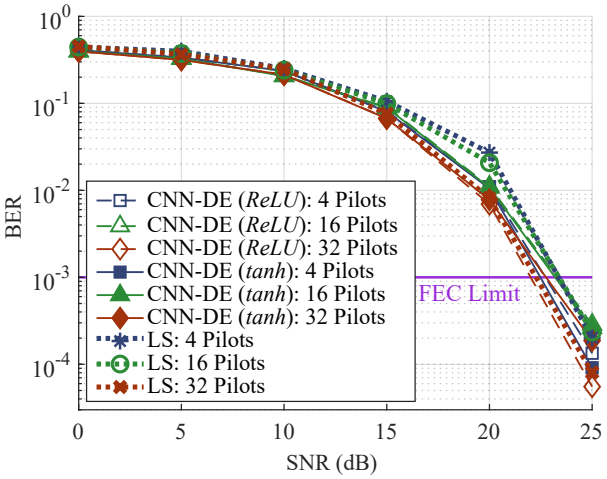

Figure 5.8. Bit error rate for LS and CNN-DE with internal activation functions *ReLU* and *tanh*.

due to the evaluation of the one-hot decoder at the output of the CNN-DE model; this model tends to perform better for solutions with lower BER (higher SNR).

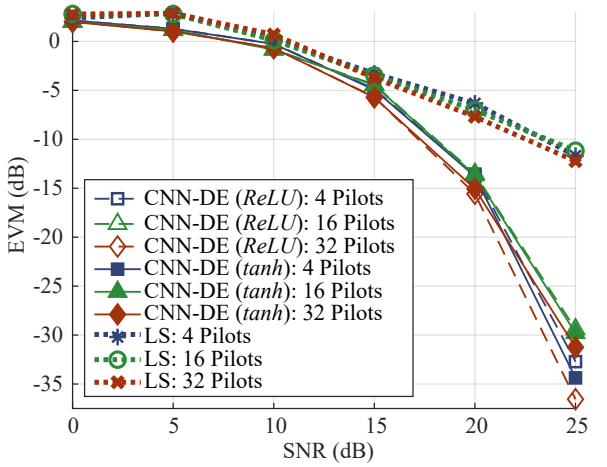

Figure 5.9. Error vector magnitude for LS and CNN-DE with internal activation functions *ReLU* and *tanh*.

The Confusion Matrix, or error matrix, is a table that allows the performance visualization of a supervised classification learning [147]. This matrix summarizes the classification performance of a classifier with respect to the test data applied. The matrix rows represent the instances in an actual (true) class while each column represents the instances in a predicted class [148]. Fig. 5.10 shows the Confusion Matrix of the proposed CNN-DE (*tanh* and *ReLU*) for the approximated VLC model at SNR = 30 dB. The confusion matrices highlight the BER results (see Fig. 5.8), the CNN-DE (*tanh*) performs better for 4 and 16 pilots, while CNN-DE (*ReLU*) produces fewer errors in the classification for 32 pilots.

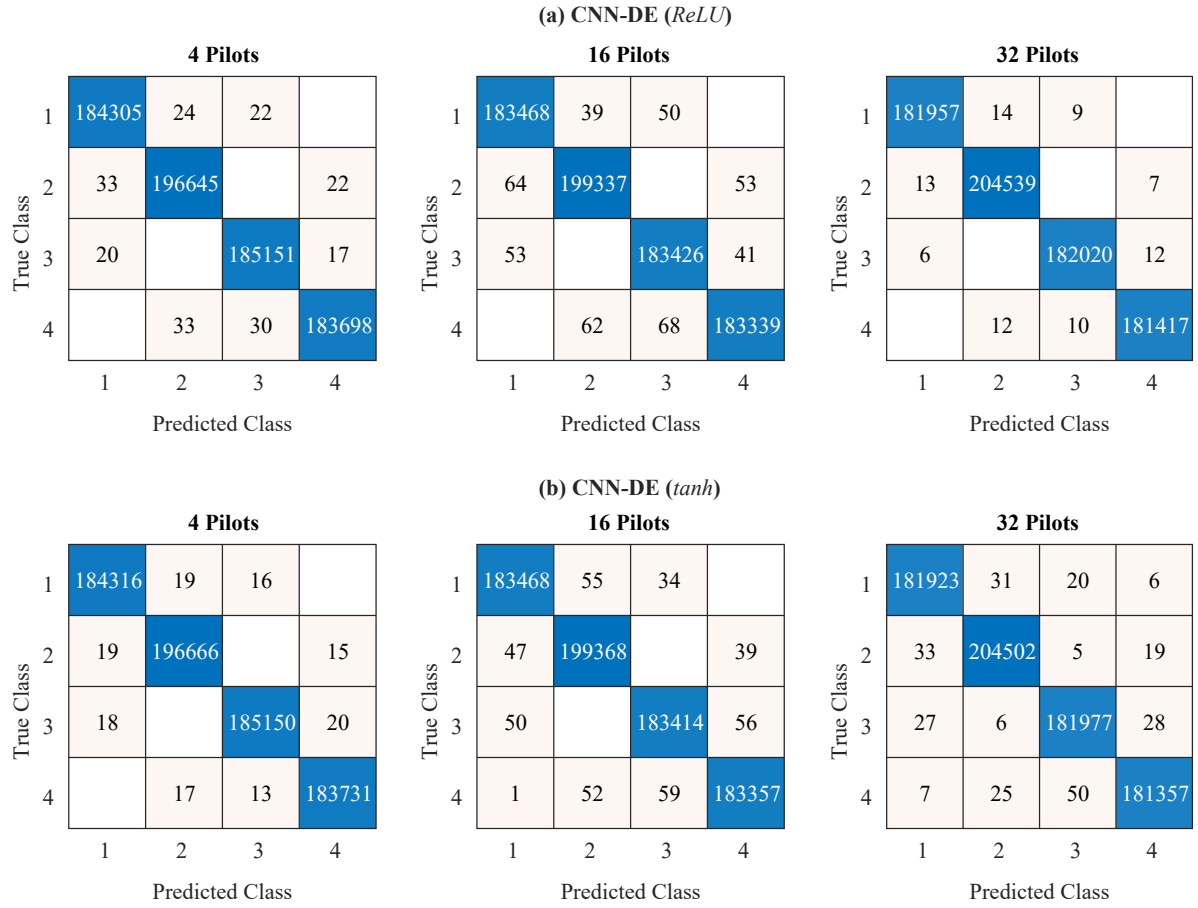

Figure 5.10. Confusion Matrices (CM) for CNN-DE for 4, 16, and 32 pilots for the comb-type distribution in OFDM symbols with $N_{\mathrm{FFT}} = 64$ in a scenario of SNR = 30 dB. (a) shows the CM for CNN-DE internal activation functions ReLU and (b) *tanh*. The empty cells indicate that there is no error between the expected and the specific cell classification.

The classification accuracy of each equalization model varying the number of pilots (4, 16, and 32 pilots) and the type of activation function (*ReLU* and *tanh*) of Fig. 5.10 is summarized in Table 5.5.

Table 5.5. Accuracy of CNN-DE for 4, 16, and 32 pilots with the activation function being *ReLU* or *tanh*.

Number of pilots	**Accuracy (%)**	
	CNN-DE (ReLU)	**CNN-DE (tanh)**
4 pilots	99.973	99.982
16 pilots	99.943	99.948
32 pilots	99.989	99.966

5.4.5. Computational Complexity Analysis

The complexity of the proposed CNN direct equalizer model is achieved in terms of the number of performed operations per transmitted bits. For the sake of simplicity, the activation functions were not considered in the calculation, since they are not dominant if compared with other operations. Considering that, in time inference:

(*i*) a dense layer with input $x \in \mathbb{R}^n$ and output $y \in \mathbb{R}^m$ performs #DENSE$(n, m) = 2nm$ operations; (*ii*) a BN layer with input $x \in \mathbb{R}^{n \times d}$ performs #BN$(n, d) = 2(n + d)$ operations; (*iii*) a conv1D layer with input $x \in \mathbb{R}^{n \times d}$ and f filters of size $k \times d$ performs #CONV1D$(n, d, k, f) = (2d - 1)(n - k + 1)kf$ operations; (*iv*) a MaxPooling1D layer with input $x \in \mathbb{R}^{n \times d}$ and p the pool size performs #MAXPOOL1D$(n, d, p) = (p-1)(n-p+1)d$ operations. Then, the number of operations of the proposed CNN-DE architecture is equal to:

$$\begin{aligned} n_{\text{oper}} &= \text{\#CONV1D}(64, 2, 4, 64) + \text{\#BN}(64, 64) + \\ &\quad \text{\#CONV1D}(32, 64, 4, 8) + \text{\#DENSE}(128, 256) + \\ &\quad \text{\#MAXPOOL1D}(n, d, p) \\ &\quad = 246,936 \text{ operations.} \end{aligned} \tag{5.2}$$

The number of transmitted bits can be achieved by considering the OFDM parameters (see Table 2): each mapped symbol is represented by $k = \log_2(M)$ bits; each OFDM frame is composed by N_{s} data subcarrier (N_{FFT}-N_{p}); and the test OFDM signal considered n_{frame} OFDM frames (equivalent to the number of test samples, see Table 3). Therefore, the number of transmitted bits n_{bits} is given by

$$\begin{aligned} n_{\text{bits}} &= k \times N_{\text{s}} \times n_{\text{frame}} \\ &= \log_2(M) \times (N_{\text{FFT}} - N_{\text{p}}) \times n_{\text{frame}} \end{aligned} \tag{5.3}$$

Finally, the complexity of the CNN-DE for the classification approach can be expressed as

$$C_{\text{CNN-DE}} = \frac{n_{\text{oper}}}{n_{\text{bits}}}. \tag{5.4}$$

The CNN-DE equalization structure presented in this work was based on the 4-QAM modulation. In this case, the architecture is the same regardless of the number of pilots. Based on this, increasing the number of pilots, the number of bits per frame is diminished, and, consequently, the complexity increases. The calculated complexities according to the number of pilots are listed in Table 5.6.

Table 5.6. Complexity of the CNN-DE.

Number of pilots	Complexity ($\times 10^3$ operations/bit)
4	2.058
16	2.572
32	3.858

5.5. Final Remarks

In this chapter, it was presented the applicability of deep learning architectures at the equalization of OFDM modulation scheme in a visible light communication (VLC) system. This work's framework considered the comb-type pilot arrangement and performed convolutional neural networks (CNN) to directly detect the mapped symbols with no need for channel estimation, interpolation, and element-wise division of an OFDM scheme.

The reported results show that the equalization scheme based on CNN outperforms the OFDM systems with equalization based on least square estimation for scenarios of low signal-to-noise ratio (SNR), regardless of the nonlinearity of the VLC systems. And based on this finding, for dimerized VLC systems that require a reduction in the LED power signal (low SNR), the proposed AI-based equalization scheme is a suitable solution.

In a second approach, a realistic model extracted from a real SISO VLC system is utilized for the dataset generation. The frequency response was determined by frequency scan, network analyzer, and estimation from OFDM training signals. The LED's nonlinearity was also contemplated and the CNN-DE was capable of equalizing the OFDM symbols without any other computations. The achieved CNN-DE and the LS-based equalization results are similar, and in terms of EVM, the CNN-DE outperforms the LS method for SNR > 15 dB. We also investigated the activation functions of the CNN-DE, and the results for both EVM and BER show that the performances are comparable.

CHAPTER 6.
Conclusions and Future Directions

6.1. Summary

The objectives of this thesis were to investigate the nonlinear LED effects, VLC parameters, and its performance for conventional and constant-envelope direct current optical OFDM, in order to enhance the system performance, increase power and spectral efficiencies, and consequently increase the VLC link distances, with the introduction of artificial intelligence techniques, such as metaheuristics and machine learning. In order to achieve the thesis objectives, the visible light communication system principles, multi-carrier OFDM modulation schemes for VLC, and soft computing artificial intelligence topics were revised. NSGA-II is used to exploit the LED nonlinear operation region, with the algorithm of minimizing the required signal-to-noise ratio (SNR) for a bit error rate BER = 1×10^{-3} and maximizing the overall SE by minimizing the optical guard-band, with and without a constant envelope (CE).

Results show that the SNR decreases with the increasing guard band due to intermodulation distortions. With VLC systems with CE signals, a guard-band of 6 % of the signal bandwidth was obtained for SNR values of ≈ 10.8 and ≈ 24 dB, for 4-QAM and 16-QAM mappings, respectively, against the SNR values of ≈ 13 and ≈ 25 dB achieved by the conventional OFDM-based systems. The SNR gains obtained with CE-OFDM and 16-QAM increased with the adoption of higher guard bands, suggesting that the CE-OFDM modulation format and parameters optimization via algorithms are promising in power and spectral-efficient VLC systems.

Optimization and artificial intelligence procedures were proposed aiming at simultaneously increasing the power and spectral efficiency of visible light communication systems in an Industry 4.0 environment. Two Case Studies for one and two-dimensional robotic movements were used and the Hybrid Multi-Objective Optimization (HMO) using a combination of the non-sorting genetic algorithm III and the Grey Wolf optimizer was proposed to minimize the signal's transmitted power and the guard band while constraining the error vector magnitude (EVM) metric. Thereafter, the optimal solutions were applied to a long-short-term memory neural network in order to forecast the future link parameters (Case Study I - CS1) and channel gain (Case Study II - CS2).

Results show that the HMO solutions provided a reduction of power consumption of up to ≈ 80 % for CS1 and ≈ 84.6 % for CS2, as compared to the non-optimized reference power and a minimized guard-band of up to ≈ 20 % and ≈ 10 % of the bandwidth for CS1 and CS2,

respectively, as compared to the fixed parameters case, for the evaluated link. The optimal parameters were experimentally tested for the CS1 and the EVM comparison validated both the proposed optimization, as well as the developed digital twin model. In CS1, the success of the proposed LSTM in forecasting the optimal parameters was expressed by the low RMSE error, under $7\ \%$ with no overfitting. Whereas, in CS2, the LSTM results show that the RNN architecture can be much simpler if the objective is to predict the channel gain of the future robot's position. Simulation results show that the RMSE obtained after testing of the proposed LSTM architecture was approximately $0.5\ \%$.

Moreover, the employment of CNN for channel equalization in an OFDM-based VLC system was investigated. The presented framework used CNN to the comb-type pilot arrangement channel equalization, suppressing the need for channel estimation, interpolation, and element-wise division of an OFDM scheme. The reported results show that the equalization scheme based on CNN outperforms the OFDM systems with equalization based on least square estimation for scenarios of low SNR, regardless of the nonlinearity of the VLC systems. And based on this finding, for dimerized VLC systems that require a reduction in the LED power signal (low SNR), the proposed AI-based equalization scheme is a suitable solution. In a second approach, a realistic model extracted from a real SISO VLC system is utilized for the dataset generation. The frequency response was determined by frequency scan, network analyzer, and estimation from OFDM training signals. The LED's nonlinearity was also contemplated and the CNN-DE was capable of equalizing the OFDM symbols without any other computations. The achieved CNN-DE and the LS-based equalization results are similar, and in terms of EVM, the CNN-DE outperforms the LS method for SNR > 15 dB. We also investigated the activation functions of the CNN-DE, and the results for both EVM and BER show that the performances are comparable.

6.2. Future Work

The developed applications of artificial intelligence in VLC systems can be extended and the following topics are planned as future work:

- conduct experiments to validate the presented optimization methodology and extend the contributions (Appendix A). Include the non-line-of-sight VLC channels in the OFDM and CE-OFDM SISO optimization;
- develop and apply these methods for determining parameters and forecasting trajectories with AI, envisioning power and spectral efficiency, in a VLC Multiple-Input Single-Output (MISO) (Appendix B) and MIMO systems;
- present GWO modified in clusters in order to make the optimization algorithm faster than the traditional algorithm and to deal with local minimum (Appendix C);
- employ the CNN equalization envisioning spectral efficiency with the minimization of

the number of used pilots. The application of CNN-DE in an adaptive modulation OFDM scheme is also planned to be studied. In addition, the analysis of the optimal parameters (the minimization of parameters number, the structure) will also be taken into consideration;

- development and analysis of the CNN direct equalizer for higher modulation order and different neural network architectures should be tested for complexity reduction. It is also intended to explore the application of CNN-DE method in MIMO-OFDM systems.

References

[1] Y. S. Cho, J. Kim, W. Y. Yang, and C. G. Kang, *MIMO-OFDM wireless communications with MATLAB*. John Wiley & Sons, 2010. [Cited on pages xv, 15, and 18]

[2] K. Deb, A. Pratap, S. Agarwal, and T. Meyarivan, "A fast and elitist multiobjective genetic algorithm: NSGA-II," *IEEE transactions on evolutionary computation*, vol. 6, no. 2, pp. 182–197, 2002. [Cited on pages xv, xxiii, 28, 29, and 45]

[3] W. Costa, H. Camporez, M. Pontes, M. Segatto, H. Rocha, J. Silva, M. Hinrichs, A. Paraskevopoulos, V. Jungnickel, and R. Freund, "Increasing the LED Bias Point of an OFDM-based VLC System through Multi-objective Optimization," in *2021 SBMO/IEEE MTT-S International Microwave and Optoelectronics Conference (IMOC)*, 2021, pp. 1–3. [Cited on pages xvi, xxi, 44, 46, 47, and 48]

[4] K. Deb and H. Jain, "An evolutionary many-objective optimization algorithm using reference-point-based nondominated sorting approach, part I: solving problems with box constraints," *IEEE transactions on evolutionary computation*, vol. 18, no. 4, pp. 577–601, 2013. [Cited on pages xxiii, 29, 30, and 60]

[5] H. Haas, L. Yin, Y. Wang, and C. Chen, "What is LiFi?" *Journal of Lightwave Technology*, vol. 34, no. 6, pp. 1533–1544, 2016. [Cited on page 1]

[6] Z. Ghassemlooy, W. Popoola, and S. Rajbhandari, *Optical wireless communications: system and channel modelling with Matlab®*. CRC press, 2019. [Cited on pages 1, 11, 12, and 14]

[7] A. Paraskevopoulos, J. Vučić, S. Voß, R. Swoboda, and K. Langer, "Optical wireless communication systems in the Mb/s to Gb/s range, suitable for industrial applications," *IEEE/ASME Transactions on Mechatronics*, vol. 15, no. 4, pp. 541–547, 2010. [Cited on page 1]

[8] S. Rajagopal, R. D. Roberts, and S.-K. Lim, "IEEE 802.15. 7 visible light communication: modulation schemes and dimming support," *IEEE Communications Magazine*, vol. 50, no. 3, 2012. [Cited on page 1]

[9] N. Consulting, U. S. D. of Energy. Office of Energy Efficiency, and R. E. B. T. P. L. Research, *Energy savings potential of solid-state lighting in general illumination applications*. Lighting Research and Development, Building Technologies Program, Office of . . . , 2003. [Cited on page 1]

[10] V. Jungnickel, P. W. Berenguer, S. M. Mana, M. Hinrichs, S. M. Kouhini, K. L. Bober,

and C. Kottke, “LiFi for industrial wireless applications,” in *2020 Optical Fiber Communications Conference and Exhibition (OFC)*, 2020, pp. 1–3. [Cited on page 1]

[11] K. T. Swami and A. A. Moghe, “A review of lifi technology,” in *2020 5th IEEE International Conference on Recent Advances and Innovations in Engineering (ICRAIE)*. IEEE, 2020, pp. 1–5. [Cited on page 1]

[12] S. Habibi, M. Omidi, F. sadat Tabataba, and E. Yazdian, “An Overview: Orthogonal Frequency Division Multiplexing Techniques for Visible Light Communication Systems,” in *2022 4th West Asian Symposium on Optical and Millimeter-wave Wireless Communications (WASOWC)*, 2022, pp. 01–06. [Cited on page 1]

[13] H. Sari, G. Karam, and I. Jeanclaude, “Transmission techniques for digital terrestrial tv broadcasting,” *IEEE communications magazine*, vol. 33, no. 2, pp. 100–109, 1995. [Cited on page 1]

[14] J. Li, Z. Huang, X. Liu, and Y. Ji, “Hybrid time-frequency domain equalization for LED nonlinearity mitigation in OFDM-based VLC systems,” *Optics express*, vol. 23, no. 1, pp. 611–619, 2015. [Cited on page 1]

[15] F. T. Monteiro, W. S. Costa, J. L. Neves, D. M. Silva, H. R. Rocha, E. O. Salles, and J. A. Silva, “Experimental evaluation of pulse shaping based 5G multicarrier modulation formats in visible light communication systems,” *Optics Communications*, vol. 457, p. 124693, 2020. [Cited on page 1]

[16] A. M. Abdelhady, O. Amin, A. Chaaban, B. Shihada, and M.-S. Alouini, “Downlink resource allocation for dynamic TDMA-based VLC systems,” *IEEE Transactions on Wireless Communications*, vol. 18, no. 1, pp. 108–120, 2019. [Cited on page 1]

[17] M. Obeed, A. M. Salhab, M.-S. Alouini, and S. A. Zummo, “On optimizing VLC networks for downlink multi-user transmission: A survey,” *IEEE Communications Surveys Tutorials*, vol. 21, no. 3, pp. 2947–2976, 2019. [Cited on page 1]

[18] Z. Yu, R. J. Baxley, and G. T. Zhou, “Iterative Clipping for PAPR Reduction in Visible Light OFDM Communications,” in *2014 IEEE Military Communications Conference*, 2014, pp. 1681–1686. [Cited on pages 2 and 41]

[19] W. Hu and D. Lee, “PAPR Reduction for Visible Light Communication Systems Without Side Information,” *IEEE Photonics Journal*, vol. 9, no. 3, pp. 1–11, 2017. [Cited on pages 2 and 41]

[20] Z. Li and C. Zhang, “An improved fd-dfe structure for downlink vlc systems based on sc-fdma,” *IEEE Communications Letters*, vol. 22, no. 4, pp. 736–739, 2018. [Cited on pages 2 and 41]

[21] J. Silva, A. Cartaxo, and M. Segatto, “A PAPR reduction technique based on a constant envelope OFDM approach for fiber nonlinearity mitigation in optical direct-detection

systems," *Optical Communications and Networking, IEEE/OSA Journal of*, vol. 4, no. 4, pp. 296–303, April 2012. [Cited on pages 2, 25, and 41]

[22] R. B. Nunes, R. d. O. Helder, M. E. Segatto, and J. A. Silva, "Experimental validation of a constant-envelope OFDM system for optical direct-detection," *Optical Fiber Technology*, vol. 20, no. 3, pp. 303–307, 2014. [Cited on pages 2 and 41]

[23] H. R. de O. Rocha, V. O. C. Dias, E. d. V. Pereira, R. B. Nunes, M. E. V. Segatto, and J. A. L. Silva, "Increasing the spectral efficiency of DDO-CE-OFDM systems by multi-objective optimization," *Journal of Lightwave Technology*, vol. 37, no. 9, pp. 2155–2162, 2019. [Cited on pages 2, 41, and 59]

[24] K. M. vd Zwaag, J. L. C. Neves, H. R. O. Rocha, M. E. V. Segatto, and J. A. L. Silva, "Increasing vlc nonlinearity tolerance by ce-ofdm," in *Latin America Optics and Photonics Conference*. Optica Publishing Group, 2018, p. W3D.3. [Cited on pages 2 and 41]

[25] K. M. vd Zwaag, J. L. Neves, H. R. Rocha, M. E. Segatto, and J. A. Silva, "Adaptation to the LEDs flicker requirement in visible light communication systems through CE-OFDM signals," *Optics Communications*, vol. 441, pp. 14–20, 2019. [Cited on pages 2, 41, and 76]

[26] E. d. V. Pereira, R. d. O. Helder, R. B. Nunes, M. E. Segatto, and J. A. Silva, "Impact of optical power in the guard-band reduction of an optimized DDO-OFDM system," *Journal of Lightwave Technology*, vol. 33, no. 23, pp. 4717–4725, 2015. [Cited on pages 2, 41, and 47]

[27] R. d. O. R. Helder, T. M. de Almeida, M. E. Segatto, and J. A. Silva, "Mono-objective optimization for direct detection optical OFDM transmissions in short-range links," *Journal of Microwaves, Optoelectronics and Electromagnetic Applications (JMOe)*, vol. 12, pp. 113–i127, 2013. [Cited on pages 2 and 41]

[28] J. Wan, X. Li, H.-N. Dai, A. Kusiak, M. Martínez-García, and D. Li, "Artificial-intelligence-driven customized manufacturing factory: Key technologies, applications, and challenges," *Proceedings of the IEEE*, vol. 109, no. 4, pp. 377–398, 2021. [Cited on page 2]

[29] R.-J. Essiambre, G. Kramer, P. J. Winzer, G. J. Foschini, and B. Goebel, "Capacity limits of optical fiber networks," *Journal of Lightwave Technology*, vol. 28, no. 4, pp. 662–701, 2010. [Cited on page 2]

[30] L. Gong, X. Zhou, W. Lu, and Z. Zhu, "A two-population based evolutionary approach for optimizing routing, modulation and spectrum assignments (rmsa) in o-ofdm networks," *IEEE Communications Letters*, vol. 16, no. 9, pp. 1520–1523, 2012. [Cited on page 2]

[31] E. d. V. Pereira, H. R. d. O. Rocha, R. B. Nunes, M. E. V. Segatto, and J. A. L. Silva, "Impact of optical power in the guard-band reduction of an optimized DDO-OFDM sys-

tem," *Journal of Lightwave Technology*, vol. 33, no. 23, pp. 4717–4725, 2015. [Cited on pages 2, 42, and 68]

[32] T. Freckmann, R.-J. Essiambre, P. J. Winzer, G. J. Foschini, and G. Kramer, "Fiber capacity limits with optimized ring constellations," *IEEE Photonics Technology Letters*, vol. 21, no. 20, pp. 1496–1498, 2009. [Cited on page 2]

[33] T. Lagkas, D. Klonidis, P. Sarigiannidis, and I. Tomkos, "Optimized joint allocation of radio, optical, and MEC resources for the 5G and beyond fronthaul," *IEEE Transactions on Network and Service Management*, vol. 18, no. 4, pp. 4639–4653, 2021. [Cited on page 2]

[34] E. Bjornson and P. Giselsson, "Two applications of deep learning in the physical layer of communication systems [lecture notes]," *IEEE Signal Processing Magazine*, vol. 37, no. 5, pp. 134–140, 2020. [Cited on page 2]

[35] H. R. de O. Rocha, C. E. S. Castellani, M. E. V. Segatto, and J. A. L. Silva, "Reducing the time of C+L band Raman amplifiers design with an algorithm based on artificial intelligence," *Optical Engineering*, vol. 59, no. 7, pp. 1 – 14, 2020. [Cited on page 2]

[36] O. Sidelnikov, A. Redyuk, S. Sygletos, M. Fedoruk, and S. Turitsyn, "Advanced convolutional neural networks for nonlinearity mitigation in long-haul WDM transmission systems," *Journal of Lightwave Technology*, vol. 39, no. 8, pp. 2397–2406, 2021. [Cited on page 2]

[37] W. S. Costa, J. L. Samatelo, H. R. Rocha, M. E. Segatto, and J. A. Silva, "Direct equalization with convolutional neural networks in ofdm based VLC systems," in *2019 IEEE Latin-American Conference on Communications*, 2019, pp. 1–6. [Cited on page 2]

[38] Y. Li, T. Geng, R. Tian, and S. Gao, "Machine-learning based equalizers for mitigating the interference in asynchronous MIMO OWC systems," *Journal of Lightwave Technology*, vol. 39, no. 9, pp. 2800–2808, 2021. [Cited on pages 2 and 3]

[39] B. Lin, Q. Lai, Z. Ghassemlooy, and X. Tang, "A machine learning based signal demodulator in NOMA-VLC," *Journal of Lightwave Technology*, vol. 39, no. 10, pp. 3081–3087, 2021. [Cited on pages 2, 3, and 53]

[40] N. Chi, J. Jia, F. Hu, Y. Zhao, and P. Zou, "Challenges and prospects of machine learning in visible light communication," *Journal of Communications and Information Networks*, vol. 5, no. 3, pp. 302–309, 2020. [Cited on pages 3 and 53]

[41] Z. Wang, Q. Wang, W. Huang, and Z. Xu, *Visible light communications: modulation and signal processing*. John Wiley & Sons, 2017. [Cited on pages 9, 13, and 14]

[42] P. A. Hoeher, *Visible light communications: theoretical and practical foundations*. Carl Hanser Verlag GmbH Co KG, 2019. [Cited on page 9]

[43] A. G. Bell, W. Adams, W. Preece *et al.*, "Discussion on "the photophone and the conver-

sion of radiant energy into sound",," *Journal of the Society of Telegraph Engineers*, vol. 9, no. 34, pp. 375–383, 1880. [Cited on page 10]

[44] F. R. Gfeller and U. Bapst, "Wireless in-house data communication via diffuse infrared radiation," *Proceedings of the IEEE*, vol. 67, no. 11, pp. 1474–1486, 1979. [Cited on page 10]

[45] G. Pang, T. Kwan, C.-H. Chan, and H. Liu, "LED traffic light as a communications device," in *Proceedings 199 IEEE/IEEJ/JSAI International Conference on Intelligent Transportation Systems (Cat. No. 99TH8383)*. IEEE, 1999, pp. 788–793. [Cited on page 10]

[46] T. Komine and M. Nakagawa, "Fundamental analysis for visible-light communication system using LED lights," *IEEE transactions on Consumer Electronics*, vol. 50, no. 1, pp. 100–107, 2004. [Cited on pages 10 and 56]

[47] T. Komine, S. Haruyama, and M. Nakagawa, "A study of shadowing on indoor visible-light wireless communication utilizing plural white led lightings," *Wireless Personal Communications*, vol. 34, no. 1, pp. 211–225, 2005. [Cited on pages 10, 13, and 56]

[48] T. Komine and M. Nakagawa, "Integrated system of white led visible-light communication and power-line communication," *IEEE Transactions on Consumer Electronics*, vol. 49, no. 1, pp. 71–79, 2003. [Cited on page 10]

[49] H. Sugiyama, S. Haruyama, and M. Nakagawa, "Brightness control methods for illumination and visible-light communication systems," in *2007 Third International Conference on Wireless and Mobile Communications (ICWMC'07)*. IEEE, 2007, pp. 78–78. [Cited on page 10]

[50] M. Yoshino, S. Haruyama, and M. Nakagawa, "High-accuracy positioning system using visible led lights and image sensor," in *2008 IEEE Radio and Wireless Symposium*. IEEE, 2008, pp. 439–442. [Cited on page 10]

[51] J. M. Kahn and J. R. Barry, "Wireless infrared communications," *Proceedings of the IEEE*, vol. 85, no. 2, pp. 265–298, 1997. [Cited on pages 10 and 14]

[52] H. Le Minh, D. O'Brien, G. Faulkner, L. Zeng, K. Lee, D. Jung, Y. Oh, and E. T. Won, "100-mb/s nrz visible light communications using a post-equalized white led," *IEEE Photonics Technology Letters*, vol. 21, no. 15, pp. 1063–1065, 2009. [Cited on page 10]

[53] A. H. Azhar, T.-A. Tran, and D. O'Brien, "Demonstration of high-speed data transmission using mimo-ofdm visible light communications," in *2010 IEEE Globecom Workshops*. IEEE, 2010, pp. 1052–1056. [Cited on page 10]

[54] ——, "A gigabit/s indoor wireless transmission using mimo-ofdm visible-light communications," *IEEE photonics technology letters*, vol. 25, no. 2, pp. 171–174, 2012. [Cited on page 10]

[55] S. Dimitrov and H. Haas, "Information rate of ofdm-based optical wireless communication systems with nonlinear distortion," *Journal of Lightwave Technology*, vol. 31, no. 6, pp. 918–929, 2012. [Cited on page 11]

[56] W. Costa, H. Camporez, M. Pontes, M. Segatto, H. Rocha, J. Silva, M. Hinrichs, A. Paraskevopoulos, V. Jungnickel, and R. Freund, "Increasing the led bias point of an ofdm-based vlc system through multi-objective optimization," in *2021 SBMO/IEEE MTT-S International Microwave and Optoelectronics Conference (IMOC)*. IEEE, 2021, pp. 1–3. [Cited on pages 11 and 59]

[57] P. Lou, H. Zhang, X. Zhang, M. Yao, and Z. Xu, "Fundamental analysis for indoor visible light positioning system," in *2012 1st IEEE International Conference on Communications in China Workshops (ICCC)*. IEEE, 2012, pp. 59–63. [Cited on pages 13 and 56]

[58] M. Russell and G. L. Stuber, "Interchannel interference analysis of ofdm in a mobile environment," in *1995 IEEE 45th vehicular technology conference. Countdown to the Wireless Twenty-First Century*, vol. 2. IEEE, 1995, pp. 820–824. [Cited on page 14]

[59] B. Fahs, A. J. Chowdhury, and M. M. Hella, "A 12-m 2.5-gb/s lighting compatible integrated receiver for ook visible light communication links," *Journal of Lightwave Technology*, vol. 34, no. 16, pp. 3768–3775, 2016. [Cited on page 14]

[60] N. Fujimoto and H. Mochizuki, "477 mbit/s visible light transmission based on ook-nrz modulation using a single commercially available visible led and a practical led driver with a pre-emphasis circuit," in *National Fiber Optic Engineers Conference*. Optica Publishing Group, 2013, pp. JTh2A–73. [Cited on page 14]

[61] G.-H. Im and J. Werner, "Bandwidth-efficient digital transmission up to 155 mb/s over unshielded twisted pair wiring," in *Proceedings of ICC'93-IEEE International Conference on Communications*, vol. 3. IEEE, 1993, pp. 1797–1803. [Cited on page 14]

[62] T. Jiang, D. Chen, C. Ni, and D. Qu, *OQAM/FBMC for future wireless communications: principles, technologies and applications*. Academic Press, 2017. [Cited on page 15]

[63] Y. G. Li and G. L. Stuber, *Orthogonal frequency division multiplexing for wireless communications*. Springer Science & Business Media, 2006. [Cited on page 15]

[64] R. W. Chang, "Synthesis of band-limited orthogonal signals for multichannel data transmission," *Bell system technical journal*, vol. 45, no. 10, pp. 1775–1796, 1966. [Cited on page 15]

[65] W. Kabir, "Orthogonal Frequency Division Multiplexing (OFDM)," in *2008 China-Japan Joint Microwave Conference*, 2008, pp. 178–184. [Cited on page 15]

[66] A. Kumar and P. NandhaKumar, "OFDM system with cyclostationary feature detection spectrum sensing," *ICT Express*, vol. 5, no. 1, pp. 21–25, 2019. [Cited on page 15]

[67] A. A. Zaidi, R. Baldemair, V. Moles-Cases, N. He, K. Werner, and A. Cedergren, "OFDM numerology design for 5G new radio to support IoT, eMBB, and MBSFN," *IEEE Communications Standards Magazine*, vol. 2, no. 2, pp. 78–83, 2018. [Cited on page 15]

[68] S. Weinstein and P. Ebert, "Data transmission by frequency-division multiplexing using the discrete fourier transform," *IEEE transactions on Communication Technology*, vol. 19, no. 5, pp. 628–634, 1971. [Cited on page 16]

[69] H. Rohling, *OFDM: concepts for future communication systems*. Springer Science & Business Media, 2011. [Cited on page 18]

[70] W. Chen, L. Qi, and F. Yanjun, "An improved least square channel estimation algorithm for underwater acoustic OFDM systems," in *2010 2nd International Conference on Future Computer and Communication*, vol. 3. IEEE, 2010, pp. V3–577. [Cited on page 20]

[71] J.-J. Van De Beek, O. Edfors, M. Sandell, S. K. Wilson, and P. O. Borjesson, "On channel estimation in OFDM systems," in *1995 IEEE 45th Vehicular Technology Conference. Countdown to the Wireless Twenty-First Century*, vol. 2. IEEE, 1995, pp. 815–819. [Cited on pages 20 and 73]

[72] M. Zhang and Z. Zhang, "An optimum dc-biasing for dco-ofdm system," *IEEE Communications Letters*, vol. 18, no. 8, pp. 1351–1354, 2014. [Cited on page 21]

[73] A. A. Abdulkafi, M. Y. Alias, and Y. S. Hussein, "Performance analysis of dco-ofdm in vlc system," in *2015 IEEE 12th Malaysia International Conference on Communications (MICC)*. IEEE, 2015, pp. 163–168. [Cited on page 21]

[74] I. Stefan, H. Elgala, and H. Haas, "Study of dimming and led nonlinearity for aco-ofdm based vlc systems," in *2012 IEEE Wireless Communications and Networking Conference (WCNC)*. IEEE, 2012, pp. 990–994. [Cited on page 21]

[75] N. Fernando, Y. Hong, and E. Viterbo, "Flip-ofdm for unipolar communication systems," *IEEE Transactions on Communications*, vol. 60, no. 12, pp. 3726–3733, 2012. [Cited on page 21]

[76] S. C. J. Lee, S. Randel, F. Breyer, and A. M. Koonen, "Pam-dmt for intensity-modulated and direct-detection optical communication systems," *IEEE Photonics Technology Letters*, vol. 21, no. 23, pp. 1749–1751, 2009. [Cited on page 21]

[77] F. Yang, Y. Sun, and J. Gao, "Adaptive laco-ofdm with variable layer for visible light communication," *IEEE Photonics Journal*, vol. 9, no. 6, pp. 1–8, 2017. [Cited on page 21]

[78] B. P. Lathi, *Modern digital and analog communication systems*. Oxford University Press, Inc., 1995. [Cited on page 22]

[79] R. A. Shafik, M. S. Rahman, A. R. Islam, and N. S. Ashraf, "On the error vector magnitude as a performance metric and comparative analysis," in *2006 International Con-*

ference on Emerging Technologies. IEEE, 2006, pp. 27–31. [Cited on pages 22, 23, and 45]

[80] Z. Yu, R. J. Baxley, and G. T. Zhou, "EVM and achievable data rate analysis of clipped OFDM signals in visible light communication," *EURASIP Journal on Wireless Communications and Networking*, vol. 2012, no. 1, p. 321, 2012. [Cited on page 22]

[81] T. Jiang and Y. Wu, "An overview: Peak-to-average power ratio reduction techniques for ofdm signals," *IEEE Transactions on broadcasting*, vol. 54, no. 2, pp. 257–268, 2008. [Cited on page 23]

[82] Y. A. Jawhar, L. Audah, M. A. Taher, K. N. Ramli, N. S. M. Shah, M. Musa, and M. S. Ahmed, "A review of partial transmit sequence for papr reduction in the ofdm systems," *IEEE Access*, vol. 7, pp. 18 021–18 041, 2019. [Cited on page 23]

[83] X. Li and L. J. Cimini, "Effects of clipping and filtering on the performance of ofdm," in *1997 IEEE 47th Vehicular Technology Conference. Technology in Motion*, vol. 3. IEEE, 1997, pp. 1634–1638. [Cited on page 24]

[84] S. C. Thompson, A. U. Ahmed, J. G. Proakis, J. R. Zeidler, and M. J. Geile, "Constant Envelope OFDM," *IEEE Transactions on Communications*, vol. 56, no. 8, pp. 1300–1312, August 2008. [Cited on pages 24 and 25]

[85] C. Santos, V. Oliari, H. Rocha, M. Pontes, M. Segatto, C. Okonkwo, A. Alvarado, and J. Silva, "Experimental demonstration of constant-envelope ofdm to reduce intermodulation impairments and increase robustness against fiber nonlinearities," *Journal of Lightwave Technology*, vol. 40, no. 15, pp. 4983–4989, 2022. [Cited on page 25]

[86] Z. Zhongyi and T. Zhaosheng, "Modulation and demodulation technique of constant envelope ofdm," in *2014 Fourth International Conference on Instrumentation and Measurement, Computer, Communication and Control*. IEEE, 2014, pp. 156–160. [Cited on page 25]

[87] Y. Collette and P. Siarry, *Multiobjective optimization: principles and case studies*. Springer Science & Business Media, 2004. [Cited on page 25]

[88] X.-S. Yang, "Metaheuristic optimization: Nature-inspired algorithms and applications," in *Artificial intelligence, evolutionary computing and metaheuristics*. Springer, 2013, pp. 405–420. [Cited on page 26]

[89] S. Mirjalili, J. S. Dong, and A. Lewis, "Nature-inspired optimizers," *Cham, Switzerland: Springer*, pp. 69–85, 2020. [Cited on page 26]

[90] D. Simon, *Evolutionary optimization algorithms*. John Wiley & Sons, 2013. [Cited on page 26]

[91] K. Miettinen, *Nonlinear multiobjective optimization*. Springer Science & Business Media, 2012, vol. 12. [Cited on page 27]

[92] B. Xin, L. Chen, J. Chen, H. Ishibuchi, K. Hirota, and B. Liu, "Interactive multiobjective optimization: A review of the state-of-the-art," *IEEE Access*, vol. 6, pp. 41 256–41 279, 2018. [Cited on page 27]

[93] A. Lambora, K. Gupta, and K. Chopra, "Genetic Algorithm - A Literature Review," in *2019 International Conference on Machine Learning, Big Data, Cloud and Parallel Computing (COMITCon)*, 2019, pp. 380–384. [Cited on page 27]

[94] A. Shukla, H. M. Pandey, and D. Mehrotra, "Comparative review of selection techniques in genetic algorithm," in *2015 international conference on futuristic trends on computational analysis and knowledge management (ABLAZE)*. IEEE, 2015, pp. 515–519. [Cited on page 27]

[95] A. Hassanat, K. Almohammadi, E. Alkafaween, E. Abunawas, A. Hammouri, and V. S. Prasath, "Choosing mutation and crossover ratios for genetic algorithms—a review with a new dynamic approach," *Information*, vol. 10, no. 12, p. 390, 2019. [Cited on page 27]

[96] N. Srinivas and K. Deb, "Multiobjective Optimization using Nondominated Sorting in Genetic Algorithms," *Evolutionary Computation*, vol. 2, no. 3, pp. 221–248, 1994. [Cited on page 28]

[97] D. E. Goldberg and K. Deb, "A comparative analysis of selection schemes used in genetic algorithms," in *Foundations of genetic algorithms*. Elsevier, 1991, vol. 1, pp. 69–93. [Cited on page 28]

[98] S. Verma, M. Pant, and V. Snasel, "A comprehensive review on NSGA-II for multi-objective combinatorial optimization problems," *IEEE Access*, vol. 9, pp. 57 757–57 791, 2021. [Cited on page 28]

[99] H. Jain and K. Deb, "An evolutionary many-objective optimization algorithm using reference-point based nondominated sorting approach, part ii: Handling constraints and extending to an adaptive approach," *IEEE Transactions on evolutionary computation*, vol. 18, no. 4, pp. 602–622, 2013. [Cited on page 29]

[100] S. Mirjalili, S. Saremi, S. M. Mirjalili, and L. d. S. Coelho, "Multi-objective grey wolf optimizer: a novel algorithm for multi-criterion optimization," *Expert Systems with Applications*, vol. 47, pp. 106–119, 2016. [Cited on pages 29, 31, and 60]

[101] C. A. C. Coello, G. T. Pulido, and M. S. Lechuga, "Handling multiple objectives with particle swarm optimization," *IEEE Transactions on evolutionary computation*, vol. 8, no. 3, pp. 256–279, 2004. [Cited on page 31]

[102] M. Premkumar, P. Jangir, B. S. Kumar, M. A. Alqudah, and K. S. Nisar, "Multi-objective grey wolf optimization algorithm for solving real-world bldc motor design problem," *Comput. Mater. Contin*, vol. 70, pp. 2435–2452, 2022. [Cited on page 31]

[103] N. Aloysius and M. Geetha, "A review on deep convolutional neural networks," in *2017*

International Conference on Communication and Signal Processing (ICCSP). IEEE, 2017, pp. 0588–0592. [Cited on page 33]

[104] S. Kiranyaz, T. Ince, O. Abdeljaber, O. Avci, and M. Gabbouj, "1-d convolutional neural networks for signal processing applications," in *ICASSP 2019-2019 IEEE International Conference on Acoustics, Speech and Signal Processing (ICASSP)*. IEEE, 2019, pp. 8360–8364. [Cited on page 34]

[105] S. Kiranyaz, O. Avci, O. Abdeljaber, T. Ince, M. Gabbouj, and D. J. Inman, "1d convolutional neural networks and applications: A survey," *Mechanical systems and signal processing*, vol. 151, p. 107398, 2021. [Cited on page 34]

[106] J. Han and C. Moraga, "The influence of the sigmoid function parameters on the speed of backpropagation learning," in *From Natural to Artificial Neural Computation: International Workshop on Artificial Neural Networks Malaga-Torremolinos, Spain, June 7–9, 1995 Proceedings 3*. Springer, 1995, pp. 195–201. [Cited on page 35]

[107] I. Goodfellow, Y. Bengio, and A. Courville, *Deep learning*. MIT press, 2016. [Cited on pages 35, 36, 74, and 75]

[108] H. Gholamalinezhad and H. Khosravi, "Pooling methods in deep neural networks, a review," *arXiv preprint arXiv:2009.07485*, 2020. [Cited on page 36]

[109] K. O'Shea and R. Nash, "An introduction to convolutional neural networks," *arXiv preprint arXiv:1511.08458*, 2015. [Cited on page 36]

[110] B. Gao and L. Pavel, "On the properties of the softmax function with application in game theory and reinforcement learning," *arXiv preprint arXiv:1704.00805*, 2017. [Cited on page 37]

[111] S. Hochreiter and J. Schmidhuber, "Long short-term memory," *Neural computation*, vol. 9, no. 8, pp. 1735–1780, 1997. [Cited on page 38]

[112] Y. Yu, X. Si, C. Hu, and J. Zhang, "A review of recurrent neural networks: Lstm cells and network architectures," *Neural computation*, vol. 31, no. 7, pp. 1235–1270, 2019. [Cited on page 38]

[113] F. A. Gers, J. Schmidhuber, and F. Cummins, "Learning to forget: Continual prediction with lstm," *Neural computation*, vol. 12, no. 10, pp. 2451–2471, 2000. [Cited on page 38]

[114] W.-R. Peng, X. Wu, V. R. Arbab, K.-M. Feng, B. Shamee, L. C. Christen, J.-Y. Yang, A. E. Willner, and S. Chi, "Theoretical and experimental investigations of direct-detected rf-tone-assisted optical ofdm systems," *Journal of Lightwave Technology*, vol. 27, no. 10, pp. 1332–1339, 2009. [Cited on page 42]

[115] LumiLeds, "LUXEON Rebel ES - Datasheet," https://www.lumileds.com/uploads/17/DS61-pdf, 2021, [Online; accessed 18-November-2022]. [Cited on pages 44, 54, and 59]

[116] E. Balashov, D. Pasquet, A. Korotkov, E. Bourdel, and F. Giannini, "Automatization of

compression point 1db (cp1db) and input 3rd order intercept point (iip3) measurements using lab view platform," in *International Symposium on Signals, Circuits and Systems, 2005. ISSCS 2005.*, vol. 1. IEEE, 2005, pp. 195–198. [Cited on page 44]

[117] C. Zhao and R. J. Baxley, "Error vector magnitude analysis for OFDM systems," in *2006 Fortieth Asilomar Conference on Signals, Systems and Computers*. IEEE, 2006, pp. 1830–1834. [Cited on page 45]

[118] Y. Hua, Z. Zhao, R. Li, X. Chen, Z. Liu, and H. Zhang, "Deep learning with long short-term memory for time series prediction," *IEEE Communications Magazine*, vol. 57, no. 6, pp. 114–119, 2019. [Cited on page 53]

[119] X. Zhao, Y. Chen, J. Guo, and D. Zhao, "A spatial-temporal attention model for human trajectory prediction," *IEEE/CAA Journal of Automatica Sinica*, vol. 7, no. 4, pp. 965–974, 2020. [Cited on page 53]

[120] Z.-Y. Wu, M. Ismail, E. Serpedin, and J. Wang, "Efficient prediction of link outage in mobile optical wireless communications," *IEEE Transactions on Wireless Communications*, vol. 20, no. 2, pp. 882–896, 2021. [Cited on page 53]

[121] M. Kottkamp, A. Pandey, D. Raddino, A. Roessler, R. Stuhlfauth, and R. und Schwarz, *5G New Radio: Fundamentals, Procedures, Testing Aspects*. Rohde & Schwarz GmbH & Company KG, 2019. [Cited on page 54]

[122] M. Hinrichs, B. Poddig, M. Nölle, P. Hellwig, R. Freund, and V. Jungnickel, "Efficient line coding for low-power optical wireless communications," in *2021 IEEE 94th Vehicular Technology Conference (VTC2021-Fall)*. IEEE, 2021, pp. 1–7. [Cited on pages 56, 105, 106, and 112]

[123] R. A. Shafik, M. S. Rahman, and A. R. Islam, "On the extended relationships among EVM, BER and SNR as performance metrics," in *2006 International Conference on Electrical and Computer Engineering*. IEEE, 2006, pp. 408–411. [Cited on pages 60 and 113]

[124] S. Patro and K. K. Sahu, "Normalization: A preprocessing stage," *arXiv preprint arXiv:1503.06462*, 2015. [Cited on page 62]

[125] A. Géron, *Hands-on machine learning with Scikit-Learn, Keras, and TensorFlow*. " O'Reilly Media, Inc.", 2022. [Cited on page 64]

[126] M. M. Bejani and M. Ghatee, "A systematic review on overfitting control in shallow and deep neural networks," *Artificial Intelligence Review*, pp. 1–48, 2021. [Cited on page 67]

[127] X. Zhang and Z. Yuan, "The application of interpolation algorithms in OFDM channel estimation," *Int. J. Simul. Syst. Sci. Technol*, vol. 17, pp. 11–1, 2016. [Cited on page 73]

[128] S. Coleri, M. Ergen, A. Puri, and A. Bahai, "Channel estimation techniques based on pilot arrangement in OFDM systems," *IEEE Transactions on broadcasting*, vol. 48, no. 3, pp.

223–229, 2002. [Cited on page 73]

[129] E. Balevi and J. G. Andrews, "Deep Learning-Based Channel Estimation for High-Dimensional Signals," *arXiv preprint arXiv:1904.09346*, 2019. [Cited on page 73]

[130] A. A. M. Picorone, T. R. Oliveira, and M. V. Ribeiro, "PLC channel estimation based on pilots signal for OFDM modulation: A review," *IEEE Latin America Transactions*, vol. 12, no. 4, pp. 580–589, 2014. [Cited on page 73]

[131] M. Soltani, V. Pourahmadi, A. Mirzaei, and H. Sheikhzadeh, "Deep Learning-Based Channel Estimation," *IEEE Communications Letters*, vol. 23, no. 4, pp. 652–655, 2019. [Cited on page 73]

[132] H. Ye, G. Y. Li, and B.-H. Juang, "Power of deep learning for channel estimation and signal detection in OFDM systems," *IEEE Wireless Communications Letters*, vol. 7, no. 1, pp. 114–117, 2017. [Cited on page 73]

[133] S. T. Ahmad and K. P. Kumar, "Radial basis function neural network nonlinear equalizer for 16-QAM coherent optical OFDM," *IEEE Photonics Technology Letters*, vol. 28, no. 22, pp. 2507–2510, 2016. [Cited on page 73]

[134] E. Giacoumidis, S. Le, I. Aldaya, J. Wei, M. McCarthy, N. Doran, and B. Eggleton, "Experimental comparison of artificial neural network and Volterra based nonlinear equalization for CO-OFDM," in *Optical Fiber Communication Conference*. Optical Society of America, 2016, pp. W3A–4. [Cited on page 73]

[135] H. Huang, J. Yang, H. Huang, Y. Song, and G. Gui, "Deep learning for super-resolution channel estimation and DOA estimation based massive MIMO system," *IEEE Transactions on Vehicular Technology*, vol. 67, no. 9, pp. 8549–8560, 2018. [Cited on page 73]

[136] R. Jiang, X. Wang, S. Cao, and J. Zhao, "Deep Neural Networks for Channel Estimation in Underwater Acoustic OFDM Systems," *IEEE Access*, vol. 7, pp. 23 579–23 594, 2019. [Cited on page 73]

[137] Y. Zhang, J. Li, Y. Zakharov, X. Li, and J. Li, "Deep learning based underwater acoustic OFDM communications," *Applied Acoustics*, vol. 154, pp. 53–58, 2019. [Online]. Available: https://linkinghub.elsevier.com/retrieve/pii/S0003682X18307400 [Cited on page 73]

[138] X. Wu, Z. Huang, and Y. Ji, "Deep neural network method for channel estimation in visible light communication," *Optics Communications*, vol. 462, p. 125272, 2020. [Cited on page 74]

[139] F. A. Aoudia and J. Hoydis, "End-to-end learning for OFDM: From neural receivers to pilotless communication," *IEEE Transactions on Wireless Communications*, 2021. [Cited on page 74]

[140] Z. C. Lipton, J. Berkowitz, and C. Elkan, "A critical review of recurrent neural networks

for sequence learning," *arXiv preprint arXiv:1506.00019*, 2015. [Cited on page 74]

[141] O. Bazgir, R. Zhang, S. R. Dhruba, R. Rahman, S. Ghosh, and R. Pal, "Representation of features as images with neighborhood dependencies for compatibility with convolutional neural networks," *Nature communications*, vol. 11, no. 1, pp. 1–13, 2020. [Cited on page 74]

[142] S. Ioffe and C. Szegedy, "Batch normalization: Accelerating deep network training by reducing internal covariate shift," *arXiv preprint arXiv:1502.03167*, 2015. [Cited on page 75]

[143] J. Nagi, F. Ducatelle, G. A. Di Caro, D. Cireşan, U. Meier, A. Giusti, F. Nagi, J. Schmidhuber, and L. M. Gambardella, "Max-pooling convolutional neural networks for vision-based hand gesture recognition," in *2011 IEEE international conference on signal and image processing applications (ICSIPA)*. IEEE, 2011, pp. 342–347. [Cited on page 75]

[144] D. P. Kingma and J. Ba, "Adam: A method for stochastic optimization," *arXiv preprint arXiv:1412.6980*, 2014. [Cited on page 77]

[145] C. Caruso and F. Quarta, "Interpolation methods comparison," *Computers & Mathematics with Applications*, vol. 35, no. 12, pp. 109–126, 1998. [Cited on page 78]

[146] K. M. V. D. Zwaag, M. P. Marinho, W. D. S. Costa, F. De Assis Souza Dos Santos, T. F. Bastos-Filho, H. R. O. Rocha, M. E. V. Segatto, and J. A. L. Silva, "A Manchester-OOK Visible Light Communication System for Patient Monitoring in Intensive Care Units," *IEEE Access*, vol. 9, pp. 104 217–104 226, 2021. [Cited on page 80]

[147] G. M. Foody, "Status of land cover classification accuracy assessment," *Remote sensing of environment*, vol. 80, no. 1, pp. 185–201, 2002. [Cited on page 82]

[148] R. Susmaga, "Confusion Matrix Visualization," in *Intelligent Information Processing and Web Mining*, M. A. Kłopotek, S. T. Wierzchoń, and K. Trojanowski, Eds. Berlin, Heidelberg: Springer Berlin Heidelberg, 2004, pp. 107–116. [Cited on page 82]

[149] P. Banelli, S. Buzzi, G. Colavolpe, A. Modenini, F. Rusek, and A. Ugolini, "Modulation formats and waveforms for 5g networks: Who will be the heir of ofdm?: An overview of alternative modulation schemes for improved spectral efficiency," *IEEE Signal Processing Magazine*, vol. 31, no. 6, pp. 80–93, 2014. [Cited on page 106]

[150] G. ITU-T, "975.1: Forward error correction for high bit-rate dwdm submarine systems," *Telecommunication Standardization Sector*, 2004. [Cited on page 107]

[151] M. Hinrichs, J. Hilt, V. Jungnickel, S.-K. Lim, I. S. Jang, J.-D. Jeong, and M. Noshad, "Pulsed modulation phy for power-efficient optical wireless communication," in *ICC 2019-2019 IEEE International Conference on Communications (ICC)*. IEEE, 2019, pp. 1–7. [Cited on page 109]

[152] W. Costa, H. Camporez, M. Hinrichs, H. Rocha, M. Pontes, M. Segatto,

A. Paraskevopoulos, V. Jungnickel, R. Freund, and J. Silva, "Toward ai-enhanced vlc systems for industrial applications," *Journal of Lightwave Technology*, 2022. [Cited on page 111]

[153] K. Jaiswal, H. Mittal, and S. Kukreja, "Randomized grey wolf optimizer (rgwo) with randomly weighted coefficients," in *2017 Tenth International Conference on Contemporary Computing (IC3)*. IEEE, 2017, pp. 1–3. [Cited on page 119]

[154] S. Gupta and K. Deep, "A memory-based grey wolf optimizer for global optimization tasks," *Applied Soft Computing*, vol. 93, p. 106367, 2020. [Cited on page 119]

[155] F. Yan, X. Xu, and J. Xu, "Grey wolf optimizer with a novel weighted distance for global optimization," *IEEE Access*, vol. 8, pp. 120 173–120 197, 2020. [Cited on page 119]

APPENDIX A.

An Experimental Investigation on Amplitude and Phase Modulated OFDM Using Lifi Technology

This Appendix presents the ongoing work on "An Experimental Investigation on Amplitude and Phase Modulated OFDM Using LiFi Technology".

A.1. Objectives

According to prior research, although having a spread on the spectrum hinders communication for some systems, CE-OFDM can handle nonlinearities better and also reduces the PAPR of OFDM systems. The purpose of this work is to conduct an experimental investigation on the use of conventional and constant envelope OFDM systems using LiFi technology in order to compare both maximum data rates achieved for 4, 16, and 32-QAM. In order to compare the two resilient multicarrier modulations, metrics including bit-error-rate (BER) and error vector magnitude (EVM) numbers are assessed in this work.

A.2. Methods

The experiment evaluated in this work considered the block diagrams of the modulations shown in Fig A.1. In order to analyze the BER, a Pseudorandom Binary Sequence (PRBS) of 1×10^6 bits were generated. For a fair comparison, we employed the same parameters of the baseband OFDM for both amplitude modulation (AM) and phase modulation (PM) as detailed in Table A.1. Considering the spread of the spectrum for CE-OFDM, $1/8 \times N_{\mathrm{FFT}}$ of the subcarriers were zeroed. The signal bandwidth was set to 25 and 50 MHz centered at $f_{\mathrm{c}} = 50$ MHz, considering a steep attenuation imposed by the frontend after 100 MHz [122]. The signal at the transmission side is up-converted to 400 MSps and normalized before being conveyed to the AWG. The data rate achieved for the OFDM for the framework developed is given by

$$R_{\mathrm{b-OFDM}} = \frac{N_{\mathrm{s}} \times \log_2(M)}{T_{\mathrm{sym}} + T_{\mathrm{CP}}} = \frac{N_{\mathrm{s}} \times \log_2(M) \times B_{\mathrm{W}}}{N_{\mathrm{u}} + N_{\mathrm{CP}}} \tag{A.1}$$

Moreover, the OFDM spectral efficiency can be determined by [149]

$$\mathrm{SE} = \frac{R_\mathrm{b}}{B_\mathrm{W,eff}} = \frac{N_\mathrm{s} \times \log_2(M)}{N_\mathrm{FFT} + N_\mathrm{CP}}, \tag{A.2}$$

where $B_\mathrm{W,eff}$ is the effective bandwidth occupied by the signal.

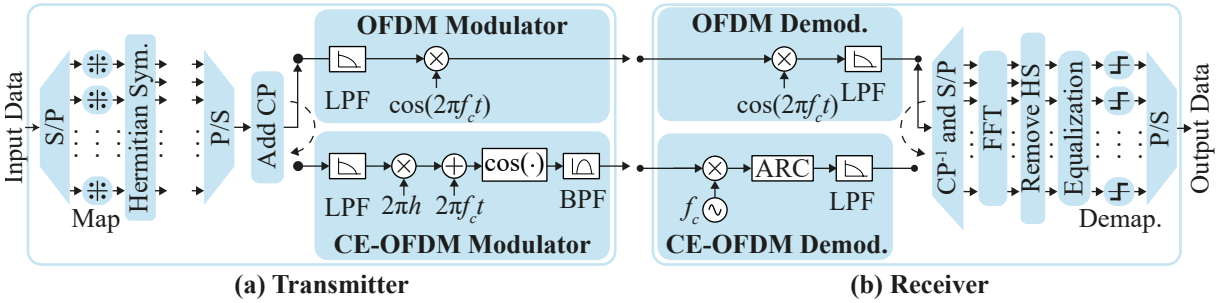

Figure A.1. Block diagram of the OFDM multicarrier modulations. (a) Conventional OFDM that modulates the baseband OFDM in amplitude. (b) CE-OFDM which is the baseband OFDM modulated in phase.

Table A.1. Parameters used in the conventional and constant-envelope OFDM schemes (see Fig. A.1).

Parameter	Symbol	Value
QAM mapping order	M	4, 16, and 32
FFT block size	N_FFT	128
Zeroed sub-carriers	N_z	1/8 $\times N_\mathrm{FFT}$
Cyclic prefix size	N_CP	6.25 %
Bandwidth (bandpass)	B_W	25 MHz
Oversampling factor	K	8
Carrier frequency	f_c	50 MHz

The analog signal was generated by a DN2.662-08 arbitrary waveform generator (AWG) with 16-bit resolution. We used the frontends developed by the researchers of the Fraunhofer Heinrich-Hertz-Institute, described and characterized in [122]. The signal acquisition was performed by a DN2.445-08 Spectrum digitizer, an Ethernet/LXI remote high-speed digitizer with 14/16 bit resolution. The signal is digitally converted to 500 MSps and synchronized by using cross-correlation with the transmitted signal. The signal was then demodulated and the output bit-stream was obtained.

Fig. A.2a illustrates the experimental configuration with the signal's modulation and demodulation (performed in Matlab) and the physical devices used. We considered for the experiments the receiver's longitudinal (Fig. A.2b) and lateral displacement (Fig. A.2c). For the longitudinal displacement, we varied the link distance from 50 cm to 500 cm in steps of 50 cm, and for the lateral direction of movement, the experiments were made in steps of 25 cm, from 0 to 125 cm, and 1 m longitudinally far at no lateral displacement (d = 0).

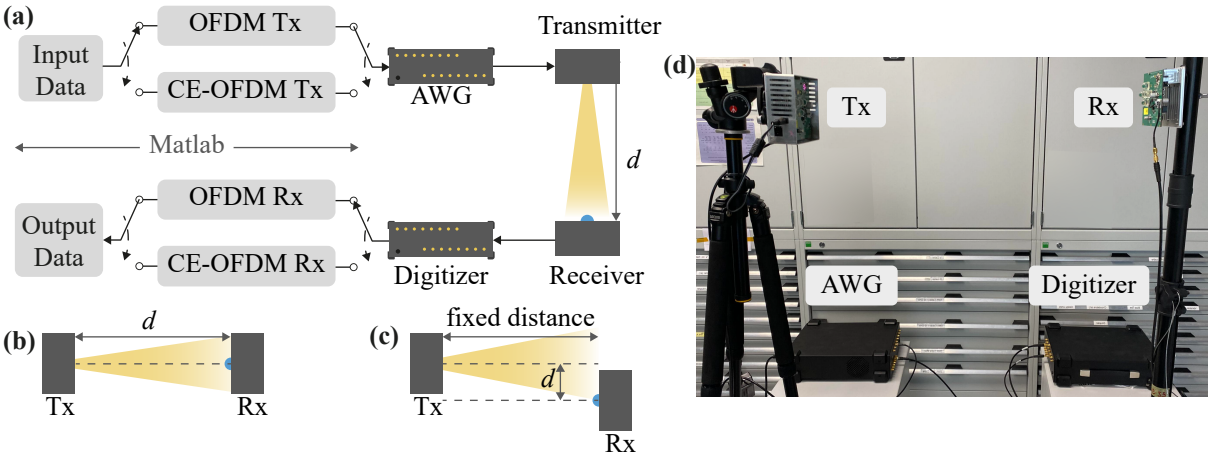

Figure A.2. Schematic of the experimental configuration. (a) OFDM and CE-OFDM experimental framework. Top view of the (b) longitudinal and (c) lateral link distance variation. (d) Photo of the Li-Fi setup.

The performance comparison of the modulations took into account the EVM and BER as figures of metrics to evaluate the system communication. The maximum data rate was also analyzed, for that we assumed the FEC-BER threshold determined as the BER $\approx 3.8 \times 10^{-3}$ [150] as a free-error condition.

A.3. Preliminary Results

In order to analyze the level of light power at the receiver as a function of the link distance, we employed the off-the-shelf high-power LEDs (ILS ILH-IO04-85NL) as the light source, operating at 850 nm. Considering the longitudinal (Fig. A.2b) and lateral (Fig. A.2c) displacement configurations already described.

In order to analyze the level of light power at the receiver as a function of the link distance, we employed the off-the-shelf high-power LEDs (ILS ILH-IO04-85NL) as the light source (already assembled in the transmitter frontend), operating at 850 nm. The power of the light was measured using a Thorlabs PM400 Optical Power Meter while accounting for lateral and longitudinal distance configurations (as illustrated in Fig A.2b and Fig. A.2c). Fig. A.3 shows the power of the optical signal as a function of the distance between the source and the power meter. The power of the signal decreases clearly in relation to the square of the distance, as determined by the channel gain modeling in (2.5).

For a bandwidth of 25 MHz, Fig. A.4a shows a clearly better performance in terms of EVM for CE-OFDM up to 400 m. Also for B_{W} =25 MHz, for all the mapping cardinalities the CE-OFDM outperforms OFDM, which demonstrates that the constant-envelope approach is more robust against the noise imposed by the photodetection, increasing the reach of the communication link. The performance of the communication tends to decline with larger bandwidths since the front end imposes a measured attenuation for frequencies beyond 75 MHz. As observed in

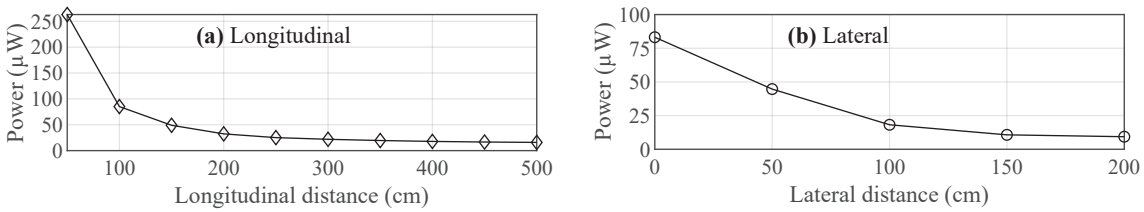

Figure A.3. Measured light power in dBm emitted by off-the-shelf high-power LEDs (ILS ILH-IO04-85NL) operating at 850nm. The measurements were performed using a ThorLabs PM400 Optical Power Meter.

Fig. A.4c, the EVM for $B_W = 50$ MHz presents a worse performance if compared with the performance of the $B_W = 25$ MHz. Regardless of the susceptibility to errors due to greater introduction of noise, Fig A.4d presents the same trend as observed in Fig. A.4a: the CE-OFDM tends to deal better with such conditions.

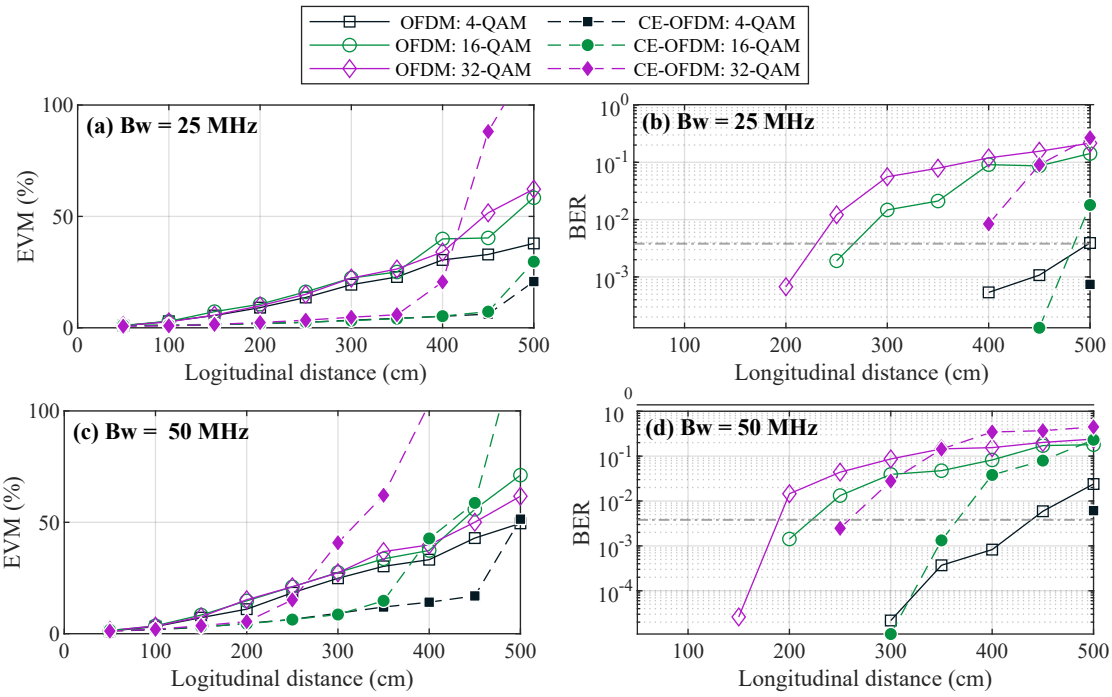

Figure A.4. Figure of metrics results for OFDM and CE-OFDM signal along with longitudinal displacement of the receiver. (a) BER and (b) EVM for bandwidth of 25 MHz. (c) BER and (d) EVM for a bandwidth of 50 MHz.

In order to validate the analysis of the longitudinal direction of the receiver movement, the lateral displacement of the receiver was also evaluated and the results are shown in Fig. A.5. As expected, the trends of the curves are similar to the ones observed in Fig. A.4, since the difference between the two configurations lies just in the attenuation of the light power as shown in Fig. A.3.

The maximum data rate achieved below the FEC-BER threshold (BER $= 1 \times 10^{-3}$ was also analyzed along the link distances. The maximum data rate achieved is depicted in Fig. A.6. As can be observed, the maximum data rates achieved by the conventional OFDM and constant-

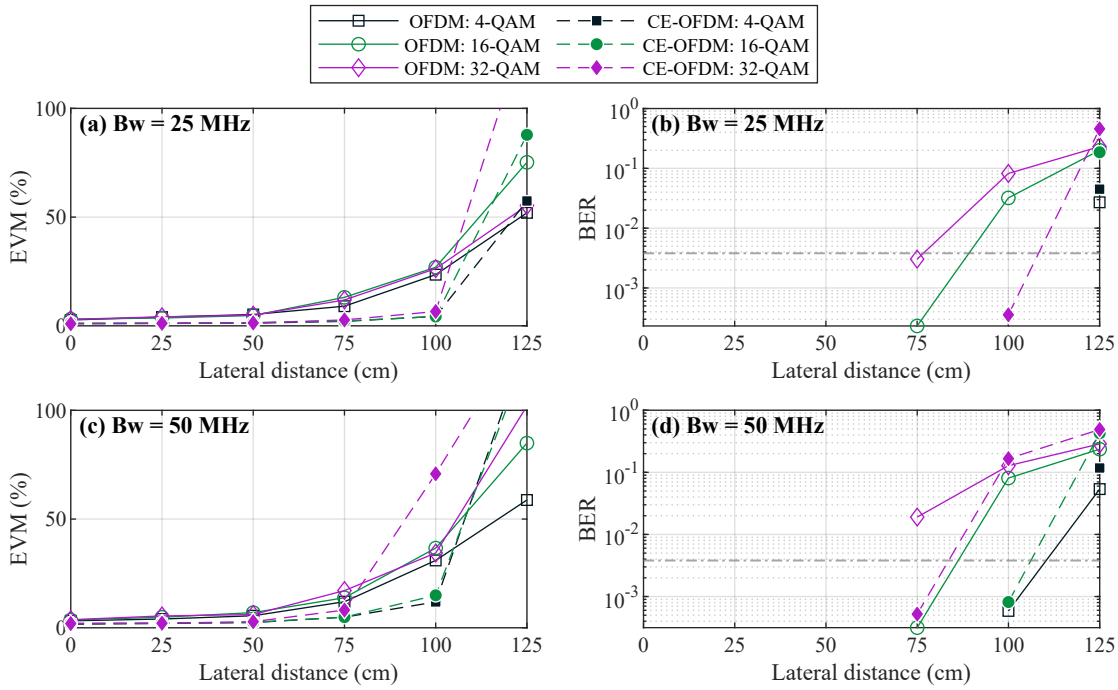

Figure A.5. Figure of metrics results for OFDM and CE-OFDM signal along with lateral displacement of the receiver. (a) BER and (b) EVM for bandwidth of 25 MHz. (c) BER and (d) EVM for a bandwidth of 50 MHz.

envelope OFDM are the same for lower distances. However, for longer link distances the CE-OFDM achieves higher data rates than the conventional OFDM for all the evaluated scenarios, considering the mapping levels of 4, 16, and 32-QAM. The numbers in parentheses next to the curves are the minimal BER for each cardinality that satisfies the FEC-BER threshold criterion.

Fig. A.7 depicts the spectral efficiency results achieved by the measurements. The calculation was performed using (A.2), and the data rate R_b is the maximum data rate was the highest data rate possible as depicted in Fig. A.6.

A.4. Next Steps

The following are the subsequent steps for this work:

- compare the proposed configuration setup's multicarrier modulations with a reliable modulation signal known as pulsed modulation PHY, in short PM-PHY [151];
- inform the scientific community about the findings.

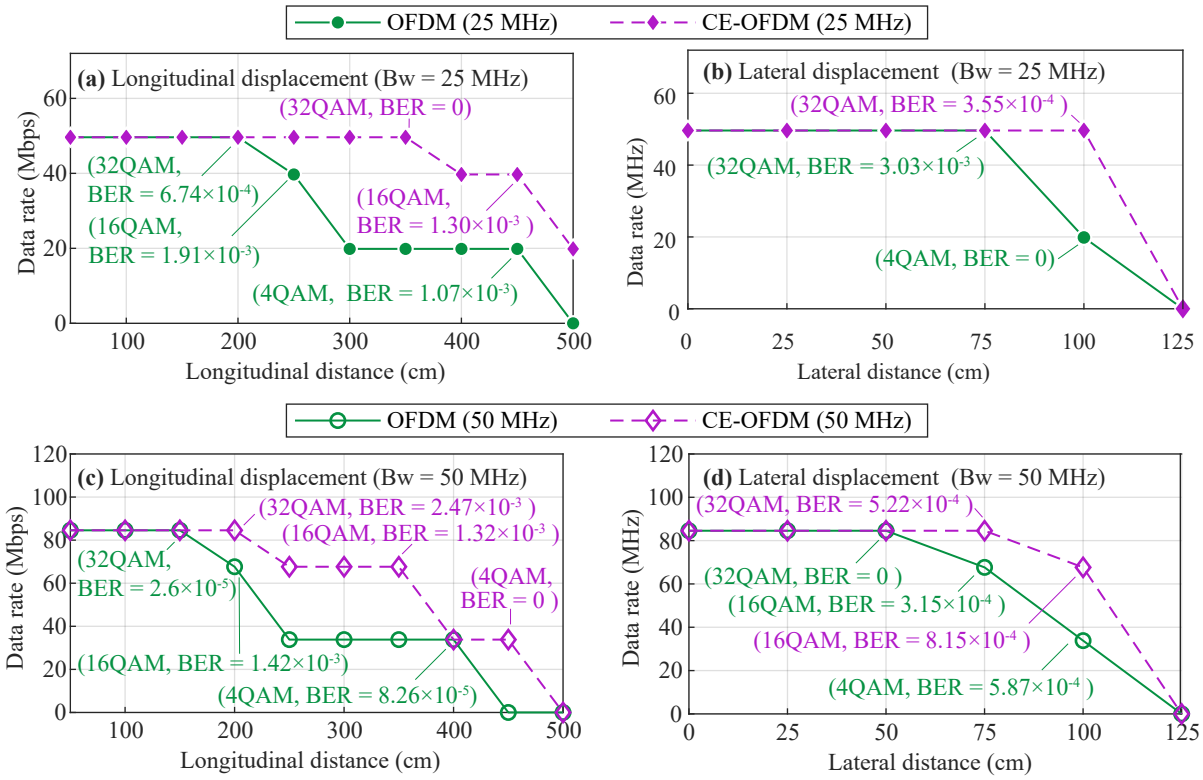

Figure A.6. The achievable data rate for signals with bandwidths of 25 and 50 MHz that are below the FEC limit (BER less than 3.8×10^{-3} when taking into account 4, 16, and 32-QAM mapping). The values in parenthesis indicate the lowest BER experimented below the FEC limit for the particular cardinality.

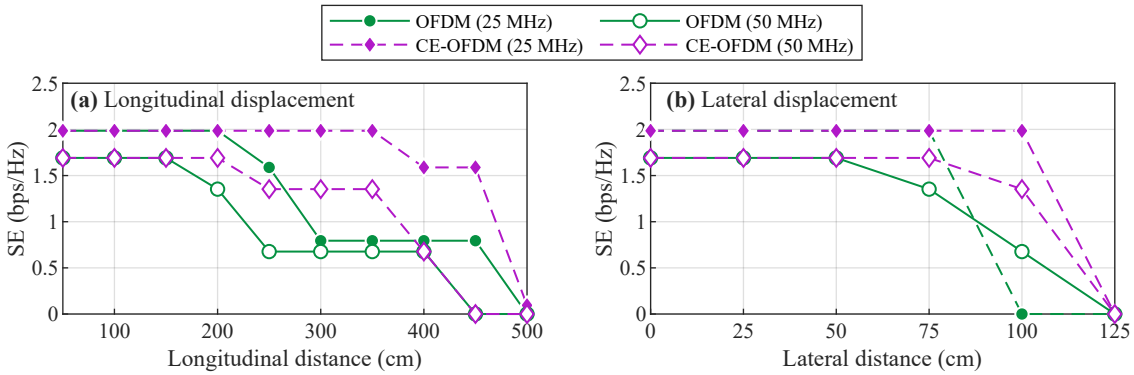

Figure A.7. Achievable spectral efficiency per modulation below the FEC limit (BER lower than limit 3.8×10^{-3}) for bandwidths of 25 and 50 MHz

APPENDIX B.

Enhancing Spectral and Power Efficiency in Multiple-Input Single-Output Visible Light Communication through Multi-Objective Optimization

This Appendix presents the ongoing work on "Enhancing Spectral and Power Efficiency in Multiple-Input Single-Output Visible Light Communication through Multi-Objective Optimization".

B.1. Objectives

The goal of the MISO system is to promote communication diversity. The settings for VLC systems can be determined to be static, however, this method may also be ineffective when only some communication channels are necessary. In order to improve the power and spectral efficiencies of the entire system, the primary goal of this work is to examine the applicability of metaheuristics in the process of determining the best VLC and multicarrier modulation parameters based on the position of the receiver. The work described in Chapter 4 is continued here while incorporating a MISO communication system.

B.2. Methods

The VLC MISO model developed in this work is presented in this section, together with the description of the problem formulation with the objectives and constraints that ought to be assessed. It is also presented how the NSGA-III and MOGWO are combined together by the hybrid multi-objective optimizer.

B.2.1. MISO Model for Visible Light Communication

In contrast to the work suggested in [152], this work aims to evaluate the application of optimization methods to ensure system performance (for BER lower than the FEC limit) and improve the power and spectral efficiency using a VLC-multiple-input single-output channel.

A VLC-MISO channel model was created with this in mind. The model is briefly explained here. The transmitter front end receives the electrical signal. The offset is eliminated at this stage, and the signal is amplified to an I_{RMS} level. The offset of the signal with a current of I_{bias} is applied immediately following the convolution with the $\mathrm{OFE_{TX}}$ impulse response because the transmitter OFE likewise has a DC frequency zeroed [122]. The reverse flow of current through the diode was ignored when modeling the static behavior of the LED, therefore no negative current is permitted in the diode. With the non-negative current, the electrical-optical conversion is performed through the so-called nonlinear LED model (NL LED model, for short). The output of this model is a signal in the optical domain, in Watts.

The optical signal is then sent through the channel and attenuated depending on the position of the receiver and transmitter (modeled as a convolution with the channel response). The sum operator, which depicts the superposition of each transmitter received signal's contribution, is used. The signal is virtually zero-clipped during the photodetection stage and is then converted into the electrical domain by the detector responsivity R, which in this technique is regarded as linear.

The frequency response of the receiver OFE is then considered, and the noise, as described in Chapter 4, is specified to be the same as for the prior SISO model ($\nu = -165$ dBm), is summed up with the signal. At last, the signal is amplified by a linear trans-impedance amplifier of gain G. The MISO-VLC model is depicted in Fig. B.1.

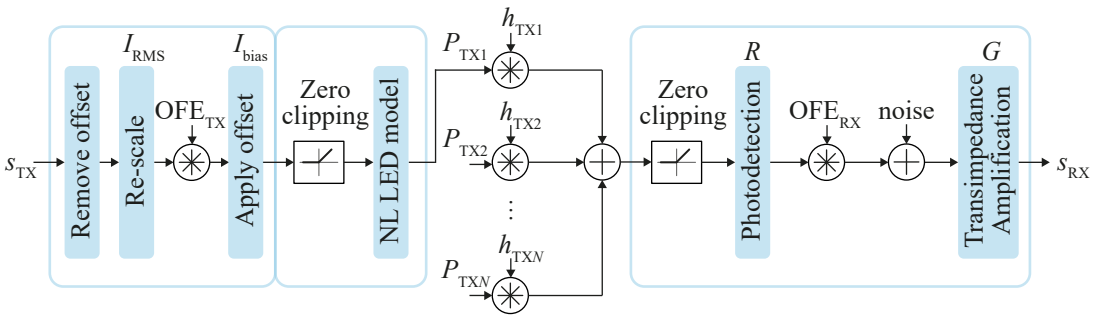

Figure B.1. Block diagram of the MISO-VLC model under evaluation. OFE: optical frontend.

The environment used in this Use Case for the generation of the MISO VLC channel is shown in Fig. B.2. The room is 7 m $\times$ 7 m $\times$ 4 m in size. The scenario considered in this work has one receiver front end and nine LED transmitter frontends mounted on the room's ceiling. An array of 27 $\times$ 27 receiver sites was produced, with equal spacing for both width and length of 25 cm, as it is useful to evaluate the optimum points and their relationship with the neighborhood of the optimal solution. With the receiver's height varying from 25 to 225 cm, in steps of 25 cm, the relationship of the best solutions taking the receiver's height into account is similarly interesting and was also developed for the channel generation. Table B.1 lists the VLC and scenario fixed parameters. The OFDM signals to be conveyed have fixed parameters as shown in Table B.2.

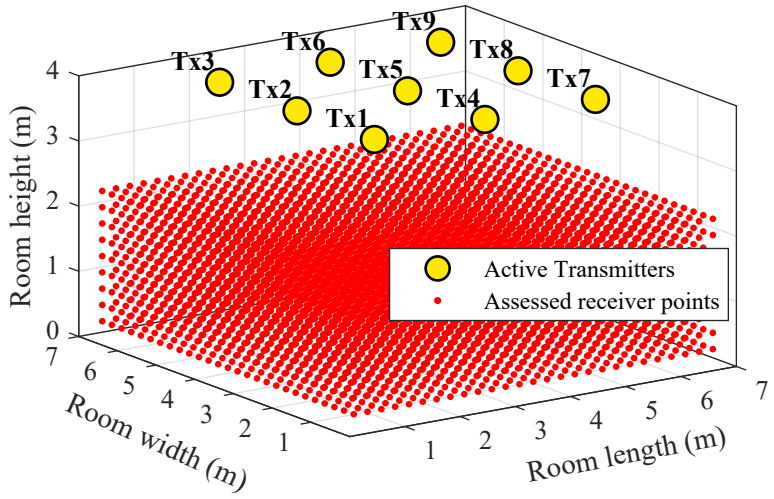

Figure B.2. Room scenario with the positions of the transmitter (yellow circles) and receiver (red dots) used as Use Case for the MISO optimization. The room's layout is outlined in Table B.1.

Table B.1. Parameters of the scenario.

	Parameter	**Value**
Room	Room size	7×7 m $\times$ 4 m
Emitter	Emitter height	4 m
	Semi-angle at half power	30°
	OFE_{TX} bandwidth	23 MHz
Receiver	Receiver height	0.25:0.25:2.25 m
	Effective photosensitive area	7 mm^2
	Field of view	45°
	Responsitivity	0.63 A/W
	OFE_{RX} bandwidth	23 MHz

B.2.2. Multi-objective Problem Formulation

Envisioning the optimization in which the objectives are to decrease the transmitters' overall power ($\min(P_{\text{T}})$) and increase the spectral efficiency ($\min(G_{\text{B}}/B_{\text{W}})$), constraints might be assumed. In summary, as presented in Chapter 4, this work's optimized features are the bias current, the RMS amplification current, and the guard band. We utilize the modulation current's RMS amplitude as it accurately reflects the average of the signal power. This decision allows for clipping of the signal at zero amplitude and takes into account the noise that it introduces. The RMS upper bound was assumed to be 1A. Here, an EVM restriction is also used, but instead of using the forward error correction (FEC) limit as a limit, an absolute EVM value is used instead. The goal of $\text{EVM} < -11$ dB translates to a BER of roughly 1×10^{-4} for an OFDM transmission using 4-QAM as subcarrier mapping in an AWGN channel [123], which was also validated and employed in this formulation problem. The parameters' boundaries of the optimizer for each transmitter i_{TX} of the MISO-VLC system are summarized in Table B.3.

Table B.2. Simulation Parameters.

Parameter	Symb.	Value
QAM mapping order	M	4
FFT block size	N_{FFT}	128
Data subcarriers	N_{s}	42
Cyclic prefix size	N_{CP}	16
Subcarrier spacing	Δ_{f}	15 kHz
Bandwidth	B_{W}	5 MHz
Oversampling factor	K	4

Table B.3. Problem formulation for the MISO power and spectral efficient optimization.

Min. P_{T} and **Min.** $\frac{G_{\mathrm{B}}}{B_{\mathrm{W}}}$
subject to:
$0.01 \leq I_{\mathrm{RMS},i_{\mathrm{TX}}} \leq 1$ A
$50 \leq I_{\mathrm{bias},i_{\mathrm{TX}}} \leq 2000$ mA
$0.001 \leq \frac{G_{\mathrm{B}}}{B_{\mathrm{W}}} \leq 1$
$\mathrm{EVM}_{\mathrm{sol}} < -11$ dB

Table B.3 shows that the number of optimization solutions, N_{sol}, tends to increase linearly as the number of transmitters, N_{TX}, assumed to have the optimal parameters assessed, increases. The guard band has a set solution that carries an identical value across all transmitters. The remaining solutions are the RMS and bias current values that are individually optimized for each emitter. As a result, N_{sol} refers to the number of solutions to this problem, given by

$$N_{\mathrm{sol}} = 2 \times N_{\mathrm{TX}} + 1. \tag{B.1}$$

The algorithm's time to output the answers increases as the number of solutions rises, which results in a higher computational cost when there are multiple transmitters per receiver point. With this in mind, we created a new restriction that corresponds to where the receiver front end is located in the space. It was empirically observed that for this scenario and configurations, the individual links with attenuation greater than 43 dB, the contributions of such transmitters, could be omitted, or the transmitter could be eliminated from the solution vector. This allowed us to develop a process that was less computationally demanding to determine the optimal parameters.

B.2.3. Hybrid-Multi-objective Optimizer and Knee-Point Selection

In this study, it is referred to as the hybrid multi-objective optimization (HMO), a heuristic that combines the multi-objective Grey Wolf optimizer (MOGWO) and the Non-Sorting Ge-

netic Algorithm III (NSGA-III), two well-known meta-heuristics, with the goal of increasing diversity. The Pareto fronts (F1s) for each receiver position are obtained from the two evaluated optimization algorithms working concurrently in the first stage of the HMO. The dominated solutions are then eliminated once the Pareto fronts have been combined. The Pareto front has separate objectives that are not dominated by one another, hence unbiased criteria for selecting the best answer were developed. The objectives are normalized, and the knee-point solution is determined and assumed to be the solution combination for a specified position with the least Euclidean distance from the origin. Both the Algorithm 4.1 and the Fig. 4.7 provide a full explanation of this technique. The parameters for the optimizer that compose the HMO are described in Table B.4.

Table B.4. Parameters of the HMO Optimizers.

NSGA-III

Parameter	**Value**
Population Size	30
Number of Iterations	50
Mutation percentage	0.5
Crossover percentage	0.5
Mutation rate	0.05

MOGWO

Parameter	**Value**
Population Size	30
Number of Iterations	50
Number of Population (wolves)	40
Grid Inflation Parameter (α)	0.1
Grids per each Dimension	20
Leader Selection Parameter (β)	4

Due to the symmetry of the receiver dispositions and the scenario in Fig. B.3, we took into account the evaluation of one-eighth of the points that were to be optimized and made the assumption that the optimal solutions could be mirrored in the corresponding similar receiver points. The position of the receiver (red dots) where the optimization is really done is shown in Fig. B.3. Since it would take a long time to evaluate the entire receiver point, this is significant for this initial investigation in a MISO scenario.

B.3. Preliminary Results

As described in Section B.2.2, the number of active transmitters that contributes to the received signal was determined according to the channel gain of the individual transmitter and

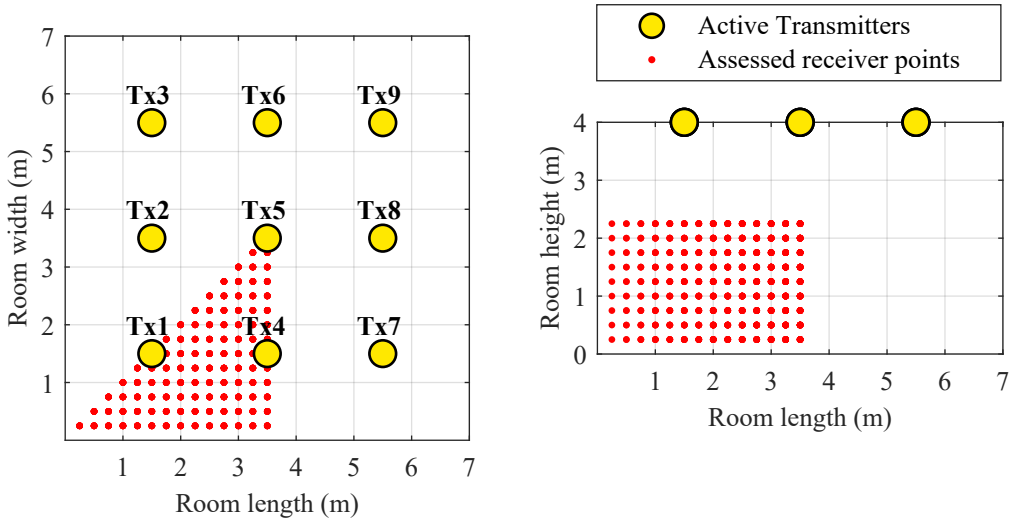

Figure B.3. Scenario with the point of the receiver to be evaluated for the optimization.

the receiver's position. Assessing all the possible links, the channel gain is determined. It is important to notice that, according to that restriction, the receiver's points that are far from the transmitter are likely to not have a link connection due to the high attenuation of the signal. Fig. B.4 shows the channel gain with the aforementioned constraint.

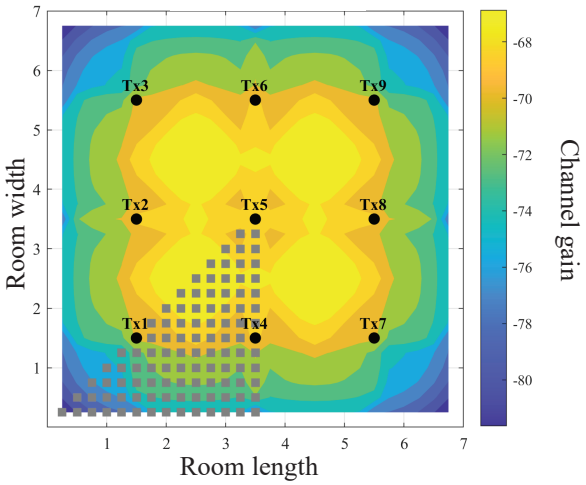

Figure B.4. Channel gain of the VLC link according to the position of the receiver, which is at a 50 cm height. The locations where the optimizations were actually assessed are indicated by the gray squares.

After running the routine proposed in this work, it is mandatory that the inequality constraint of the metric EVM< -11 dB be satisfied for 4-QAM. If this condition is not accepted, the solution is penalized by adding a high-value scalar to the objective values, so it is likely that the solution will be rejected by the optimization algorithm. Fig. B.5 shows the EVM for each knee-point solution determined by the HMO. The solutions in the yellow areas are those in which the EVM is higher than -11 dB, hence the receiver's solutions at those locations are penalized. In the other areas, more in the center of the room, the EVM is lower than -11 dB, which indicates

that the solutions are valid according to the imposed conditions.

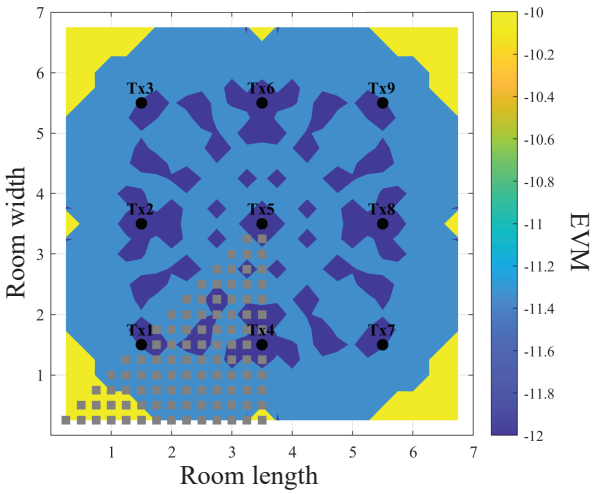

Figure B.5. Error vector magnitude of the knee-point solutions according to the receiver's positions. The yellow area is penalized since the EVM main condition (EVM $<$ -11 dB) is not satisfied.

Fig. B.6 shows the optimized power for 50 cm height receiver points. The position in which fewer transmitters are active, the less is the required power, on the contrary at the center of the room, where more superposition of signals is evaluated the power needed to fulfill the requirements of the problem is higher. As can be observed, the yellow is the solutions that were penalized since the EVM condition was not fulfilled.

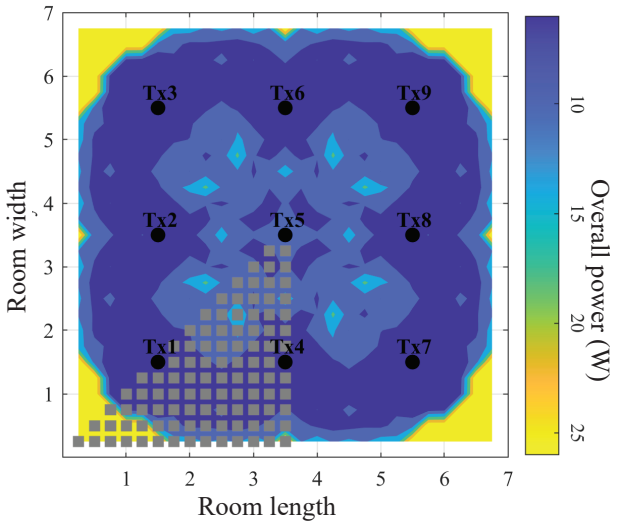

Figure B.6. Optimal power achieved by the evaluation of the HMO technique for the receivers at 50 cm height. Less power is required in the blue dark areas in which fewer transmitters are active, whereas the yellow parts denote the locations where the solutions were penalized because the EVM requirement wasn't met.

B.4. Next Steps

The further steps in this project are listed below:

- expand the optimization analysis in further work to account for different receiver heights, as well as their relationship.
- analyze the relation between the optimized features and the objectives determined in the problem formulation;
- investigate the relation between the received power and the performance of the system in order to modify the restriction of the minimum channel gain for the transmitter to be active;
- perform the updated GWO optimization and look for strategies to shorten the time it takes to evaluate the algorithms;
- investigate the minimum resolution of the receiver points.

APPENDIX C.

Clusterized Grey Wolf Optimizer

This Appendix presents the ongoing work on "Clusterized Grey Wolf Optimizer".

C.1. Objectives

The Grey Wolf Optimizer algorithm, despite being one of the most popular metaheuristic optimization algorithms, has the disadvantage of occasionally ignoring the precise global solution because the iterations used for investigation and exercise purposes are the same, as also seen through the simulations and experiments presented in this thesis. The literature has made numerous changes to address delayed convergence and local minimum stagnation of GWO in specific problems. [153, 154] but not typically address these problems for various complex cost functions. In order to obtain faster convergence and overcome local minimum stagnation with minimal computational effort, this work analyzes the use of several proposed GWO modifications and their capabilities. It also suggests a new position updating framework.

C.2. Methods

The GWO algorithm shows superiority in the exploitation process if compared with other metaheuristics but an inefficiency in exploration, which reflects slow convergence and low precision. In this way, in this work, the GWO is modified envisioning a faster convergence with lower fitness.

The proposed modification lies in the GWO updated position process working as a cluster. For that, it was used other modifications, in order to extract their abilities to better perform for different types of cost functions. For this initial investigation it was used the Randomized GWO [153], GWO-WD [155], λ-GWO, and a new update position modification that is mathematically expressed as

$$\overrightarrow{X}_{t+1} = \frac{\overrightarrow{A_1}^3\overrightarrow{X_1} + \overrightarrow{A_2}^3\overrightarrow{X_2} + \overrightarrow{A_3}^3\overrightarrow{X_3}}{\frac{1}{6}(\overrightarrow{C_1} + \overrightarrow{C_2} + \overrightarrow{C_3})} \tag{C.1}$$

In the GWO update position step, the solutions (wolves) are sorted according to their fitness the wolves are divided into four clusters. Each cluster updates the wolves' position considering the aforementioned modifications. At intervals of 5 iterations, half of the worse wolves of each

cluster are discarded and new solutions are generated randomly, considering the equality and inequality constraints.

The benchmark functions are frequently used to assess how well optimization algorithms perform. These mathematical functions provide insight into how effectively an optimization algorithm can discover the global minimum under various complexity scenarios. The two-dimensional unimodal benchmark functions assessed in this work are mathematically defined in Table C.2. The functions f_1 to f_7 are shown in Fig. C.2 for two dimensions.

The benchmark test functions known as multimodal functions include many peaks and valleys on their visualization, as well as more than one local maximum or minimum. Because there are numerous local minima that are not genuine global minima, these functions make it difficult for the optimization algorithms to discover the real global solution. Table C.1 shows the multimodal benchmark function used in this work. Some visualizations for two variables ($D = 2$) can be seen in Fig. C.1. Finally, the fixed-dimension multimodal benchmark functions are functions that have more than one local minimum or maximum in a fixed number of dimensions. Table C.1 describes the fixed-dimension multimodal benchmark functions used in this work.

Table C.1. Fixed-dimenstion multimodal benchmark functions.

Function	D	**Range**	$f_{\min}$
$f_{14}(x) = \left(\frac{1}{500} + \sum_{j=1}^{25} \frac{1}{j+\sum_{i=1}^{2}(x_i - a_{ij})^6}\right)$	2	[-65.54, 65.54]	1
$f_{15}(x) = \sum_{i=1}^{11} \left[a_i - \frac{x_i(b_i^2+b_i x_2)}{b_i^2+b_i x_3+x_4}\right]^2$	4	[-5, 5]	0.00030
$f_{16}(x) = 4x_1^2 - 2.1x_1^4 + \frac{1}{3}x_1^6 + x_1x_2 - 4x_2^2 + 4x_2^4$	2	[-5, 5]	-1.0316
$f_{17}(x) = \left(x_2 - \frac{5.1}{4\pi^2}x_1^2 + \frac{5}{\pi}x_1 - 6\right)^2 + 10\left(1 - \frac{1}{8\pi}\right)\cos(x_1) + 10$	2	[-5, 5]	0.398
$f_{18}(x) = [1 + (x_1 + x_2 + 1)^2) \times \ldots$ $(19 - 14x_1 + 3x_1^2 - 14x_2 + 6x_1x_2 + 3x_2^2)] \times \ldots$ $[30 + (2x_1 - 3x_2)^2 \times \ldots$ $(18 - 32x_1 + 12x_1^2 + 48x_2 - 36x_1x_2 + 27x_2^2)]$	2	[-2, 2]	3
$f_{19}(x) = -\sum_{i=1}^{4} c_i \cdot \exp\left(-\sum_{j=1}^{3} a_{ij}(x_j - p_{ij})^2\right)$	3	[1, 3]	-3.86
$f_{20}(x) = -\sum_{i=1}^{4} c_i \cdot \exp\left(-\sum_{j=1}^{6} a_{ij}(x_j - p_{ij})^2\right)$	6	[0, 1]	-3.32
$f_{21}(x) = -\sum_{i=1}^{5} \left[(X - a_i)(X - a_i)^{\mathrm{T}} + c_i\right]^{-1}$	4	[0, 10]	-10.1532
$f_{22}(x) = -\sum_{i=1}^{7} \left[(X - a_i)(X - a_i)^{\mathrm{T}} + c_i\right]^{-1}$	4	[0, 10]	-10.4028
$f_{23}(x) = -\sum_{i=1}^{10} \left[(X - a_i)(X - a_i)^{\mathrm{T}} + c_i\right]^{-1}$	4	[0, 10]	-10.5363

Table C.2. Unimodal benchmark functions for the dimensions 30, 100, and 1000.

Function Name	Function	Range	$f_{\min}$
Sphere	$f_1(x) = \sum_{i=1}^{n} x_i^2$	$[-100,\ 100]$	0
Schwefel's 2.22	$f_2(x) = \sum_{i=1}^{n} \lvert x_i \rvert + \prod_{i=1}^{n} \lvert x_i \rvert$	$[-10,\ 10]$	0
Schwefel's 1.20	$f_3(x) = \sum_{i=1}^{n} \left(\sum_{j-1}^{i} x_j \right)^2$	$[-100,\ 100]$	0
Schwefel's 2.21	$f_4(x) = \max_i \{ \lvert x_i \rvert, 1 \leq i \leq n \}$	$[-100,\ 100]$	0
Rosenbrock	$f_5(x) = \sum_{i=1}^{n-1} [100(x_{i+1} - x_i^2)^2 + (x_i - 1)^2]$	$[-30,\ 30]$	0
Step	$f_6(x) = \sum_{i=1}^{n} (\lvert x_i + 0.5 \rvert)^2$	$[-100,\ 100]$	0
Quartic Noise	$f_7(x) = \sum_{i=1}^{n} i \cdot x_i^4 + \texttt{random}(0, 1)$	$[-1.28,\ 1.28]$	0

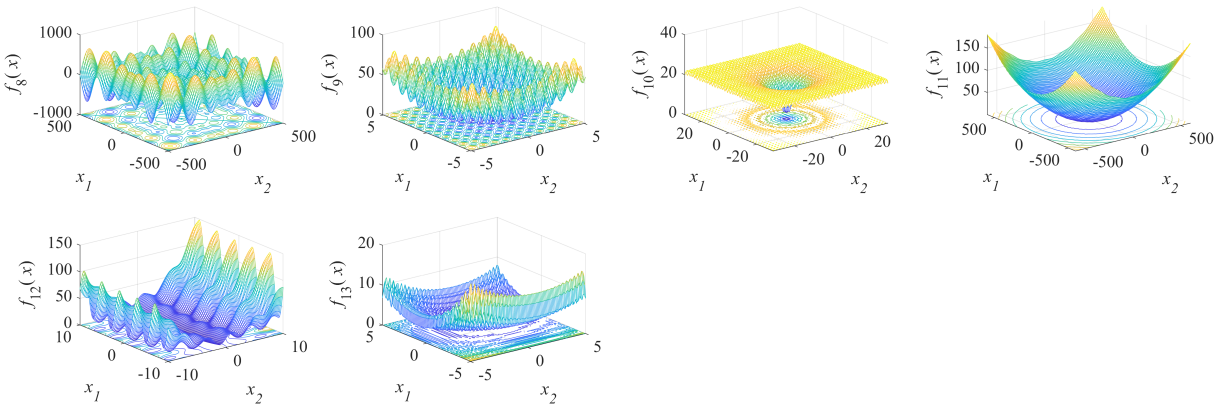

Figure C.1. Two-dimensional multimodal benchmark test functions.

C.3. Preliminary Results

The simulations were performed on a machine with a 2.80 GHz Intel Core i7 7600U CPU and 16 GB of DDR4 RAM. The algorithms used as stop criteria for the number of iterations were set to 500 iterations. The number of repetitions of each algorithm for each benchmark function was 30 times. The GWO and its modifications were parameterized for 30 agents (or wolves), at maximum, per iteration.

Table C.4 lists the results for the comparison of the GWO and the C-GWO in terms of the least achieved cost function value. As can be seen, the approach proposed in this work outperforms 30 of 39 of the uni and multimodal benchmark functions.

The results of the evaluated algorithms for the fixed-dimension multimodal benchmark functions are summarized in Table C.5. For these functions, the C-GWO did not show good performance if compared with the traditional GWO. For forty percent of the benchmark functions, the C-GWO outperforms GWO. However, 50% of the function's outputs are better solutions, on average, for the GWO. This also happens with the individual modifications here used and

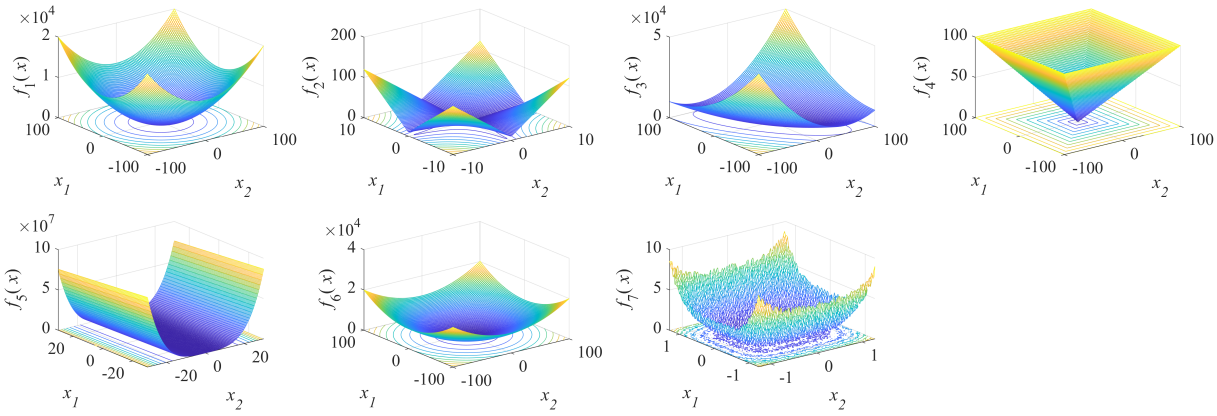

Figure C.2. Two-dimensional unimodal benchmark test functions.

should be investigated in more detail.

Table C.6 summarizes the results shown in the figures for the unimodal, multimodal, and fixed-dimension multimodal benchmark functions. As analyzed in terms of the minimum achieved cost value on average for the 30 repetitions of each algorithm for each function, the C-GWO performs better in 69 % of the assessed functions.

C.4. Next Steps

The following actions are required for this work:

- test other GWO modifications in the C-GWO in order to increase the number of benchmark functions in which the C-GWO performs better than the traditional GWO - mainly for fixed-dimension multimodal benchmark functions;
- apply the modified GWO here proposed to the VLC system in order to obtain faster convergence;
- analyze the CPU time per optimizer as the complexity quantification of the algorithm;
- study the exchange between the best solutions of each cluster;
- study the interval of new solutions generated.

Table C.3. Multimodal benchmark function for dimensions D = 30, 100, and 1000.

Function Name	**Function**	**Range**	$f_{\min}$
Schwefel's	$f_8(x) = \sum_{i=1}^{n} -x_i \sin(\sqrt{\lvert x_i \rvert})$	$[-500,\ 500]$	-12569.5
Rastrigin	$f_9(x) = \sum_{i=1}^{n} [x_i^2 - 10\cos(2\pi x_i) + 10]$	$[-5.12,\ 5.12]$	0
Ackley	$f_{10}(x) = -20\exp\left(-0.2\sqrt{\frac{1}{n}\sum_{i=1}^{n} x_i^2}\right) \ldots - \exp\left(\frac{1}{n}\sum_{i=1}^{n}\cos(2\pi x_i)\right) + 20 + e$	[-32, 32]	0
Griewank	$f_{11}(x) = \frac{1}{4000}\sum_{i=1}^{n} x_i^2 - \prod_{i=1}^{n}\cos\left(\frac{x_i}{\sqrt{i}}\right) + 1$	[-600, 600]	0
Pendilized	$f_{12}(x) = \frac{\pi}{n}\{10\sin(\pi y_1) + \ldots \sum_{i=1}^{n-1}(y_i - 1)^2\left[1 + 10\sin^2(\pi y_{i+1})\right]\} \ldots + \frac{\pi}{n}(y_n - 1)^2 + \sum_{i=1}^{n} u(x_i, 10, 100, 4))$ $y_i = 1 + \frac{x_i + 1}{4}$ $u(x_i, a, k, m) = \begin{cases} k(x_i - a)^m & x_i > a \\ 0 & -a < x_i < a \\ k(-x_i - a)^m & x_i < -a \end{cases}$	[-50, 50]	0
Generalized Pendilized	$f_{13}(x) = 0.1\sin^2(3\pi x_1) + \ldots 0.1\sum_{i=1}^{n}(x_i - 1)^2[1 + \sin^2(3\pi x_i + 1)] + \ldots 0.1(x_n - 1)^2[1 + \sin^2(2\pi x_n)] + \ldots \sum_{i=1}^{n} u(x_i, 5, 100, 4)$	[-50, 50]	0

Table C.4. Comparison modified version with conventional GWO: Uni and Multimodal BTF

F	D	GWO				C-GWO			
		ave	*std*	*best*	*worst*	*ave*	*std*	*best*	*worst*
f_1	30	8.49e-28	9.84e-28	6.28e-29	4.15e-27	**0.00e+00**	0.00e+00	**0.00e+00**	**0.00e+00**
	100	1.64e-12	1.36e-12	2.74e-13	5.34e-12	**0.00e+00**	0.00e+00	**0.00e+00**	**0.00e+00**
	1000	2.64e-01	6.76e-02	1.51e-01	4.26e-01	**0.00e+00**	0.00e+00	**0.00e+00**	**0.00e+00**
f_2	30	1.03e-16	1.01e-16	1.91e-17	5.47e-16	**0.00e+00**	0.00e+00	**0.00e+00**	**0.00e+00**
	100	4.95e-08	1.71e-08	2.44e-08	8.76e-08	**0.00e+00**	0.00e+00	**0.00e+00**	**0.00e+00**
	1000	**6.26e-01**	3.36e-01	**2.74e-01**	**1.80e+00**	6.48e+86	3.55e+87	2.51e+03	1.94e+88
f_3	30	7.01e-06	1.66e-05	6.99e-09	8.75e-05	**0.00e+00**	0.00e+00	**0.00e+00**	**0.00e+00**
	100	4.74e+02	6.47e+02	4.15e+01	3.20e+03	**0.00e+00**	0.00e+00	**0.00e+00**	**0.00e+00**
	1000	1.55e+06	2.94e+05	1.04e+06	2.31e+06	**0.00e+00**	0.00e+00	**0.00e+00**	**0.00e+00**
f_4	30	7.86e-07	7.93e-07	8.33e-08	4.02e-06	**0.00e+00**	0.00e+00	**0.00e+00**	**0.00e+00**
	100	7.30e-01	6.47e-01	3.47e-02	2.56e+00	**0.00e+00**	0.00e+00	**0.00e+00**	**0.00e+00**
	1000	7.97e+01	3.83e+00	7.29e+01	8.65e+01	**0.00e+00**	0.00e+00	**0.00e+00**	**0.00e+00**
f_5	30	**2.73e+01**	8.46e-01	**2.60e+01**	**2.88e+01**	2.88e+01	1.79e-01	2.81e+01	2.90e+01
	100	**9.77e+01**	7.28e-01	**9.60e+01**	**9.85e+01**	9.88e+01	2.26e-01	9.80e+01	9.90e+01
	1000	1.06e+03	3.85e+01	1.02e+03	1.17e+03	**9.99e+02**	7.49e-02	**9.99e+02**	**9.99e+02**
f_6	30	6.65e-01	3.85e-01	**8.97e-05**	1.75e+00	**3.25e-01**	2.48e-01	4.38e-04	**8.66e-01**
	100	9.60e+00	9.71e-01	7.46e+00	1.13e+01	**7.81e+00**	1.24e+00	**5.31e+00**	**9.76e+00**
	1000	2.03e+02	2.93e+00	1.97e+02	2.11e+02	**1.89e+02**	6.20e+00	**1.76e+02**	**2.05e+02**
f_7	30	2.13e-03	1.03e-03	3.60e-04	4.22e-03	**5.45e-05**	5.15e-05	**3.74e-06**	**2.41e-04**
	100	7.22e-03	2.41e-03	3.55e-03	1.35e-02	**5.40e-05**	4.15e-05	**4.12e-06**	**1.52e-04**
	1000	1.52e-01	3.77e-02	1.11e-01	2.39e-01	**6.13e-05**	6.23e-05	**2.12e-06**	**2.43e-04**
f_8	30	**-5.70e+03**	9.24e+02	**-7.28e+03**	-3.18e+03	-5.16e+03	1.56e+02	-5.42e+03	**-5.06e+03**
	100	**-1.59e+04**	3.13e+03	**-1.90e+04**	-5.65e+03	-1.53e+04	4.14e+02	-1.61e+04	**-1.44e+04**
	1000	-8.47e+04	2.25e+04	-1.04e+05	-1.88e+04	**-1.44e+05**	2.26e+03	**-1.48e+05**	**-1.41e+05**
f_9	30	7.44e+00	2.55e+01	0.00e+00	1.41e+02	**0.00e+00**	0.00e+00	0.00e+00	**0.00e+00**
	100	9.27e+00	5.91e+00	3.35e-11	2.36e+01	**0.00e+00**	0.00e+00	**0.00e+00**	**0.00e+00**
	1000	2.14e+02	5.50e+01	1.12e+02	3.18e+02	**0.00e+00**	0.00e+00	**0.00e+00**	**0.00e+00**
f_{10}	30	1.03e-13	1.88e-14	7.51e-14	1.57e-13	**4.44e-16**	0.00e+00	**4.44e-16**	**4.44e-16**
	100	1.28e-07	4.27e-08	5.49e-08	2.36e-07	**4.44e-16**	0.00e+00	**4.44e-16**	**4.44e-16**
	1000	1.85e-02	2.69e-03	1.28e-02	2.27e-02	**4.44e-16**	0.00e+00	**4.44e-16**	**4.44e-16**
f_{11}	30	2.78e-03	6.97e-03	0.00e+00	2.86e-02	**0.00e+00**	0.00e+00	0.00e+00	**0.00e+00**
	100	4.70e-03	1.25e-02	9.45e-14	4.80e-02	**0.00e+00**	0.00e+00	**0.00e+00**	**0.00e+00**
	1000	3.03e-02	5.31e-02	9.09e-03	2.39e-01	**1.18e-04**	6.48e-04	**0.00e+00**	**3.55e-03**
f_{12}	30	**3.50e-02**	2.15e-02	**6.58e-03**	1.08e-01	4.68e-02	2.02e-02	1.47e-02	**9.09e-02**
	100	2.22e-01	5.09e-02	1.49e-01	3.54e-01	**2.17e-01**	5.12e-02	**1.36e-01**	**3.44e-01**
	1000	7.98e-01	2.01e-02	7.61e-01	8.31e-01	**7.61e-01**	2.06e-02	**7.20e-01**	**8.23e-01**
f_{13}	30	**4.54e-01**	1.60e-01	**2.00e-01**	**7.03e-01**	1.30e+00	3.58e-01	8.00e-01	2.80e+00
	100	**4.95e+00**	4.51e-01	**3.93e+00**	**5.61e+00**	9.54e+00	9.97e-01	6.54e+00	1.01e+01
	1000	**8.84e+01**	9.75e-01	**8.66e+01**	**9.13e+01**	9.99e+01	1.44e-01	9.93e+01	1.00e+02
- / = / +				9 / 0 / 30					

Table C.5. Comparison of the clustered GWO and the traditional GWO for the fixed-dimension multimodal benchmark functions.

F	D	GWO				C-GWO			
		ave	*std*	*best*	*worst*	*ave*	*std*	*best*	*worst*
f_{14}	2	4.17e+00	3.96e+00	9.98e-01	1.27e+01	**1.06e+00**	2.52e-01	**9.98e-01**	**1.99e+00**
f_{15}	4	3.88e-03	7.50e-03	**3.07e-04**	2.04e-02	**1.70e-03**	3.60e-03	3.72e-04	**1.93e-02**
f_{16}	2	**-1.03e+00**	3.63e-08	-1.03e+00	**-1.03e+00**	-1.03e+00	5.26e-06	**-1.03e+00**	-1.03e+00
f_{17}	2	**3.98e-01**	4.72e-06	**3.98e-01**	**3.98e-01**	3.98e-01	4.64e-04	3.98e-01	4.00e-01
f_{18}	2	3.00e+00	6.12e-05	**3.00e+00**	**3.00e+00**	**3.00e+00**	6.21e-05	3.00e+00	3.00e+00
f_{19}	3	-3.00e-01	2.26e-16	-3.00e-01	-3.00e-01	-3.00e-01	2.26e-16	-3.00e-01	-3.00e-01
f_{20}	6	-3.23e+00	9.59e-02	**-3.32e+00**	-3.08e+00	**-3.27e+00**	7.84e-02	-3.32e+00	**-3.10e+00**
f_{21}	4	**-9.07e+00**	2.51e+00	**-1.02e+01**	**-2.68e+00**	-6.59e+00	2.95e+00	-1.02e+01	-8.81e-01
f_{22}	4	**-1.04e+01**	9.17e-04	**-1.04e+01**	**-1.04e+01**	-8.73e+00	2.63e+00	-1.04e+01	-2.77e+00
f_{23}	4	**-1.05e+01**	1.08e-03	-1.05e+01	**-1.05e+01**	-9.83e+00	2.19e+00	**-1.05e+01**	-2.42e+00
- / = / +				5 / 1 / 4					

Table C.6. Comparison of results between GWO and C-GWO.

	C-GWO		
	Worse	Equal	Better
D = 30	4	0	9
D = 100	3	0	10
D = 1000	2	0	11
Fixed-dimension	5	1	4
Total	14	1	34